DTRA
Defense Threat
Reduction Agency

INVESTIGATION OF NANO-NUCLEAR REACTIONS IN CONDENSED MATTER

FINAL REPORT

Dr. Pamela A. Mosier-Boss
SPAWAR Systems Center Pacific
San Diego, CA 92152

Mr. Lawrence P. Forsley
JWK International
7617 Little River Turnpike Suite 1000
Annandale, VA 22003

Dr. Patrick J. McDaniel
University of New Mexico
Albuquerque, NM 87131

TABLE OF CONTENTS

LIST OF ABBREVIATIONS

AAAS	American Association for the Advancement of Science
AC	alternating current
ACS	American Chemical Society
ADM	Admiral
AFCEA	Armed Forces Communications and Electronics Association
Ag	silver
AgCl	silver chloride
Al	aluminum
Am	americium
APS	American Physical Society
ARPA-E	Advanced Research Projects Agency-Energy
ASN	Assistant Secretary of the Navy
Au	gold
B	boron
BARC	Bhabha Atomic Research Centre
Be	beryllium
BF_3	boron trifluoride
BK	Ban & Korn
bkg	background
BTI	Bubble Technology Industries
C4I	command, control, communication, computers, and intelligence,
C4ISR	command, control, communication, computers, intelligence, surveillance, and reconnaissance
C	carbon
Capt.	Captain
CBS	Columbia Broadcasting System
CCD	charge coupled device
CD	compact disk
CDR	Commander
Cf	californium
cfi	chromatic aberration-free infinity
CH	carbon-hydrogen bond
CH_2	methylene group
CIA	Central Intelligence Agency
Cl	chlorine/chloride
Cl_2	chlorine gas
cm	centimeter
cm^2	square centimeter
cm^3	cubic centimeter
CO_2	carbon dioxide
C-O-C	ether group
cpm	counts per minute
cps	counts per second
CR-39	Columbia resin #39

Cs	cesium
Cu	copper
$CuCl_2$	copper chloride
d	DC (direct current)
D	deuterium
D_2	deuterium gas
D_2^+	charged deuterium gas
DAQ	data acquisition
DC	direct current
D.C.	District of Columbia
DDR&E	Department of Defense Research and Engineering
D_2O	deuterated water
DoD	Department of Defense
DoE	Department of Energy
Dr.	doctor
DTRA	Defense Threat Reduction Agence
E	applied voltage
E	electric
EDX	Energy-dispersive X-ray spectroscopy
EMIS	Energetic Materials Intelligence Seminar
ENEA	Ente Nazionale per l'Energia Atomica (National Agency for Atomic Energy)
et al.	and company
Fe	iron
g	gram
Ge	germanium
GPIB	general purpose interface bus
GUI	graphical user interface
h	height
h	hour
H	height
H	hydrogen
H_2	hydrogen gas
H_x	hydrogen at ratio x
HAD	heat after death
He	helium
HE	high explosive
Hg	mercury
Hg_2SO_4	mercurous sulfate
H_2O	water
HPGe	high purity germanium
HPLC	high pressure liquid chromatography
HQ	headquarters
I	current
ICCF	International Conference of Cold Fusion
ICF	inertial confinement fusion

i.e.	that is
in	inch
In	indium
IL	Illinois
IR	infrared
J	Joule
JASON	July August September October November or Junior Achiever, Somewhat Older Now
Jr.	junior
JWK	Jay Woo Khim
K	Kelvin
K	potassium
keV	kiloelectron volt
kJ	kilojoule
L	length
LANL	Los Alamos National Laboratory
LENR	low energy nuclear reactions
LET	linear energy transfer
Li	lithium
LiCl	lithium chloride
Li_2SO_4	lithium sulfate
LLC	Limited Liability Company
LP	low profile
LS	liquid scintillator
Lt. Gen.	Lieutenant General
M	metal
M	molar concentration
mA	milli-ampere
MCl_2	metal chloride
MD	Maryland
MDS	Molecular Devices Company
MeV	mega-electron volt
min	minute
mL	milliliter
mm	millimeter
mm^2	square millimeter
mol	mole
Mr.	Mister
mV	millivolt
n	neutron
Na	sodium
NaI	sodium iodide
NaOH	sodium hydroxide
NASA	National Aeronautics and Space Administration
Nd	neodymium

NdFeB	neodymium iron boron alloy
NDIA	National Defense Industrial Association
Ne	neon
Ni	nickel
NI	National Instruments
NMR	nuclear magnetic resonance
NPR	National Public Radio
NPT	national pipe thread
n/s	neutrons per second
O	oxygen
O_2	oxygen gas
OCP	open circuit potential
OD	outer diameter
OH	Ohio
ONR	Office of Naval Research
OOP	optimal operating point
p	proton
P	phosphorous
PAO	Public Affairs Office
PAR	Princeton Applied Research
Pb	lead
PCI	peripheral component interconnect
Pd	palladium
$PdCl_2$	palladium chloride
PdO	palladium oxide
PE	polyethylene
p.n.	part number
Po	polonium
psig	pounds per square inch gauge
Pt	platinum
Pu	plutonium
Q&A	questions and answers
r	radius
RADM	Rear Admiral
RDA	research, development, and acquisition
R&D	research and development
RDECOM	Research Development and Engineering Command
RTV	room temperature vulcanized
Ru	ruthenium
rxns	reactions
s	second
S	superwave
SEM	scanning electron microscope
SES	Senior Executive Services
Si	silicon

Sn	tin
SRIM	stopping and range of ions in matter
$SrSO_4$	strontium sulfate
SPAWAR	Space and Naval Warfare Systems Command
SPI	Structure Probe, Incorporated
SRI	Stanford Research Institute
SS	stainless steel
SSB	silicon surface barrier
SSC	SPAWAR Systems Center
SSNTD	solid state nuclear track detector
S&T	science and technology
SW	superwave
T	tritium
T	temperature
T	type of thermocouple that is copper, constantan (Cu-Ni alloy)
T_c	critical temperature
TFT	task force team
Tl	thallium
U	uranium
UAV	Unmanned Autonomous Vehicle
UCSD	University of California San Diego
UK	United Kingdom
URL	universal resource locator
U.S.	United States
USAF	United States Air Force
USB	universal serial bus
USV	Unmanned Submersible Vehicle
UT	Utah
V	volume
V	volt
VADM	Vice Admiral
vs.	versus
W	width
x	times (magnification)
x	abscissa spatial coordinate
XP	experience
XRD	X-ray diffractometer
y	ordinate spatial coordinate
YSI	Yellow Springs Instrument Company
Z	atomic number

α	alpha
β	beta
ΔT	temperature difference

γ	gamma
μA	microampere
μCi	microcurie
μL	microliter
μm	micron
μm^3	cubic micron
π	pi

~	approximately
>	greater than
≥	greater than or equal to
<	lesser than
≤	lesser than or equal to
°	degree
°C	degrees Celsius
%	percent

vide infra	Latin for see below
vide supra	Latin for see above

LIST OF TABLES

LIST OF FIGURES

Appendix I: Miscellaneous

1. Statement given at the press conference at the American Chemical Society on March 2009

2. Complete bibliography of SSC-Pacific LENR publications

Appendix II: List of Publications on CD

1. ‘Further Evidence of Nuclear Reactions in the Pd/D Lattice: Emission of Charged Particles,’ S. Szpak, P.A. Mosier-Boss, and F.E. Gordon, Naturwissenshaften, **94**, 511-514 (2007).

2. ‘Further Evidence of Nuclear Reactions in the Pd/D Lattice: Emission of Charged Particles: Erratum,’ S. Szpak, P.A. Mosier-Boss, and F.E. Gordon, Naturwissenshaften, **94**, 515 (2007).

3. ‘Use of CR-39 in Pd/D Co-deposition Experiments,’ P.A. Mosier-Boss, S. Szpak, F.E. Gordon, and L.P.G. Forsley, Eur. Phys. J. Appl. Phys., **40**, 293-303 (2007).

4. ‘Comment on “The Use of CR-39 in Pd/D Co-deposition Experiments” by P.A. Mosier-Boss, S. Szpak, F.E. Gordon, and L.P.G. Forsley: Interpreting SPAWAR-Type Dominant Pits,’ L. Kowalski, Eur. Phys. J. Appl. Phys., **44**, 287-290 (2008).

5. ‘Reply to Comment on “The Use of CR-39 in Pd/D Co-deposition Experiments”: a Response to Kowalski,’ P.A. Mosier-Boss, S. Szpak, F.E. Gordon, and L.P.G. Forsley, Eur. Phys. J. Appl. Phys., **44**, 291-295 (2008).

6. ‘Detection of Energetic Particles and Neutrons Emitted During Pd/D Co-deposition,’ P.A. Mosier-Boss, S. Szpak, F.E. Gordon, and L.P.G. Forsley, Low-Energy Nuclear Reactions Sourcebook (Vol. 1) , Jan Marwan, Steven B. Krivit, editors, *American Chemical Society/Oxford University Press*, Washington, D.C., 311-334 (2008).

7. ‘Triple Tracks in CR-39 as the Result of Pd-D Co-deposition: Evidence of Energetic Neutrons,’ P.A. Mosier-Boss, S. Szpak, F.E. Gordon, and L.P.G. Forsley, Naturwissenschaften, **96**, 135-142 (2009).

8. ‘Characterization of Neutrons Emitted during Pd/D Co-deposition,’ P.A. Mosier-Boss, S. Szpak, F.E. Gordon, and L.P.G. Forsley, J. Sci Exploration, **23**, 473-477 (2009).

9. ‘Characterization of Tracks in CR-39 Detectors Obtained as a Result of Pd/D Co-deposition,’ P.A. Mosier-Boss, S. Szpak, F.E. Gordon, and L.P.G. Forsley, Eur. Phys. J. Appl. Phys., **46**, 30901-p1 to p12 (2009).

10. ‘Technology Forecast: Worldwide Research on Low-Energy Nuclear Reactions Increasing and Gaining Acceptance,’ Defense Intelligence Agency Analysis Report DIA-08-0911-003, B. Barnhart, P. McDaniel, P. Mosier-Boss, M. McKubre, L. Forsley, and L, DeChiaro (2009).

11. ‘Characterization of Energetic Particles Emitted During Pd/D Co-deposition for Use in a Radioisotope Thermoelectric Generator (RTG),’ P.A. Mosier-Boss, F.E. Gordon, and L.P.G. Forsley, Low-Energy Nuclear Reactions Sourcebook (Vol. 2) , Jan Marwan, Steven B. Krivit, editors, *American Chemical Society/Oxford University Press*, Washington, D.C., 119-135 (2009).

12. ‘Comments on Codeposition Electrolysis Results,’ L. Kowalski, J. Condensed Matter Nucl. Sci., **3**, 1-3 (2010).

13. ‘Comments on Codeposition Electrolysis Results: A Response to Kowalski,’ P.A. Mosier-Boss, F.E. Gordon, and L.P.G. Forsley, J. Condensed Matter Nucl. Sci., **3**, 4-8 (2010).

14. ‘Comparison of Pd/D Co-deposition and DT Neutron Generated Triple Tracks Observed in CR-39 Detectors,’ P.A. Mosier-Boss, J.Y. Dea, L.P.G. Forsley, M.S. Morey, J.R. Tinsley, J.P. Hurley and F.E. Gordon, Eur. Phys. J. Appl. Phys., **51**, 20901-p1 to p10 (2010).

15. ‘A New Look at Low-Energy Nuclear Reaction Research,’ S.B. Krivit and J. Marwan, J. Environ. Monitoring, **11**, 1731-1746 (2009).

16. Comments on “A New Look at Low-Energy Nuclear Reaction Research,” K. Shanahan, J. Environ. Monitoring, **12**, 1756-1764 (2010).

17. ‘A New Look at Low-Energy Nuclear Reaction Research: A Response to Shanahan,’ J. Marwan, M.C.H. McKubre, F.L. Tanzella, P.L. Hagelstein, M.H. Miles, M.R. Swartz, E. Storms, Y. Iwamura, P.A. Mosier-Boss, and L.P.G. Forsley, J. Environ. Monitoring, **12**, 1765-1770 (2010).

18. ‘Review of Twenty Years of LENR Research Using Pd/D Co-deposition,’ P.A. Mosier-Boss, J.Y. Dea, F.E. Gordon, L.P.G. Forsley, and M.H. Miles, J. Condensed Matter Nucl. Sci., **4**, 173-187 (2011).

19. ‘Comparison of SEM and Optical Analysis of DT Neutron Tracks in CR-39 Detectors,’ P.A. Mosier-Boss, L.P.G. Forsley, P. Carbonelle, M.S. Morey, J.R. Tinsley, J.P. Hurley, and F.E. Gordon, SPIE Conference Proceedings on Hard X-Ray, Gamma-Ray, and Neutron Detector Physics XIII, Larry A. Franks, Ralph B. James, and Arnold Burger editors (2011).

20. ‘Comparison of SEM and Optical Analyses of DT Neutron Tracks in CR-39 Detectors,’ P.A. Mosier-Boss, L.P.G. Forsley, P. Carbonelle, M.S. Morey, J.R. Tinsley, J.P. Hurley, and F.E. Gordon, Radiat. Meas., **47**, 57-66 (2012).

21.’Characterization of Neutrons Emitted during Pd/D Co-deposition,’ P.A. Mosier-Boss, F.E. Gordon, L.P.G. Forsley, J. Condensed Matter Nucl. Sci., 6, 13-23 (2012).

22. ‘A Review on Nuclear Products Generated During Low-Energy Nuclear Reactions (LENR),’ P.A. Mosier-Boss, J. Condensed Matter Nucl. Sci., 6, 135-148 (2012).

Appendix III: List of Presentations on CD (Speaker Underlined)

1. ‘20 Years of LENR Research using Co-deposition,’ S. Szpak, P.A. Mosier-Boss, F.E. Gordon, Symposium on New Energy Technology, 237th American Chemical Society National Meeting, Salt Lake City, UT, Mar. 22-26, 2009.

2. ‘Nano-Nuclear Reactions in Condensed Matter,’ L.P.G. Forsley and P.A. Mosier-Boss, Symposium on New Energy Technology, 237th American Chemical Society National Meeting, Salt Lake City, UT, Mar. 22-26, 2009.

3. ‘Characterization of Neutrons Emitted During Pd/D Co-deposition,’ P.A. Mosier-Boss, S. Szpak, F.E. Gordon, L.P.G. Forsley, Symposium on New Energy Technology, 237th American Chemical Society National Meeting, Salt Lake City, UT, Mar. 22-26, 2009.

4. ‘Twenty Year History in LENR Research Using Pd/D Co-deposition,’ S. Szpak, F.E. Gordon, P.A. Mosier-Boss, L.P.G. Forsley, M. Miles, and M, Swartz, University of Missouri, May 30, 2009.

5. ‘Cold Fusion: Reality or Fiction,’ L.P.G. Forsley, Conference at Université Catholique de Louvain, May 4-5, 2009.

6. ‘Twenty Years of LENR Research,’ P.A. Mosier-Boss, AFCEA C4ISR, San Diego, CA, May 14, 2009.

7. ‘Low Energy Nuclear Reactions (LENR) Research at SPAWAR Systems Center Pacific to Chief of Naval Operations/Strategic Studies Group,’ P.A. Mosier-Boss, Dec. 9, 2009.

8. ‘Characterization of Nuclear Emissions Resulting from Pd/D Co-deposition,’ P.A. Mosier-Boss, F.E. Gordon, and L.P.G. Forsley, Symposium on New Energy Technology, 239th American Chemical Society National Meeting San Francisco, CA, Mar. 21-22, 2010.

9. ‘Evidence of the Occurrence of LENR in a Metal Lattice,’ P.A. Mosier-Boss, EMIS 2010, May 13, 2010.

10. ‘Evidence of Nuclear Particles,’ P.A. Mosier-Boss, RDECOM Power and Energy TFT LENR Workshop, Army Research Labs, Adelphi, MD, June 29, 2010.

11. ‘Comparison if Three Methods of Analyzing Tracks Observed in CR-39 Detectors Used in Pd/D Co-deposition Experiments,’ L.P.G. Forsley, P.A. Mosier-Boss, F. Tanzella, A. Lipson, D. Zhou, A, Roussetski, M. McKubre, Symposium on New Energy Technology, 241st American Chemical Society National Meeting, Anaheim, CA, Mar. 21-25, 2011.

12. ‘Comparison of DT-Generated and Pd/D Co-deposition Triple tracks in CR-39 Detectors,’ P.A. Mosier-Boss, F.E. Gordon, L.P.G. Forsley, P. Carbonelle, M.S. Morey, J.R. Tinsley, and J.P. Hurley, Symposium on New Energy Technology, 241st American Chemical Society National Meeting, Anaheim, CA, Mar. 2011.

13. ‘Comparison of SEM and Optical Analysis of DT Neutron Tracks in CR-39 Detectors,’ P.A. Mosier-Boss, L.P.G. Forsley, P. Carbonelle, M.S. Morey, J.R. Tinsley, J.P. Hurley, and F.E. Gordon, SPIE Conference on Hard X-Ray, Gamma-Ray, and Neutron Detector Physics XIII, San Diego, CA, Aug, 21-24, 2011.

14. ‘The Greening of America: a New Nuclear Future,’ P.A. Mosier-Boss, 243rd American Chemical Society National Meeting, San Diego, CA, Mar. 2012.

15. ‘Fukushima Revisited and the Nano-Nuclear Alternative,’ L.P.G. Forsley, 243rd American Chemical Society National Meeting, San Diego, CA, Mar. 2012.

1.0 INTRODUCTION

On March 23, 1989, Martin Fleischmann and Stanley Pons, professors of chemistry at the University of Utah, held a press conference to announce the results of electrochemical experiments that produced more heat than could be accounted for by chemical means. They speculated that the heat had a nuclear origin. The experiments were quickly dubbed "Cold Fusion" by the news media. The physics community noted that Fleischmann and Pons had not published their results in any journal prior to their announcement, there had been no reports of any replications of the effect, there was no mention of the generation of any nuclear ash, and that the reported results did not match theory. Despite these perceived irregularities scientists, worldwide, went into their laboratories to replicate the Fleischmann–Pons results. A few scientists succeeded but a great many more failed. It is now known that those failures were due to the fact that the experimental conditions necessary to achieve the effect, *i.e.*, high D loading and high D flux inside the Pd lattice, had not been achieved. Ultimately, the lack of replication by others and the fact that Fleischmann and Pons were not able to defend their original claims caused most scientists to lose interest.

At the time of the announcement in 1989, SPAWAR Systems Center Pacific scientists were involved in developing batteries for torpedo propulsion. The lead scientist in those torpedo propulsion efforts, Stanislaw Szpak, was aware of the Fleischmann–Pons experiment prior to the press conference and knew about the long incubation times needed to fully load bulk Pd with D. To reduce the incubation time, he developed the Pd/D co-deposition process as a means to initiate low energy nuclear reactions (LENR) inside the Pd lattice. In this process, working and counter electrodes are immersed in a solution of palladium chloride and lithium chloride in deuterated water. Figure 1-1a shows a photograph of an operating Pd/D co-deposition cell. When a current is applied, Pd metal plates out on the cathode in the presence of evolving deuterium gas. Figure 1-1b shows an SEM photomicrograph of an electrode prepared by Pd/D co-deposition. From the SEM, it can be seen that the Pd deposit exhibits highly expanded surfaces consisting of spherical modules in the micron and nano-scale size regimes.[1,2]

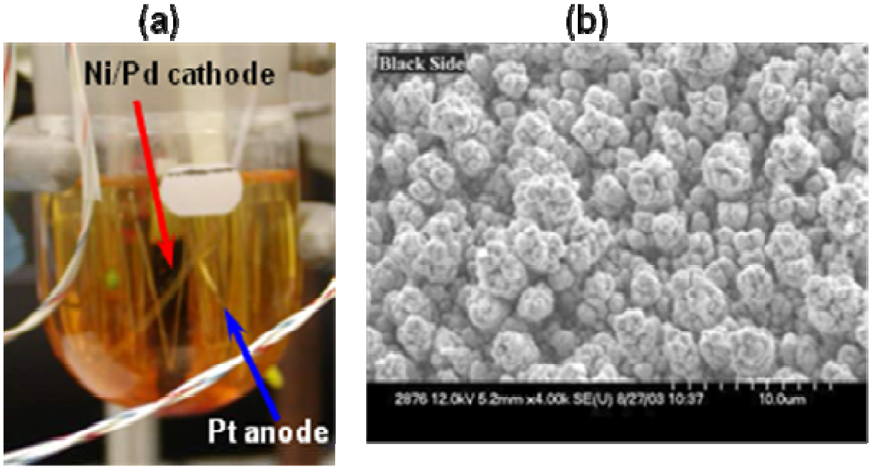

Figure 1-1. (a) Photograph of an operating Pd/D co-deposition cell. (b) SEM photomicrograph of the Pd deposit formed as a result of Pd/D co-deposition.

The Pd/D co-deposition process has been shown to provide a reproducible means of manufacturing Pd-D nano-alloys that induce low energy nuclear reactions (LENRs). Cyclic voltammetry[2,3] and galvanostatic pulsing[4] experiments indicate that, by using the co-deposition technique, a high degree of deuterium loading (with an atomic ratio D/Pd>1) is obtained within seconds. These experiments also indicate the existence of a D_2^+ species within the Pd lattice. Because an ever expanding electrode surface is created, non-steady state conditions are assured, the cell geometry is simplified because there is no longer a need for a uniform current distribution on the cathode, and long charging times are eliminated.[5]

By using the Pd/D co-deposition technique and co-depositional variants[6] (based on flux control[7,8]), solid evidence (*i.e.*, excess heat generation,[7,9,10], hot spots,[11] mini-explosions, ionizing radiation,[12] near- IR emission,[13] tritium production,[14] transmutation,[15] and neutrons[16]) has been obtained that indicate that lattice assisted nuclear reactions can and do occur within the Pd lattice. The results to date indicate that some of the reactions occur very near the surface of the electrode (within a few atomic layers). Also, the reactions may be enhanced in the presence of either an external electric or magnetic field, or by optically irradiating the cathode of cells driven at their optimal operating point (OOP). Optimal operating points appear when heat, power gain, or helium or tritium production, are presented as a function of the input electrical power.[17,18] They allow standardization, and driving with electrical input power beyond the OOP yields a falloff of the production rates.

Besides LENR, the Pd/H(D) system exhibits superconductivity. Palladium itself does not superconduct. However, it was found that H(D)/Pd does and that the critical temperatures of the deuteride are about 2.5 K higher than those of hydride (at the same atomic ratios).[19] This is the 'inverse' isotope effect. In these early measurements, the loading of H(D) in the Pd lattice was less than unity, *i.e.* H(D):Pd < 1. Later Tripodi *et al.*[20] developed a method of loading and stabilizing 50 μm diameter Pd wires with H(D):Pd loadings greater than one. These samples have exhibited near room temperature superconductivity. Examples of measured superconducting transitions of PdH_x samples are shown in Figure 1-2.

We believe the two phenomena, LENR and high T_c superconductivity, are related and that both need to be investigated in order to gain an understanding of the processes occurring inside the Pd lattice. The scope of this effort was to design and conduct experiments to elucidate the underlying physics of nuclear reactions occurring inside Pd-D nano-alloys and to make that data available to theoreticians to aid in their ability to develop a theory that explains how and why low energy nuclear reactions can occur within a palladium lattice. Development of such a theory is needed to provide insight on how to optimize the LENR processes occurring in the Pd lattice. In this report, results of the following experiments will be discussed:

1. Analysis of the CR-39 detectors used in the SRI replication of the SSC-Pacific co-deposition experiment
2. Summary of experiments that rule out chemical/mechanical origins for the tracks observed in CR-39 used in Pd/D co-deposition experiments
3. Comparison of DT and Pd/D co-deposition generated triple tracks in CR-39 detectors
4. Pd/D co-deposition experiments conducted using uranium as a witness material

5. The apparent discrepancy between CR-39 and X-ray measurements to detect charged particles
6. Temporal measurements of radiation, neutrons, and charged particles
7. Thermal measurements
8. Preparation and characterization of stabilized Pd foils and nano-deposits

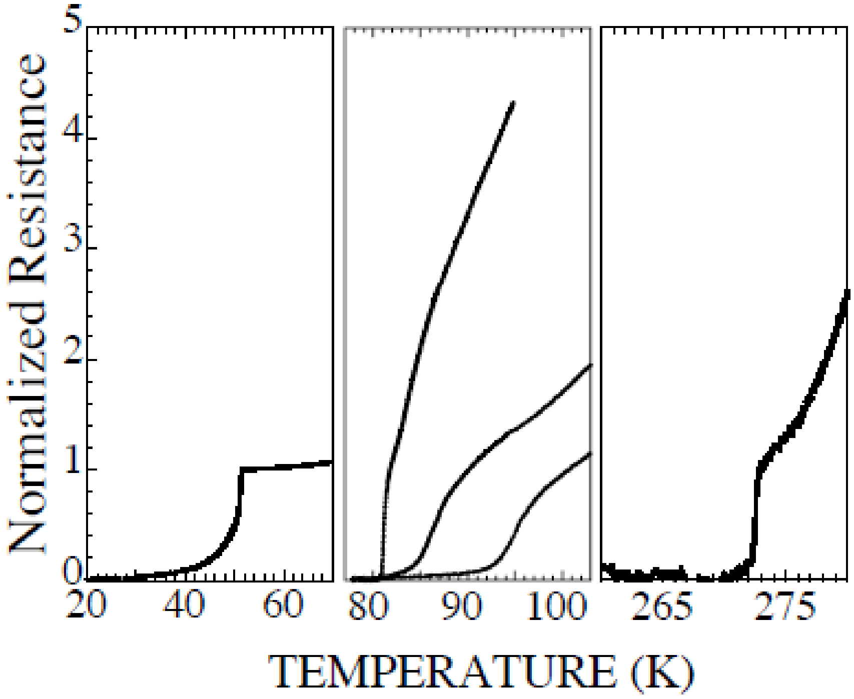

Figure 1-2. A series of superconducting transitions for PdH_x samples are shown.[20]

2.0 EXPERIMENTAL PROCEDURES

2.1 Chemicals

The following salts from Aldrich were used: palladium chloride, copper (II) chloride, nickel chloride, lithium sulfate, and mercurous sulfate. Lithium chloride came from Fluka. Aldrich HPLC grade water was used in light water experiments. Deuterated water (99.9% D) was obtained from Aldrich. Uranyl nitrate was obtained from SPI Chemicals. For deuterated water experiments, the lithium chloride and lithium sulfate were dried prior to use. Plating solutions were typically 0.03 M MCl_2 (where M = Pd, Ni, or Cu) in 0.3 M lithium chloride.

Pt, Ag, and Au wires (250 µm in diameter) were obtained from Aldrich. Ni screen was obtained from S. Szpak. Prior to use, the metal screen and wires were rinsed in dilute nitric acid and air dried. Uranium wire (500 µm in diameter) was obtained from Goodfellow and was used as received.

2.2 Electrolysis Experiments

2.2.1 Electrolytic cells

Two kinds of cells were used in these experiments – a glass cell and a plastic cell. A description of the cells and electrodes are provided.

2.2.1.1 Glass cell

Figure 2.2-1 shows photographs of the glass cell. The cell is comprised of a large-mouthed, round bottom, 50 mL flask with a 45/50 ground glass joint (Ace Glass, p.n. 9448-05). The top has six pass-throughs for the anode, cathode, two thermistors (YSI, Inc., p.n. 55006), heater, and combined gas vent and fill tube with luer lock for the syringe. Polyethylene heat shrink tubing is used to hold the cell components in place in the pass throughs.

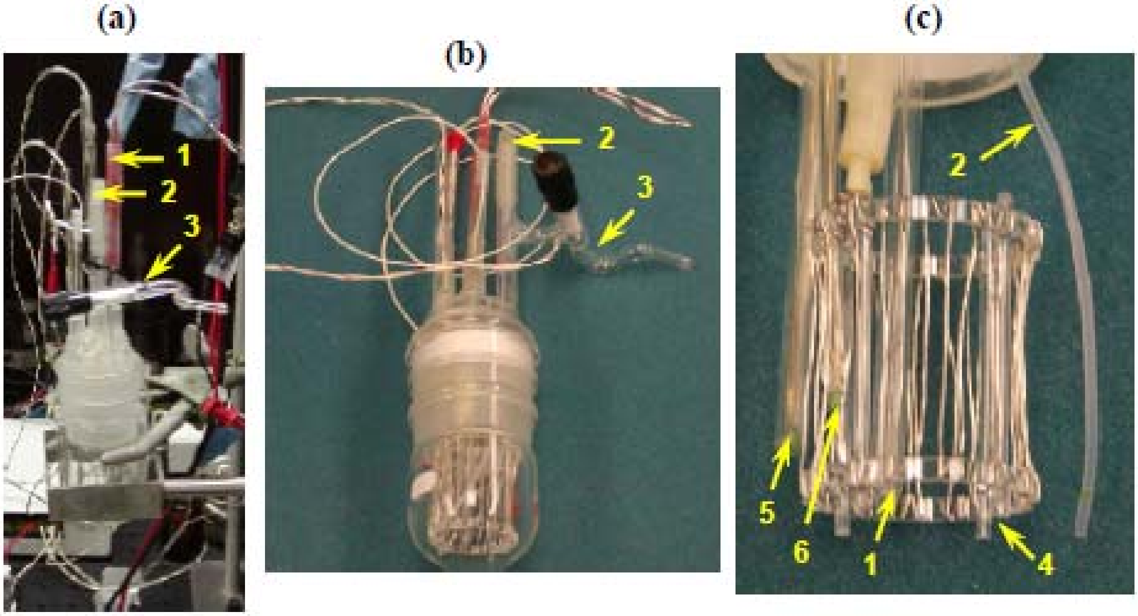

Figure 2.2-1. Photographs of the cell (a and b) and the insert (c) where 1 = heater, 2 = Teflon fill tube with luer lock, 3 = vent, 4= Pt anode, and 5,6 = thermistors in NMR tubes.

Figure 2.2 shows a photograph of the cathode. A thermistor is placed inside a glass NMR tube that is potted inside a glass tube. A Pt wire is also potted inside the glass tube, Figure 2.2. This Pt wire provides Ohmic contact to the cathode wire or screen. Polyethylene heat shrink tubing provides a pressure contact between the Pt lead and the cathode wire or screen.

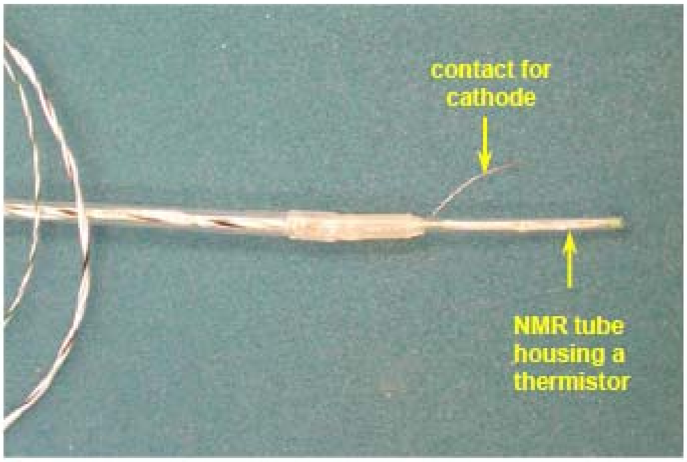

Figure 2.2.-2 Photograph of the cathode used with the glass cell.

2.2.1.2 Plastic cell

Figure 2.2-3a shows a photograph of a cathode. The support is made out of polyethylene. In this particular example, the cathode is an Ag wire that extends across the CR-39 detector (in this photograph, the CR-39 detector retains its blue, 60 µm thick polyethylene cover). As will be discussed *vide infra*, the presence of a thin layer of water greatly impacts the energy of the charged particles. Consequently, the CR-39 detector needs to be in close proximity to the detector. Polyethylene heat shrink is used to establish Ohmic contact between the Pt lead wire and the Ag wire onto which the Pd/D co-deposition will take place.

Figure 2.2-3b shows a schematic of the plastic cell used in the Pd/D co-deposition experiments. This schematic shows the placement of the anode and cathode inside the cell. The anode is a Pt wire (either 0.5 or 0.25 mm diameter) that is weaved onto a polyethylene support as shown in Figure 2.2-3b A photograph of a fully assembled cell prior to use is shown in Figure 2.2-3c. A polyethylene strip is used as a spring to separate the anode and cathode.

The plastic cells used in these experiments are made of butyrate. Each cell has dimensions of 1.125 in L x 1.125 in W x 2.5 in H and a wall thickness is 0.0625 in. Consequently the inside diameter of the cell is 1 in x 1 in. These cells have been used in these experiments because they are inexpensive, they are readily available, and they can be easily modified to perform a given experiment. Such modifications include construction of a double chamber cell to separate the anode from the cathode, inclusion of T-type thermocouples inside the cell, and constructing cells with 6 µm thick Mylar film windows. Schematics of these cell modifications will be shown *vide infra.*

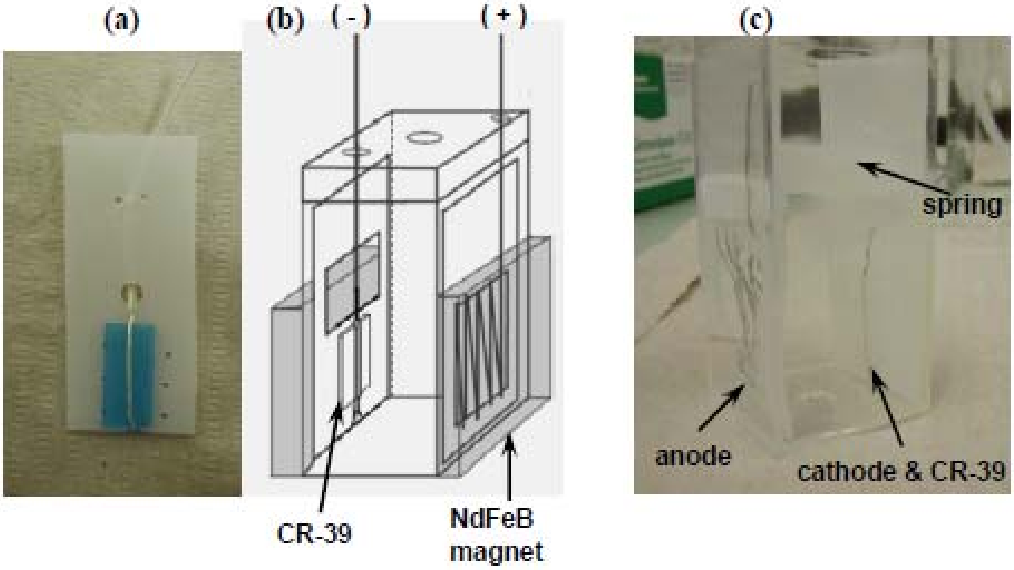

Figure 2.2-3. (a) Photograph of a cathode and CR-39 detector used inside a plastic cell. The CR-39 detector has its blue polyethylene cover on. (b) Schematic of a plastic cell. (c) Photograph of the plastic cell. The blue cover on the CR-39 detector has been removed.

2.2.2 Hardware/software used to operate cells

Figure 2.2-4 shows photographs of the hardware used to conduct the electrolysis experiments. The computer (4 in Figure 2.2-4a) has the Microsoft XP operating system and the National Instruments PCI-GPIB/LP, NI-488.2 board. The National Instruments USB-6251 multifunctional DAQ (8 in Figure 2.2-4c) and the SCB-68 connector block (9 in Figure 2.2-4c) connects to the computer via an USB. The leads to the thermistors (measure T), heater (measure V), and glass cell (measure V and I) are connected to the connector block. The heater current is measured using the Keithley 175A autoranging multimeter (1 in Figure 2.2-4a), which is connected to the PCI-GPIB/LP, NI-488.2 board inside the computer. The BK Precision DC power supply (3 in Figures 2.2-4a and b) provided the power to the heater used in the glass cell. The Kepco (2 in Figure 2.2-4a) is used to apply power to the glass cell. A Labview based program obtained from Energetics Technologies was used to control the electrolysis and do the data acquisition.

For the plastic cells, either the PAR 363 potentiostat (5 in Figure 2.2-4b) or the PAR 362 scanning potentiostat (6 in Figure 2.2-4b) was used to control the electrolysis. Data acquisition (T from the T-type thermocouples, cell voltage, and cell current) was done using the LoTech Personal DAQ/56 (7 in Figure 2.2-4b). The LoTech Personal DAQ connects to the computer via an USB.

2.3 Nuclear Diagnostics

In 1989, the Department of Energy (DoE) conducted a review of the phenomenon. The conclusions of the review were that the claims of excess heat were not convincing, that the excess heat was not shown to be associated with a nuclear process, and that the evidence of neutron emission was not persuasive. In the aftermath of the DoE review, it was concluded that heat was not going to convince anyone that nuclear events were occurring inside the palladium lattice. Also heat does not provide any information as to the processes occurring inside the Pd lattice. For these reasons, the emphasis of the research done as SSC-Pacific shifted from heat to looking for nuclear emissions such as γ -/X-rays and tritium.

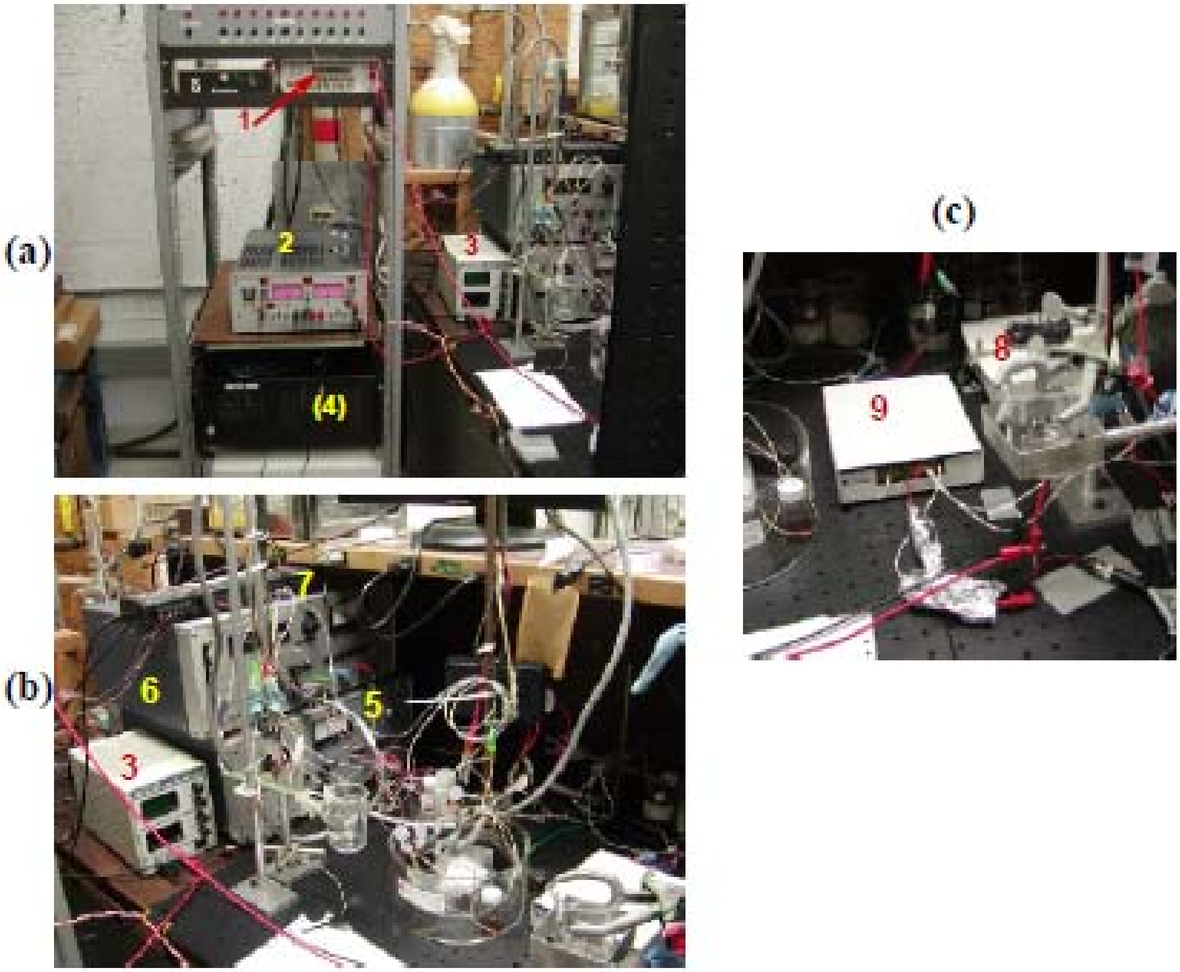

Figure 2.2-4. Photographs of the hardware used to operate the cells where 1 = Keithley 175A autoranging multimeter, 2 = Kepco BOP50-2M, 3 = BK model 1735 DC power supply, 4 = computer, 5 = PAR 363 potentiostat, 6 = PAR 363 scanning potentiostat, 7 = LoTech Personal DAQ/56, 8 = NI USB-6251 multifunctional DAQ, and 9 = NI SCB-68 connector block

In this DTRA funded effort, the nuclear diagnostics used in these experiments were CR-39 to detect neutrons and charged particles, bubble detectors to detect neutrons, NaI(Tl) and HPGe detectors for the measurement of γ- and X-rays, silicon barrier detector for charged particle measurements, and liquid scintillator for the detection of α-, β-, and γ- emitters.

2.3.1 CR-39

CR-39, a polyallydiglycol carbonate polymer, is a solid state nuclear track detector (SSNTD) that is widely used in the inertial confinement fusion (ICF) field. As a charged particle traverses through the plastic, it creates along its ionization trail a region that is more sensitive to chemical etching than the rest of the bulk. After treatment with an etching agent, tracks remain as holes or pits in the plastic. The size and shape of the tracks provide information as to what type of particle created the track as well as its energy.

Fukuvi CR-39 was used in these experiments. At the end of the experiment, the detectors were etched in 6.5 M NaOH solution. Figure 2.3-1a is a photograph showing how the detectors are etched. An Erlenmeyer flask of water is used as the heating bath. Figure 2.3-1b shows a close-up of the Erlenmeyer flask. A test tube containing the etching solution is immersed in the water. A thermometer is in contact with the etching solution. When the temperature of the etching solution gets to between 62-65°C, the detector is dropped inside the test tube and is etched for 6-7 h. After etching, the detector is rinsed in water, then in vinegar, and again in water.

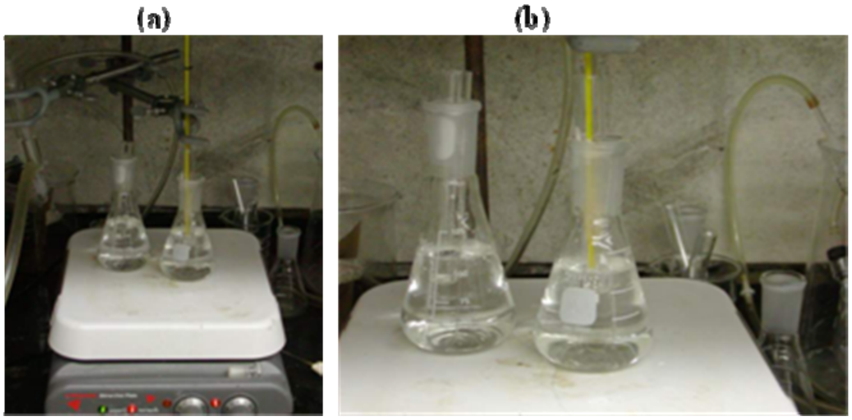

Figure 2.3-1 (a) Photograph of the set-up used to etch the CR-39 detectors at the end of an experiment. (b) Close-up of the Erlenmeyer flask.

Microscopic examination of the etched CR-39 detectors was done using an Eclipse E600 epifluorescent microscope (Nikon) and CoolSnap HQ CCD camera (Photometrics). The software used to obtain the images was MetaVue (MDS Analytical Technologies). Figures 2.3-2 and b show images of alpha tracks obtained using the Eclipse E600 microscope.

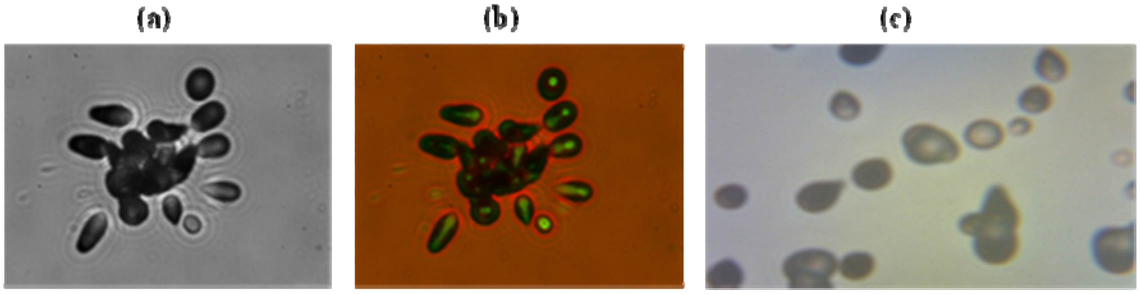

Figure 2.3-2. Images of uranium alpha tracks obtained using the Eclipse E600 microscope at 1000x magnification where (a) was obtained with the microscope optics focused on the surface of the detector and (b) is an overlay of two images obtained at different focusing depths (surface of the detector and the bottom of the pits). (c) Uranium alpha tracks obtained using the Konus Campus microscope at 1500x magnification.

It is essential that a microscope with high quality optics and imaging system be used in the analysis of the CR-39 detectors. Figure 2.3-2c shows an image of uranium alpha tracks obtained using a Konus Campus binocular microscope and Moticam 1000 microscope camera. Compared to the images shown in Figure 2.3-2a, the alpha tracks shown in Figure 2.3-2c are blurry and no diffraction rings are observed. High quality optics and imaging are particularly important in detecting and identifying tracks due to >10 MeV protons and alpha particles, which are < 2 μm in diameter.

Scanning of the CR-39 detectors was done using a TASL[i] automated scanning track analysis system to obtain quantitative information on the pits produced in the CR-39. The system has a high quality microscope optical system (Nikon cfi series) operating at a magnification high enough to discriminate between tracks and background. The images obtained are then analyzed by the proprietary software. The software makes 15 characteristic measurements of each feature located in the image to provide reliable discrimination between etched tracks and background features present on or in the plastic detectors. These measurements include track length and diameter, optical density (average image contrast) and image symmetry. Based upon the measured properties of a feature, the software of the automated scanning system determines whether or not the measured features are consistent with that of an energetic particle. The software ignores overlapping tracks.

2.3.2 Bubble detectors

Figure 2.3-4 shows a photograph of bubble detectors (BTI) that have (bottom detector) and have not (top detector) been exposed to neutrons. Inside the detector, tiny droplets of superheated liquid are dispersed throughout a clear polymer. When a neutron strikes a droplet, the droplet immediately vaporizes, forming a visible gas bubble trapped in the gel. The number of droplets provides a direct measurement of the tissue-equivalent neutron dose. The efficiency of bubble detector for neutrons is 10^{-5}. The bubbles can be recompressed between measurements. While easy to use, these detectors have a limited lifetime of use (~ 3 months).

Figure 2.3-4. Photograph of bubble detectors that have (bottom) and have not (top) been exposed to neutrons.

In the experiments that used these detectors to detect neutrons, a bubble detector is placed near the cell and another one is placed in a nearby room to monitor the background. The bubbles resulting from the experiment and the background are counted daily. To determine the average number of neutrons produced during a day, a probability analysis is done. In the case of 26 observations and P_0 = average number of neutrons per day, the relevant equations are:

Unnormalized binomial probability:
A1 = 1
A2 = -1*A1*0.00001/0.99999*P_0
A3 = -1*A2*0.00001/0.99999*P_0
and so on to
A30 = =1*A29*0.00001/0.99999*P_0
Actual probability:
B1 = A1+A2+ … +A29+A30
B2 = B1*0.00001/0.99999*P_0
B3 = B2*0.00001/0.99999*P_0/2
and so on to
B6 = B5*0.00001/0.99999*P_0/5
Predicted number of occurrences:
Y1 = B1*26
Y2 = B2*26
Y3 = B3*26
Y4 = (1-B1-B2-B3)*26

2.3.3 Liquid scintillator

Figure 2.3-5 shows a photograph of a Beckman Coulter LS6500 multipurpose scintillation counter that was used. This particular instrument has an RS-232 interface that was hooked up to a computer that had the LS-WinConnection software suite. This software suite allows the capture of the spectral data.

Liquid and solid samples are placed in a liquid scintillating cocktail (Fisher Scintiverse E). Samples were typically counted for ten minutes. The cocktail interacts with alpha, beta, and gamma emitters. The fluor of the cocktail captures the energy of the beta particle, alpha particles, or gamma rays and is itself promoted to an excited state. The fluorescence solute decays rapidly through photon emission and transforms the energy of beta particles, alpha particles, or gamma rays to photons that can be detected by the photomultipliers of the detector.

2.3.4 Real-time γ-/X-ray measurements

Gamma ray measurements were done using either an Ortec 10% p-type HPGe with an Al window, an Ortec 65% p-type HPGe with an Al window, an Ortec 15% n-type HPGe with a Be window, or a ScintiTech 3in x 3 in (100%) NaI(Tl) detector.

Experiments using these detectors were done in Pb caves to reduce the background emissions. Photographs of cells and experimental configurations are shown *vide infra*.

Figure 2.3-5. Photograph of the Beckman Coulter LS6500 multipurpose scintillation counter.

2.3.5 Surface silicon barrier detector

An Ametek TS-SNA-300-100 surface silicon barrier detector was used. A description and schematic of the cell can be found *vide infra*. The cell was placed on top of the silicon barrier detector. Figure 2.3-6 shows a schematic how the energies of alpha particles were measured as a function of Mylar thickness. In this experimental configuration, the Mylar is used to slow down the alpha particles. The slit in the acrylic support is used to collimate the alpha particles and reduce scatter.

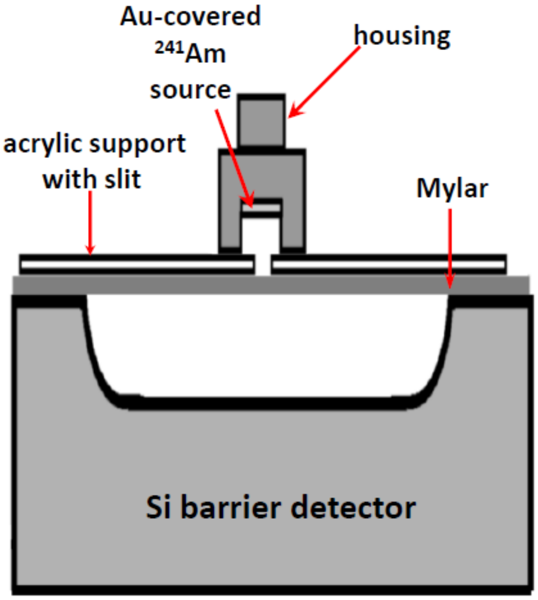

Figure 2.3-6. Schematic of experimental configuration used to measure alpha particle energies as a function of Mylar thickness.

2.4 Gas-Loading Experiments

At the time of termination of the DTRA effort, the components to do gas loading of Pd foils, Pd nanopowders, etc. had been acquired and assembled. Figure 2.4-1 shows a schematic of the gas-loading system. Photographs of the assembled system are shown in Figure 2.4-2. Table 2.4-1 summarizes the components (Swagelok) for the gas loading system.

Table 2.4-1 Components for gas-loading system.

DESCRIPTION	PART NUMBER	QUANTITY
Linde Specialty Gas regulator for H_2	UPG-3-150-660	1
316L SS Swagelok Tube Fitting, Male Connector, 1/4 in. Tube OD x 1/8 in. Male NPT (connect regulator to tubing)	316L-400-1-2	1
Brass bellows-sealed valve, 1/4 in Swagelok tube fitting	B-4HK	3
Swagelok 1/4 " union tee to connect vent, coupler, gas regulator	SS-100-3	1
Swagelok 1/16" union tee to connect sample to two valves	SS-100-3	2
316L SS Swagelok Tube Fitting, Union, 1/4 in. Tube OD to connect T to valve	316L-400-6	1
Swagelok 316 SS Double-Ended Miniature Sample Cylinder, 50 cm^3, 1000 psig (68.9 bar)	SS-4CD-TW-50	1
SS Swagelok Tube Fitting, Reducing Union, 1/4 in. x 1/16 in. Tube OD	SS-400-6-1	2

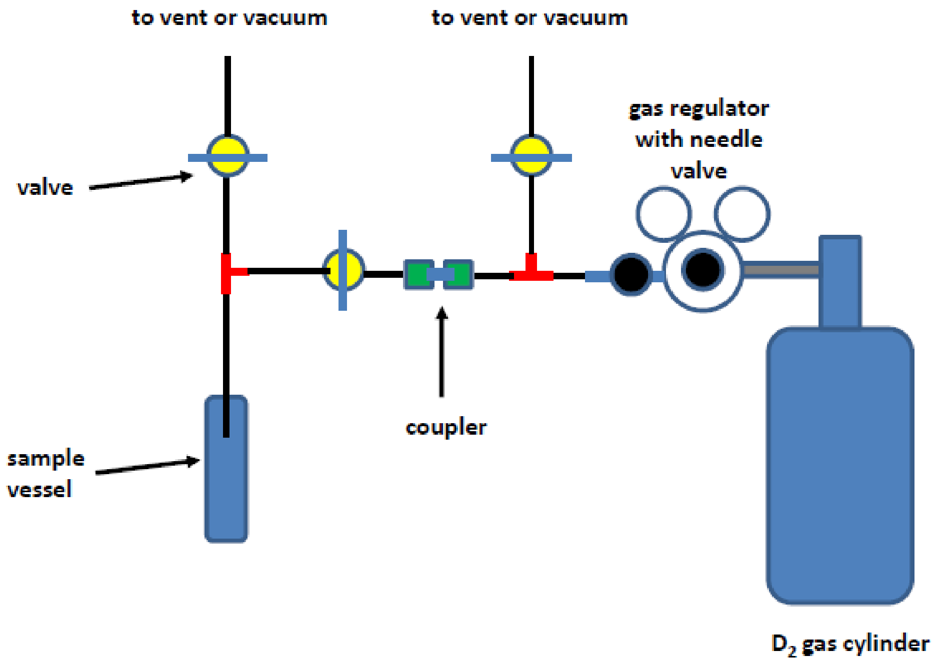

Figure 2.4-1. Schematic of the gas loading system.

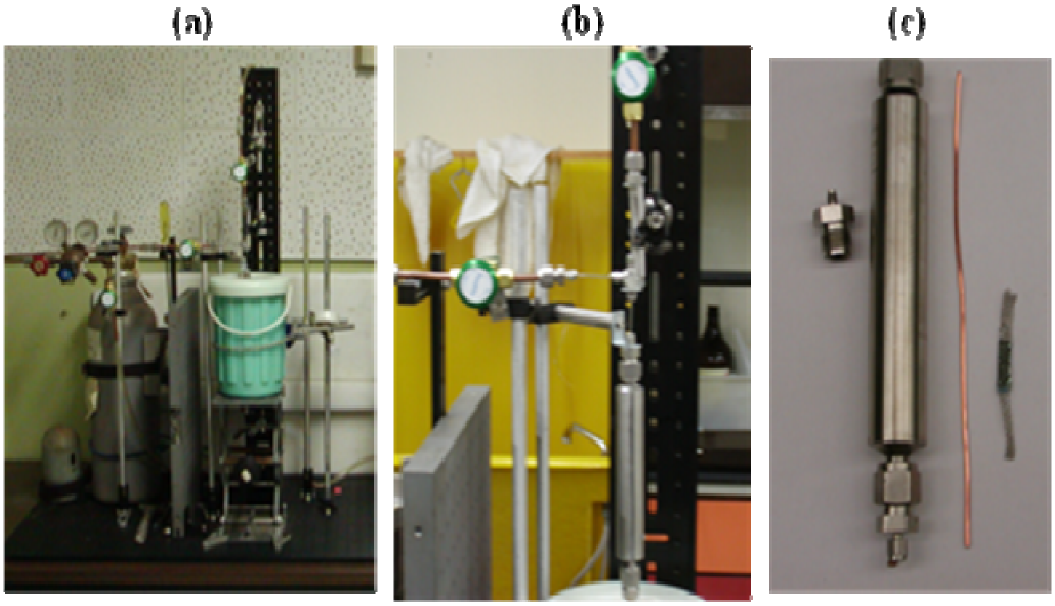

Figure 2.4-2 Photographs of (a) the entire gas loading system, (b) The part showing the valves and sample chamber, and (c) close up of the sample chamber and sample. The Pd foil is held in contact with a CR-39 detector by Ni screen. The Ni screen is then wrapped around the Cu support.

2.5 Modeling

LET calculations were done using SRIM freeware downloadable from http://www.srim.org/. Modeling of alpha tracks was done using freeware Track_Test that is downloadable from http://www.cityu.edu.hk/ap/nru/test.htm. Spectral manipulation was done using GRAMS/AI (Thermo Galactic).

3.0 SUMMARY OF RESULTS

3.1 Analysis of the CR-39 Detectors used in the SRI Replication of the SSC-Pacific Co-Deposition Experiment

3.1.1. Introduction

In 2007, SRI did replications of the SSC-Pacific Pd/D co-deposition experiment using CR-39 detectors. The SRI experiments were done with the CR-39 solid nuclear track detectors either inside the cell in contact with the cathode or outside the cell. Figure 3.1-1 shows schematics of the cell and cathode used in the immersion experiments. The detectors used in the immersion experiments were designated 10-5 and 10-6. In the outside the cell experiments, the CR-39 detector and cathode were separated by a 6 µm thick Mylar film. This detector was designated 10-7. Upon completion of the experiments, the etched CR-39 detectors were subjected to either microscopic examination that was done by Mosier-Boss (SSC-Pacific), scanning using an automated scanner which was done by Forsley (JWK), sequential etching analysis done by Lipson and Roussetski (Russian Academy of Sciences), or linear energy transfer (LET) spectrum analysis done by Zhou (NASA).

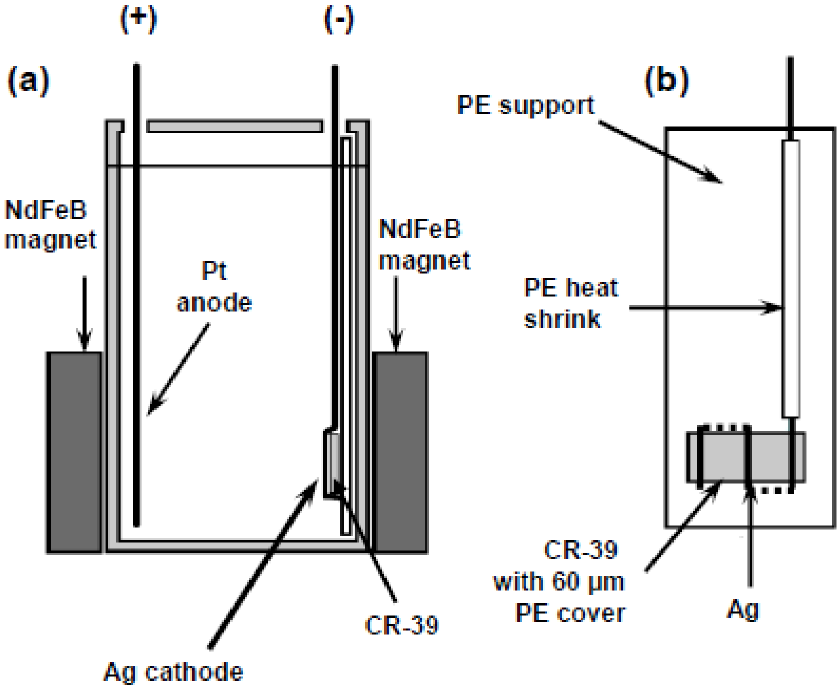

Figure 3.1-1. Schematics of the (a) cell and (b) Ag wire cathode. The continuous, single-wire cathode runs vertically over the CR-39 detector (solid lines) and under the plastic support (dashed lines) through holes in the plastic support at the top and bottom. PE = polyethyene.

3.1.2 Summary of SRI neutron and electrochemical results

A BF_3 neutron detector was also used to monitor the immersion experiments. A photograph of the detector and cells 10-5 and 10-6, inside a protective, acrylic chamber, is shown in Figure 3.1-2a. The BF_3 detector has a polyethylene Remball (the white sphere shown in the photograph). The Remball moderates the neutrons, slowing them down for capture by ^{10}B. The neutron count rate as a function of time is shown in Figure 3.1-2b. Several bursts of neutrons were observed during the first twelve days of operation. Figure 3.1-2c shows plots of the neutron count rate and cell voltage superimposed upon one another measured during the large neutron excursion that occurred on day one of cell operation. It can be seen that as the neutron count rate increased, a simultaneous decrease in the cell voltage was occurred. Such decreases in cell voltage are indicative of heat production.[21] The measured cell current/voltage profiles are shown in Figure 3.1-2d.

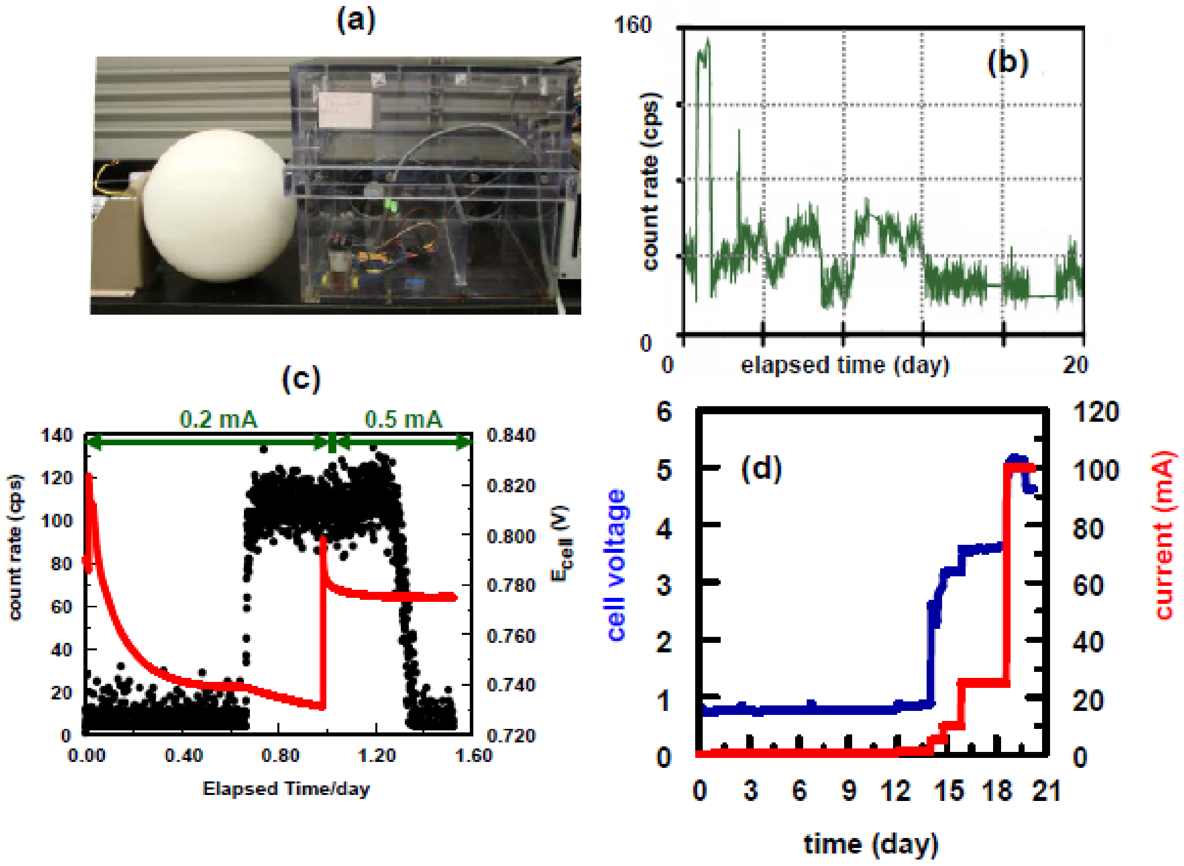

Figure 3.1-2. (a) Photograph of the cell inside the reaction chamber and the Remball/BF$_3$ detector outside the acrylic chamber. (b) Neutron count rate as a function of time. (c) Neutron count rate and cell voltage measured during the large neutron excursion. (d) Current/voltage profile.

The current profile used in the SRI replication was as follows: 100 µA for 24 h, followed by 200 µA for 48 h, followed by 500 µA until the Pd has plated out (*i.e.*, the Pd is completely plated out when the solution turns from red-brown to clear).[22] This charging profile assures good adherence of the Pd on the electrode substrate. In the SRI replication, the Pd was completely plated out by day 12. Once the Pd was plated out of solution, the cathodic current was increased to 1 mA for 48 h, 5 mA for 24 h, 10 mA for 24 h, 25 mA for 72 h, and 100 mA for 48 h as shown in Figure 3.1-2d. It has been observed that it takes considerably longer for the Pd to plate out than one would expect based upon the amount of palladium present and the number of coulombs of charge that passed to clear the solution, which indicates that the Pd has completely plated out. This indicates that there is another electrochemical reaction occurring during the plating phase. Earlier cyclic voltammetry measurements of thin Pd films on Au beads indicate that this other electrochemical reaction is the reduction of D_2O.[2,3] Figure 3.1-3a shows a schematic of the electrode used in these cyclic voltammetry experiments. Voltammograms are shown in Figure 3.1-3b. The reduction of bulk water occurs at potentials more negative than -1.2 V. However, as shown in Figure 3.1-3b, there are peaks observed in the voltammograms between -1.0 and 0.4 V. The Pd surface is catalytic and the peaks designated A, D, B, and C are attributed to deuterium atoms adsorbed on the surface of the Pd that is in contact with the water layer. Peaks A and D, formed in the cathodic sweep, are smaller than peaks B and C which are formed in the anodic sweep. The relative sizes of the peaks indicate that, as soon as deuterium is formed during the cathodic sweep, it goes inside the Pd metal lattice. Consequently, some reduction of D_2O, and with it D loading of Pd, occurs during the plating phase over the first twelve day period of the SRI experiment.

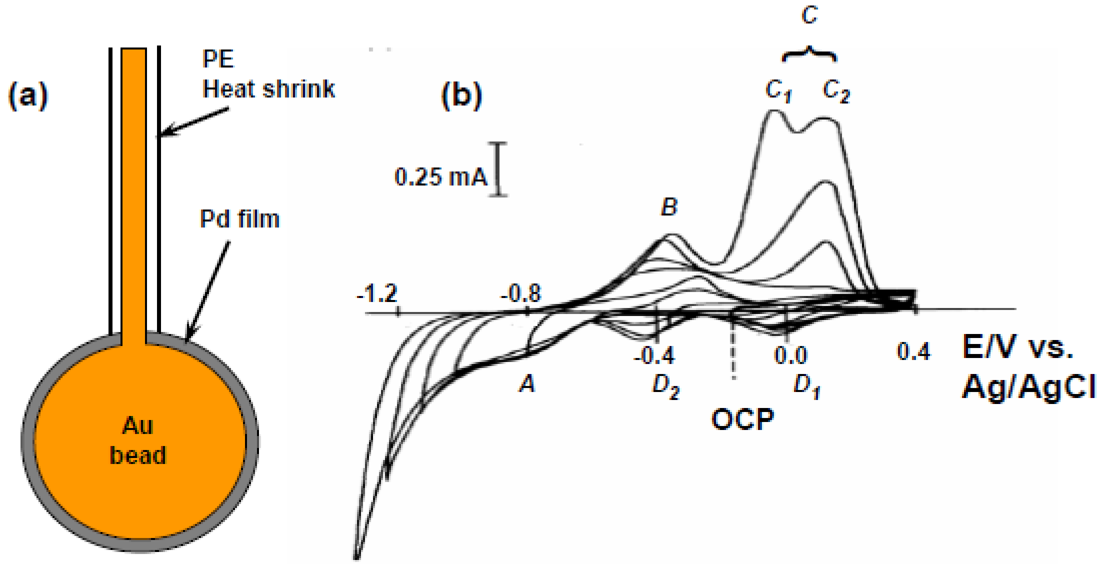

Figure 3.1-3. (a) Schematic of the thin Pd film on Au bead electrode used in the cyclic voltammetry experiments. (b) Evolution of voltammograms as a function of lower scan reversal for a fixed (+400 mV) upper limit potential, reversals at -300, -500, -700, -900, -1000, -1100, and -1200 mV. The OCP is -0.118 V *vs.* the Ag/AgCl reference electrode.

3.1.3 Summary of microscopic analysis and scanning of the CR-39 detectors used in the SRI replication

The Fukuvi CR-39 detectors come covered on both sides with a 60 µm thick polyethylene film. In the immersion experiments of the SRI replication, this film was between the cathode and the detector. Linear energy transfer (LET) calculations indicate that 60 µm thick polyethylene film will block 7 MeV alphas and 1.8 MeV protons. In addition, in the SRI replication, the magnetic field was present throughout the course of the experiment. At the end of the experiment, Fran Tanzella etched CR-39 detectors 10-5 and 10-6 and sent them to SSC-Pacific for microscopic analysis. Tracks were observed on both the front and back surfaces of both detectors. Figure 3.1-4 shows a photomicrograph of detector 10-5 obtained at 1000× magnification showing the density of tracks obtained. The image shown in Figure 3.1-4a was obtained by focusing the microscope optics on the surface of the detector. It can be seen that there are dark, circular and elliptical tracks. There are also smaller, shallower tracks that are due to either latent tracks deeper inside the plastic, or to particles that barely impact the detector, or to highly energetic charged particles. Figure 3.1-4b is an overlay image of two photomicrographs obtained at two different focusing depths (the surface of the detector and the bottom of the pits). This image shows bright spots inside the tracks. These bright spots indicate the endpoints of the particles that enter the detector and are caused by the curved bottom of the track acting like a lens when the detector is backlit.[23] The color, shape, and bright spot inside are features consistent with those observed for nuclear generated particle tracks. In Figure 3.1-4a, a triple track is circled. As will be discussed *vide infra*, such tracks are indicative of ≥ 9.6 MeV neutrons.

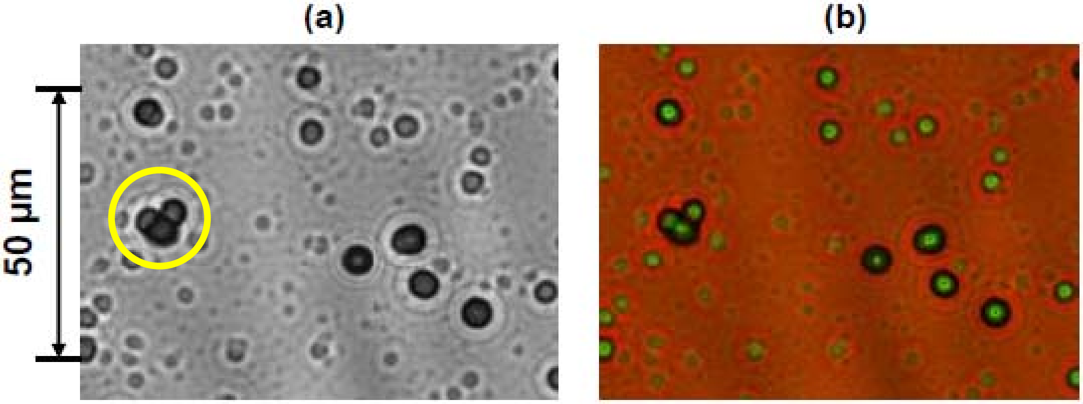

Figure 3.1-4. Photomicrograph of the CR-39 detector 10-5 used in the SRI replication obtained at a magnification of 1000x. (a) The image was taken with the microscope optics focused on the surface of the detector. (b) The image is an overlay of two images taken at different focusing depths (surface of the detector and the bottom of the tracks).

A control experiment using $CuCl_2$ in place of $PdCl_2$ was done at SSC Pac. The SRI protocol for the immersion experiment was followed in the control experiment. Specifically, a 60 μm thick polyethylene film separated the cathode from the CR-39 detector and a magnetic field was present throughout the course of the experiment. For both $CuCl_2$ and $PdCl_2$, the same electrochemical reactions occur at the anode and cathode. Specifically, oxygen and chlorine gas evolution occurs at the cathode while deuterium gas evolution and metal electroplating occur at the cathode. In addition, the resultant Cu and Pd metallic deposits exhibit similar dendritic morphologies. The only significant difference is that Pd absorbs deuterium and Cu does not. No tracks were observed for the $CuCl_2$ experiment. This experiment indicates that the tracks observed in the $PdCl_2$ experiment cannot be attributed to a chemical species diffusing through the polyethylene film that attacks the surface of the detector. If this were the case, the CR-39 detector used in the $CuCl_2$ experiment would have exhibited cloudiness and pitting, which it did not. The results also indicate that the Cu dendrites did not pierce through the polyethylene cover and into the detector. It can therefore be concluded that the observed pitting in the $PdCl_2$ system is not due to either chemical or mechanical damage of the CR-39 detector.

Figure 3.1-5a shows a photograph of the polyethylene-covered CR-39 detector 10-5 at the end of the experiment. Arrows indicate the placement of the Ag wire across the face of the detector. The dark areas on the polyethylene cover are due to the Pd deposit. These dark areas indicate that the Pd deposit extended past the Ag wires and into the areas between the wires. Ohmic measurements using probes on both sides of the film indicate that the deposit did not go through the 60 μm thick polyethylene film. These measurements indicate that the Pd dendrites did not pierce through the polyethylene film and into the CR-39 detector. Figure 3.1-5b shows a photograph of the front surface of the detector 10-5 after etching. The white, cloudy areas are due to high track density. It can be seen that the density of tracks is highest near the vicinity of the Pd-coated Ag wires indicating that the cathode is the source of these tracks.

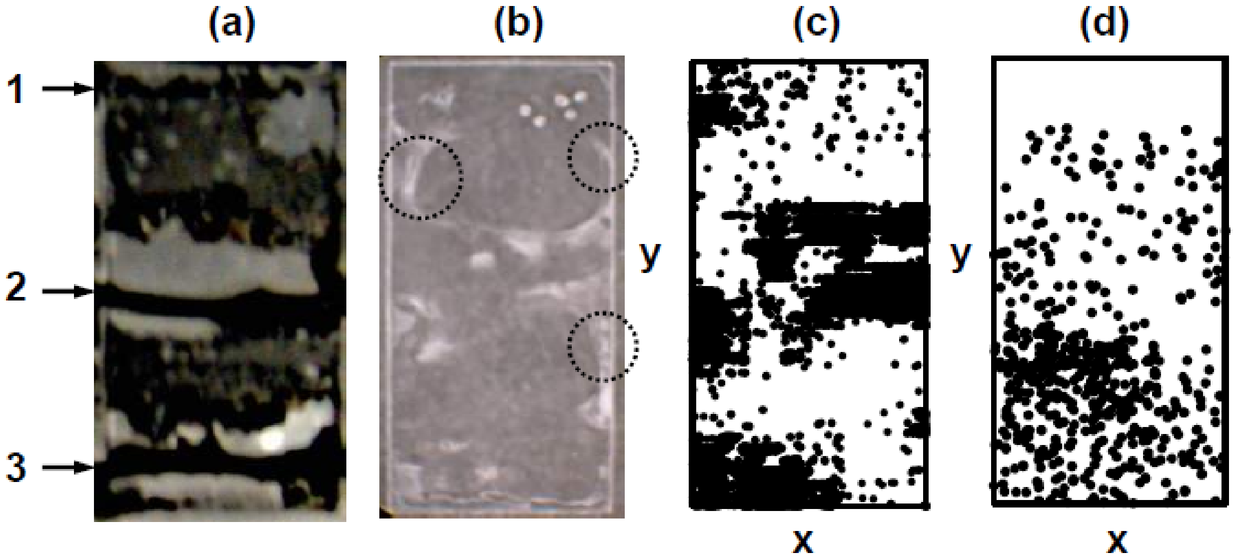

Figure 3.1-5. (a) Photograph (provided by F. Tanzella of SRI) of the surface of detector 10-5 facing the cathode obtained at the end of the experiment. The polyethylene cover is on the surface of the detector. Arrows indicate the placement of the Ag wires, which are numbered. (b) Photograph (provided by F. Tanzella of SRI) of the detector 10-5 after it was etched. The five dots on the upper right hand corner were created by pushing a pin into the detector. These marks indicate which side of the detector was facing the cathode. Circled areas indicate a high density of tracks. Scanned results of the detector that shows the spatial distribution of tracks on the (c) front and (d) back surfaces of the detector.

Both detectors used in the immersion experiments, 10-5 and 10-6, were then sent to JWK where Larry Forsley had both detectors scanned with an automated scanning track analysis system to obtain quantitative information on the pits in the CR-39. The proprietary software makes 15 characteristic measurements of each feature located in the image to provide reliable discrimination between etched tracks and background features present on or in the plastic detectors. These measurements include track length and diameter, optical density (average image contrast) and image symmetry. Based upon the measured properties of a feature, the software of the automated scanning system determines whether or not the measured features are consistent with that of an energetic particle. The software algorithms ignore overlapping tracks. The spatial distribution of positively identified tracks for the front and back surfaces of detector 10-5 are shown in Figures 3.1-5c and 5d, respectively. In the photograph shown in Figure 3.1-5b, three cloudy areas are circled. Microscopic examination of these areas showed numerous overlapping tracks. The track density was too high for the scanner to accurately measure the contrast and size of the individual tracks. This is why no tracks have been identified by the scanner in these cloudy areas. On the backside of the detector, the identified tracks are not clearly associated with any of the wires. However, the density of tracks is greatest between the second and third wires. Looking at the photograph in Figure 3.1-5a, it appears that the density of the Pd deposit is greater between wires 2 and 3.

Figure 3.1-6 summarizes the scanned results obtained for a blank CR-39 detector. Both the front and back surfaces of the detector were scanned. For the blank detector, 147 tracks were observed on the front surface and 166 tracks on the back. The size distributions of the front and back surfaces of the blank detector are shown in Figures 3.1-6a and 3.1-6c, respectively. For both surfaces, there is a distribution of tracks between 1 and 5 μm in diameter and a second distribution between 6 and 40 μm in diameter. As discussed *vide supra*, the 60 μm thick polyethylene film on the detector will block 7 MeV alphas and 1.8 MeV protons. The tracks in the 1-5 μm range are likely due to very energetic protons with an estimated energy ≥10 MeV. Protons with this energy will be able to pass through the polyethylene film and would leave a small diameter track in the CR-39 detector. Oda *et al.*[24] did sequential etching of CR-39 exposed to 10 MeV protons. The track diameters were 1.0 and 2.6 μm after removing 6.5 and 15 μm of plastic, respectively. It is unlikely that the tracks in the 6-40 μm size range are due to alpha particles given that the polyethylene film blocks alphas with energies ≤ 7 MeV. These tracks are most likely recoils resulting from cosmic ray spallation neutrons interactions with the constituents of the detector, *i.e.* proton, carbon, and oxygen atoms. CR-39 detectors do not respond to thermal neutrons. Neutrons that are 1-6 MeV in energy will result in tracks with sizes ranging between 5 and 30 μm is diameter.[25] Neutrons with energies greater than 8 MeV will produce tracks in CR-39 with diameters ≥30 μm. Plots of minor *vs.* major axis of the tracks

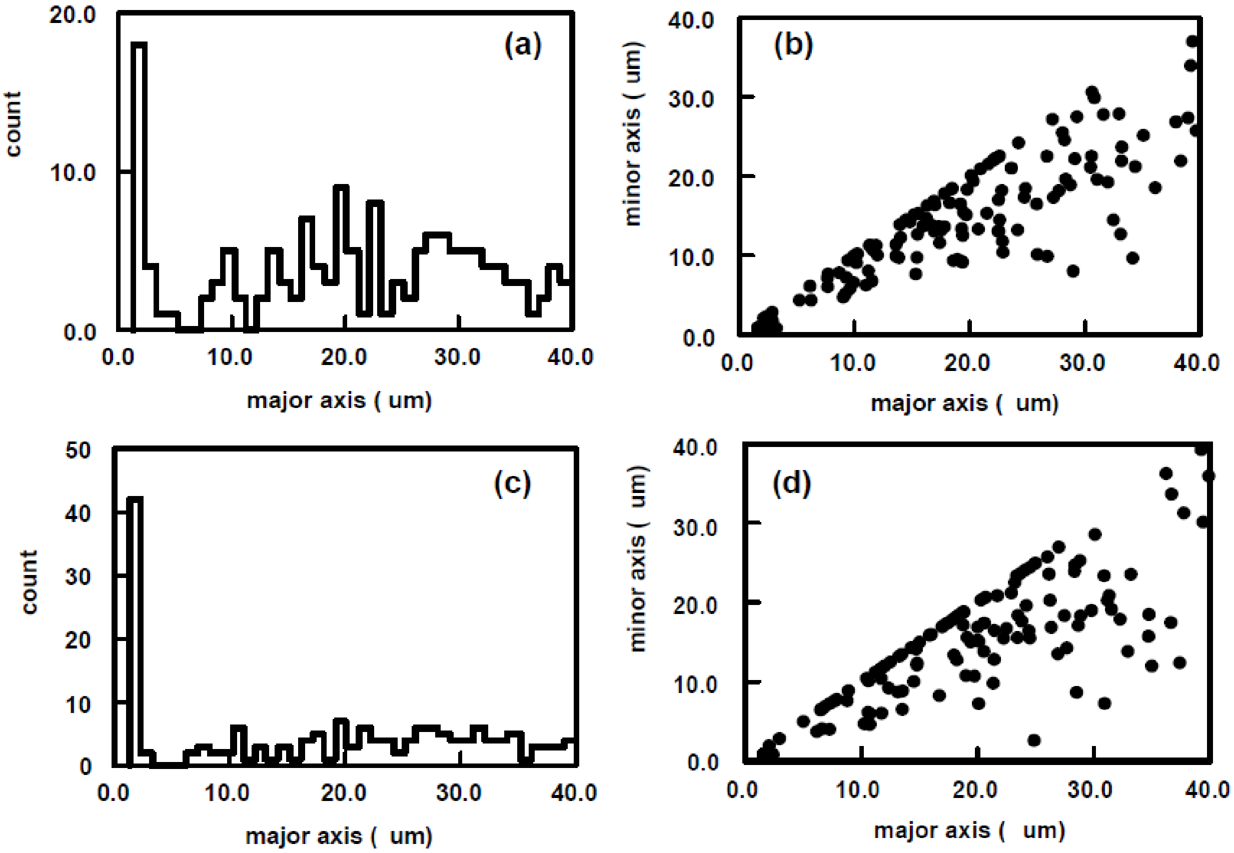

Figure 3.1-6. Scanned results obtained for a blank CR-39 detector. Front surface (147 tracks): (a) size distribution and (b) plot of minor axis and major axis. Back surface (166 tracks): (c) size distribution and (d) plot of minor axis and major axis.

observed on the front and back surfaces are shown in Figures 3.1-6b and 3.1-6d, respectively. The plots show that the majority of the tracks exhibit ellipticity indicating that the particles have entered the detector at angles less than 90º.

Figure 3.1-7 summarizes the scans of the front and back surfaces of the CR-39 detector 10-5 used in the SRI replication. The size distributions of tracks on the front and back surfaces of detector 10-5 are shown in Figures 3.1-7a and 3.1-7c, respectively. The number of tracks on the front and back surfaces are significantly greater than what was observed on the blank detector. On the front surface, 34254 tracks were positively identified. Two size distributions are observed: 0 to 3.5 µm and 3.5 to 20 µm in diameter. As can be seen in Figure 3.1-7a, the majority of the tracks (~70%) fall in the 0-3.5 µm size range. For the tracks in the 3.5-20 µm size range, the peak maximum occurs at 6.7 µm. A plot of minor *vs.* major axis of the tracks on the front surface is shown in Figure 3.1-7b. The line along the diagonal, where the minor and major axis are equal, represents particles that have entered the detector at a 90º angle. The majority of the tracks fall in the circled area. In this region, the major axis is larger than the minor axis indicating that these particles entered the detector at oblique angles. On the back surface, 750

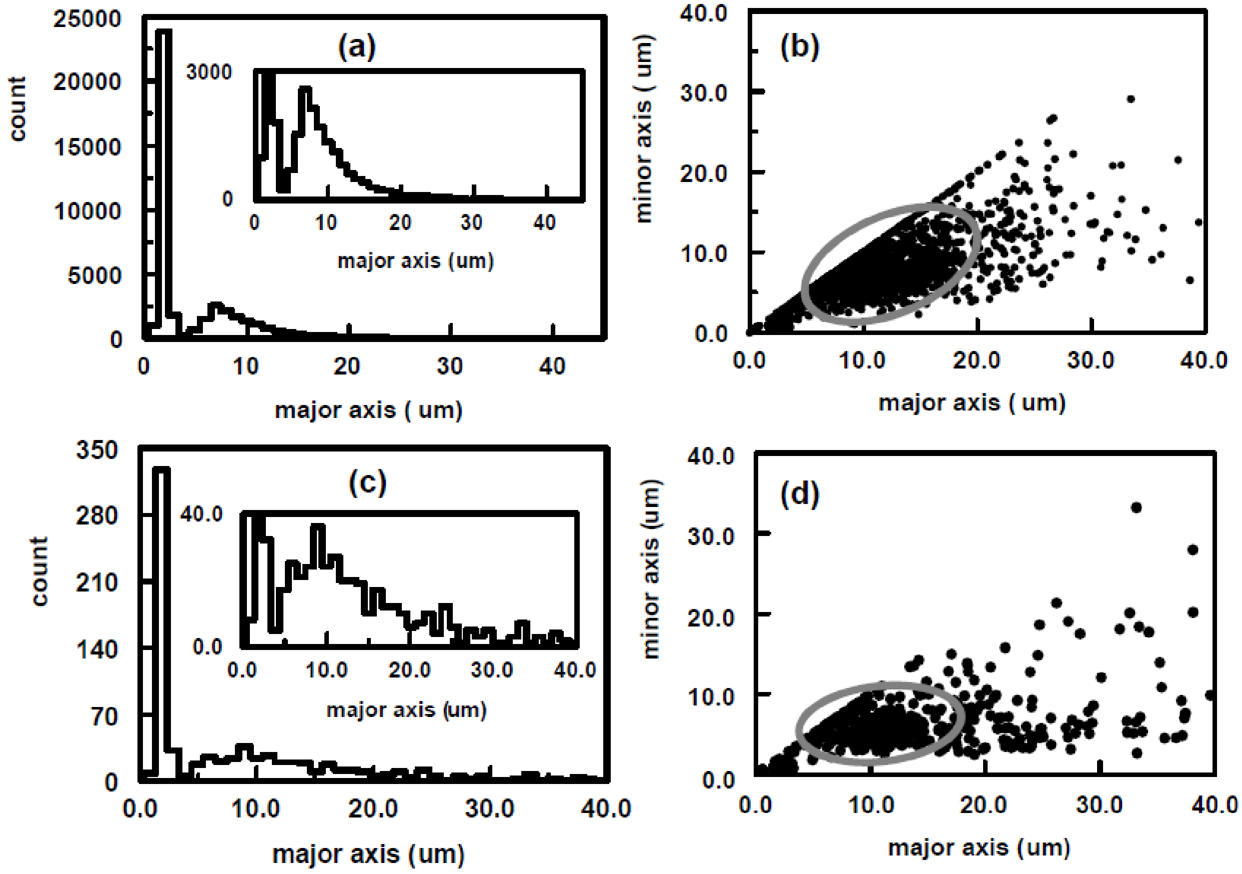

Figure 3.1-7. Scanned results obtained for the CR-39 detector 10-5 used in the SRI replication. Front surface (34,254 tracks, spatial distribution of tracks shown in Figure 4c): (a) size distribution and (b) plot of minor axis and major axis. Back surface (750 tracks, spatial distribution of tracks shown in Figure 4d): (c) size distribution and (d) plot of minor axis and major axis. In (b) and (d), the circled areas indicate the bulk of the tracks.

tracks were identified by the scanner. Approximately 40% of those tracks fall in the 0-3.5 µm size distribution. The remainder of the tracks fall in the 3.5-40 µm size range with the peak maximum occurring at 8.8 µm. Figure 3.1-7d shows the plot of minor *vs.* major axis for the tracks identified on the back surface. The majority of the tracks fall in the circled region. Compared to the front surface, the tracks on the back surface exhibit greater ellipticity indicating that the angles of incidence are more acute. The scanned results of detector 10-6 were similar to that obtained for detector 10-5.

In the SRI replication, the 60 µm thick polyethylene film separated the detector from the cathode. Given the presence of the polyethylene film and the small size of the tracks, the 0-3.5 µm diameter tracks on the front surface are attributed to ≥ 10 MeV protons. On the back side, the 0-3.5 µm diameter tracks are likely due to protons that have gone all the way through the CR-39 detector. LET calculations indicate that, to go through 1 mm thick CR-39, the proton needs an energy of 10 MeV. To get through both the 60 µm thick polyethylene film as well as the 1 mm thick CR-39 detector, the proton energy needs to be ≥ 11.8 MeV.

Identification of the particles causing the 3.5-20 µm diameter tracks on the front surface is complicated by the presence of the 60 µm thick polyethylene film between the detector and the cathode. The polyethylene film allows ≥ 1.8 MeV protons and ≥ 7 MeV alphas through. Lipson *et al.*,[26] using 50 µm thick Pd foils in contact with CR-39 and Al and Cu spacers, detected the emission of 11-16 MeV alpha and 1.7 MeV protons during electrolysis. However, the tracks could be due to knock-ons that are registered in the CR-39 detector as the energetic protons pass through the polyethylene film. The resultant tracks from these knock-ons would be larger than the tracks from the protons themselves. The tracks could also potentially be due to recoils from neutron interactions with the polyethylene film. Neutrons that are ≥0.25 MeV in energy would result in tracks that are 5-20 µm is diameter.[25] As indicated *vide supra*, the majority of the tracks on the back surface are 3.5-40 µm in diameter. These tracks could be due to recoils from either neutrons or the energetic protons. Analysis using sequential etching and LET spectrum analysis, provided additional information as to the identity and energy of the particles that produced the tracks on the front and back surfaces of the CR-39 detector used in the SRI replication.

3.1.4 Summary of sequential etching analysis of the CR-39 detectors used in the SRI replication

After scanning detectors 10-5 and 10-6, they were sent to the Russian Academy of Sciences for further analysis by Roussetski and Lipson. They had developed a sequential etching method that could be used to identify and determine the energies of energetic proton and alpha particles.[27] They also analyzed blank detectors as well as detector 10-7, which had been placed outside the cell in a magnetic field experiment. In this particular experiment, a 6 µm thick Mylar film separated the detector and the cathode.

CR-39 detectors were calibrated using alpha sources (in the range of 1.6 - 7.7 MeV) and by exposing them to monoenergetic cyclotron alpha-beams (in the energy range of 10 – 30 MeV). Detectors were also calibrated with Van de Graaff accelerator producing monoenergetic proton beams (energy range of 0.75-3 MeV). Only circular tracks are used to generate calibration curves. These tracks are created by charged particles with trajectories normal to the surface of the detector. Figure 3.1-8 shows alpha and proton calibration curves.

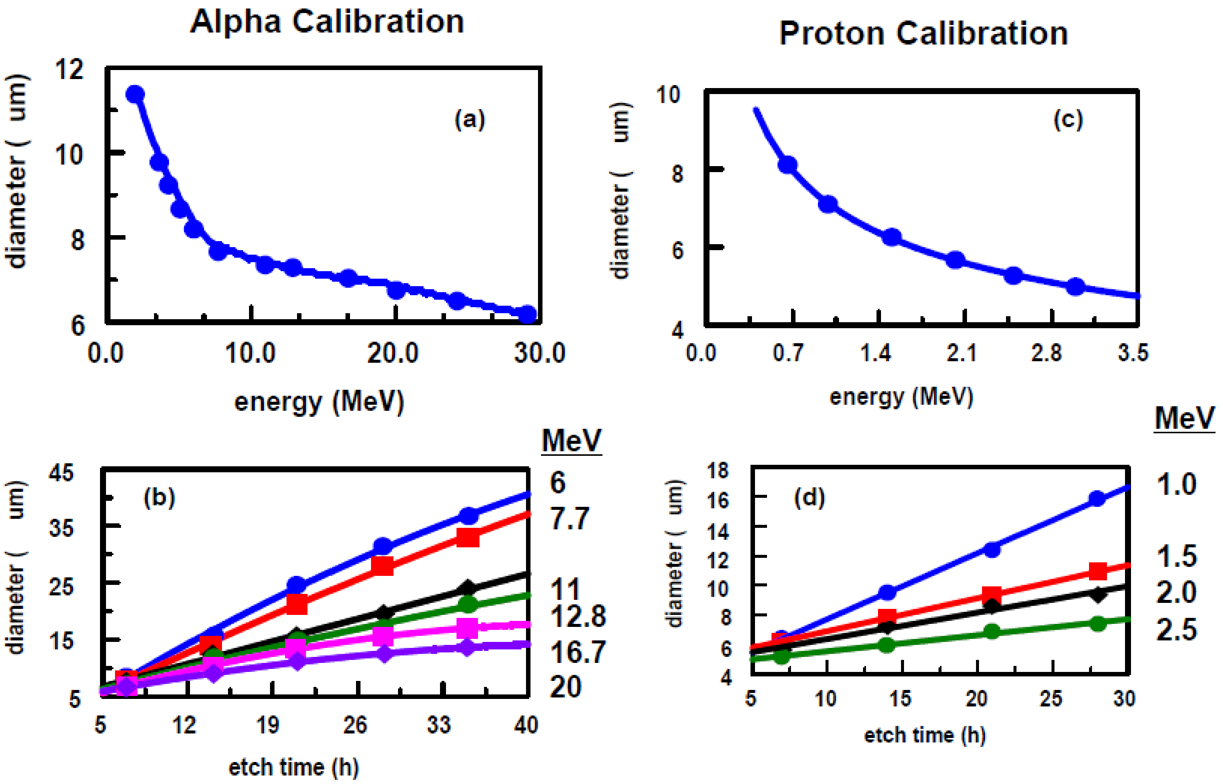

Figure 3.1-8. Calibration curves generated for energetic alpha and proton particles. (a) Alpha track size as a function of energy (7 h etch). (b) Track diameter *vs.* etching time for six different alpha energies. (c) Proton track size as a function of energy (7 h etch). (b) Track diameter *vs.* etching time for four different proton energies.

Significant results of the sequential etching are summarized in Figure 3.1-9. Sequential etching of detector 10-7 showed proton recoil tracks. Figure 3.1-9a shows the proton recoil spectrum obtained for detector 10-7. It is compared to the proton recoil spectrum obtained for ^{252}Cf neutrons. This comparison shows that detector 10-7 has been exposed to 2.3-2.45 MeV neutrons. The neutron emission rate was estimated to be 1-3 n/s. Blank detectors did not show proton recoils inside the detector indicating that the source of the neutrons observed in detector 10-7 was the Pd/D deposit on the Ag cathode. Figure 3.1-9b shows the spectrum obtained for the front side of detector 10-5 after 21 h of etching. The tracks are identified to be due to 3 MeV protons and alphas of energies of 12 and 16 MeV.

3.1.5 Summary of LET spectrum analysis of CR-39 detectors used in the SRI replication

Dazhong Zhou, of NASA-Johnson Space Center, took the scanned data of detectors 10-5 and 10-6 that Forsley had done and analyzed them using a LET spectrum method.[28-33] Applying the LET spectrum method to the scanned data, the LET spectrum (differential and integral fluence), Figure 3.1-10, and energy distributions of the charged particles, Figure 3.1-11, were determined. For protons, a the major peak is observed at ~ 11.5 – 12 MeV for the front CR-39 surfaces and

~ 9.75 MeV for the back CR-39 surfaces. The distribution of α particles is nearly uniform because they are mainly secondary particles.

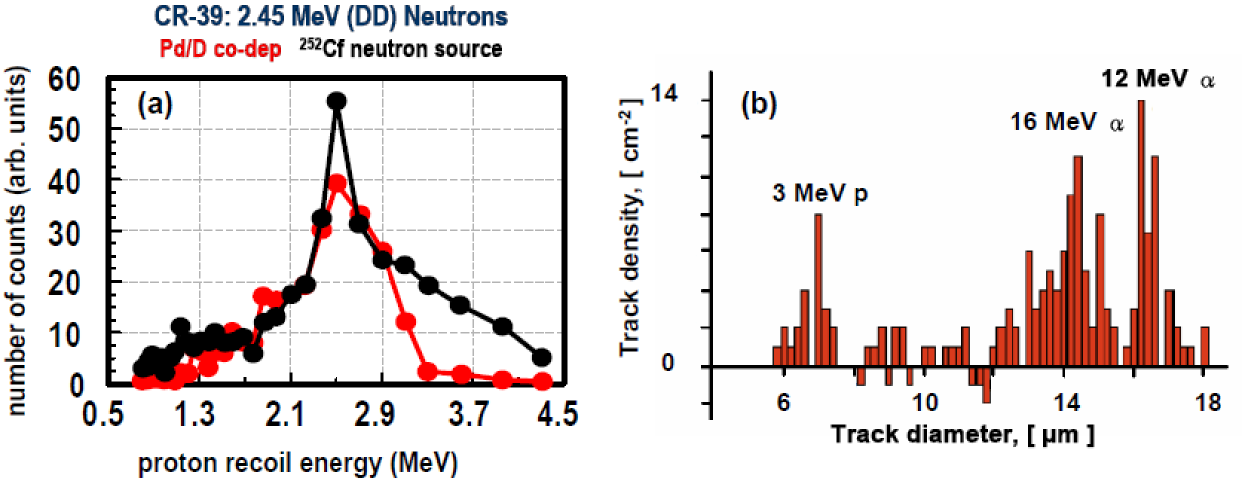

Figure 3.1-9. Results obtained for the sequential etching. (a) Reconstruction of the proton recoil spectra for detector 10-7 and a detector exposed to ^{252}Cf neutrons (etch time 14 h). (b) The front side spectrum of nuclear tracks in detector 10-5 after subtracting the neutron induced proton recoil spectrum from its back side (etch time is 21 h).

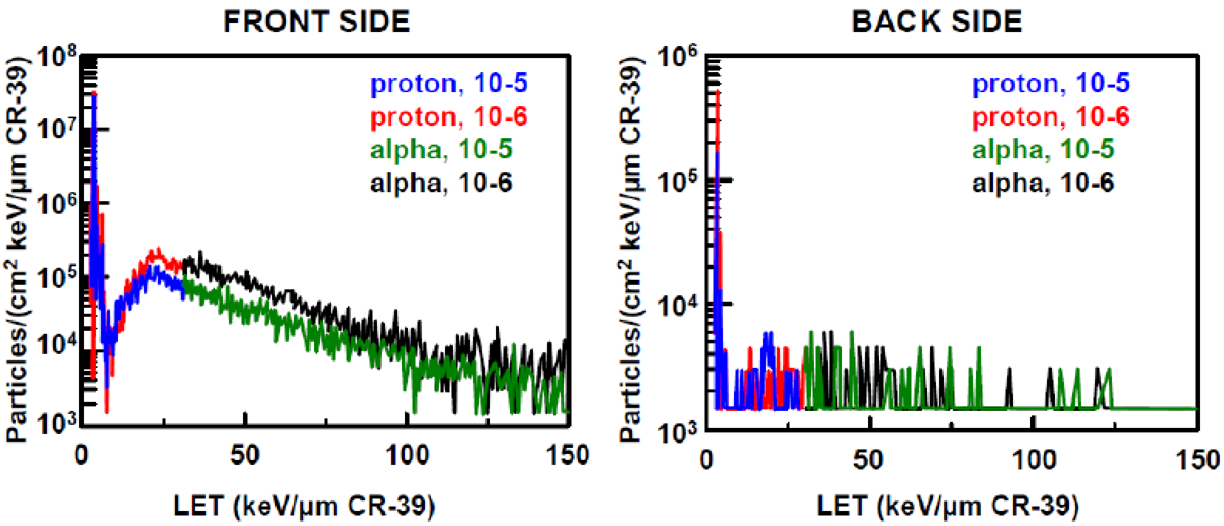

Figure 3.1-10. LET spectra of differential fluence calculated for the front and back surfaces of detectors 10-5 and 10-6. The front surface was the side closest to the cathode.

3.1.6 Conclusions

The SRI results indicated that the Pd/D co-deposition experiment with CR-39 detectors was replicable. The detectors used in the SRI experiments were analyzed, independently, by three different methods. The three analytical techniques gave complementary results. From the microscopic analysis and automated scanning results, it was concluded that there was evidence of 2.5 and > 9.6 MeV neutrons, > 10 MeV protons, and energetic alphas. The sequential etching analysis gave evidence of 2.5 MeV neutons, 3 MeV protons, as well as 12 and 16 MeV alphas. From the LET function analysis, it was concluded that there were 3-10 MeV protons, with peaks at 5.5, 6.5, 7.5, 9.5, 10.5, and > 12 MeV. The LET function analysis also showed a continuum of alpha energies. However, the tracks attributed to alphas could possibly be due to neutron recoils.

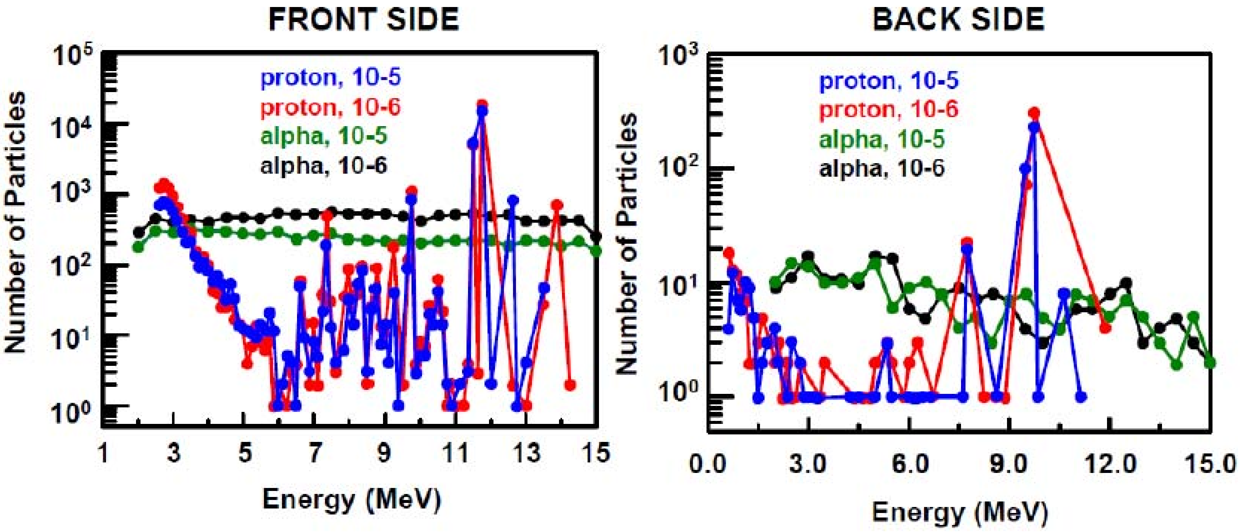

Figure 3.1-11. Energy distribution of particles calculated for the front and back surfaces of detectors 10-5 and 10-6. The front surface was the side closest to the cathode.

From the BF_3 data, it is interesting to note that the bursts of neutrons occurred during the plating phase of the Pd/D co-deposition process. Once the Pd had plated out and the current was ramped up, the neutron bursts ceased. This implies that high D loading is not necessary for neutron production, which agrees with the early BARC results.[34] The BARC experiments used $Ag_{0.25}Pd$ tubes instead of Pd rods. These tubes are connected to a plenum. In this configuration, the D ions, which impinge on the cathodes during electrolysis under the influence of the applied electric current, diffuse through the walls of the Pd-Ag tubes and escape into the gas plenum. The ions recombine inside the tubes to form molecular D_2. Consequently the BARC experiments did not achieve the high D/Pd loadings necessary for heat production. In their studies, six out of eleven cells saw a neutron signal within 9 h, one within 24 h, and two in two weeks. These results suggest that multiple channels are possible, *i.e.*, one channel results in heat and ^{4}He, another results in neutrons, and yet another tritium. The implication is that by controlling experimental parameters, it should be possible to switch back and forth over the various channels, a concept that Swartz[35] refers to as the ‘optimal operating points (OOPs).

3.2 Summary of Experiments that Rule out Chemical/Mechanical Origins for the Tracks Observed in CR-39 used in Pd/D Co-deposition Experiments

3.2.1 Summary of earlier CR-39 results

In 2007, Mosier-Boss *et al.*[22] reported on seeing tracks in CR-39 detectors used in Pd/D co-deposition experiments. The tracks were either circular or oval in shape and had bright spots in their centers when the microscope optics were focused inside the tracks. These features are diagnostic of nuclear-generated tracks. They conducted a series of control experiments that showed that the tracks were not due to chemical damage, nor were they due to the metal dendrites piercing into the plastic, nor were they due to radioactive contamination of the cell components.

Figure 3.2-1 shows photomicrographs of CR-39 obtained at 20x and 200x magnification. Figure 3.2-1a was for a CR-39 detector used in a co-deposition experiment on an Ag wire conducted in D_2O. The density of tracks is high and occur homogeneously along the Ag wire. Tthe tracks are coincident with the placement of the Pd deposit on the Ag cathodic substrate indicating that the Pd deposit is the source of the tracks. When co-deposition was done on an Ag wire in H_2O, visual examination of the detector showed sparse patches of cloudy areas along the length of the Ag wire. Figure 3.2-1b shows one such patch at a magnification of 20x. At a magnification of 200x, tracks are observed in this patch, however the density of tracks is several orders of magnitude less than was observed for co-deposition done in D_2O. These results are consistent with the reports of energetic particles for light water electrolysis experiments using thin Pd foils.[26] Visual inspection of the CR-39 detector used in the Pd wire experiment done in D_2O showed scattered cloudy areas along the length of the Pd wire. Figure 3.2-1c shows photomicrographs of one such cloudy area at 20x and 200x. Tracks are observed. The density of tracks is less than that observed for co-deposition done in D_2O but more than was observed in H_2O. It has been well documented that, in the case of bulk Pd, generation of heat, tritium, and helium does not occur homogeneously throughout the Pd.[36] This indicates that the reactions occur in localized areas within the bulk Pd. Metallurgical aspects of bulk Pd are still not fully

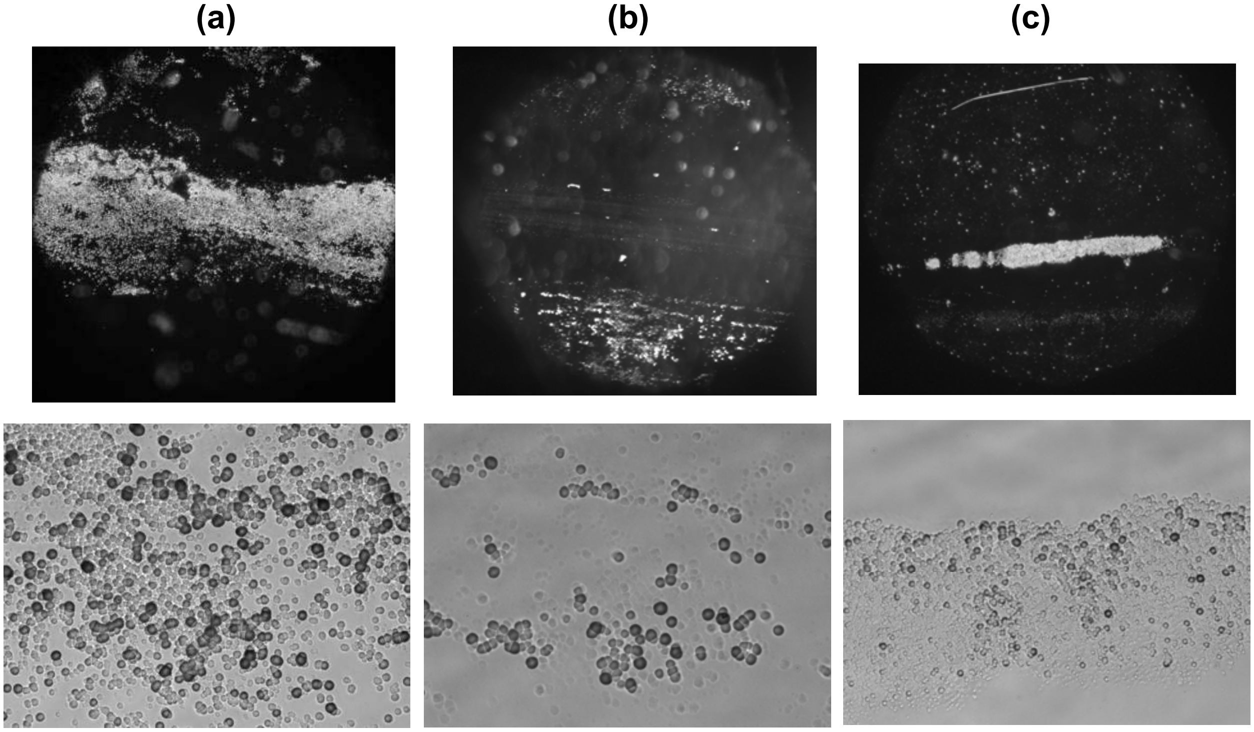

Figure 3.2-1. Photomicrographs obtained at 20x (top) and 200x (bottom) magnification for CR-39 used in (a) Ag/Pd/D co-deposition in D_2O, (b) Ag/Pd/H codeposition in H_2O, and (c) bulk Pd electrolysis in D_2O. The time duration of operation was the same for all three experiments.

understood. The CR-39 results show that some areas in the bulk Pd show greater activity than others. Another suggestion has been made that the pits observed in the CR-39 detectors are caused by the tips of the Pd dendrites formed during the Pd/D co-deposition either piercing the surface of the CR-39 or producing hydroxide ions that etch pits into the CR-39. Since pits are observed using a Pd wire which has no dendritic structure to it, neither of these suggested mechanisms of pit formation (piercing or localized etching) is valid.

Another observation made in these studies was that an external magnetic or electric field was required to obtain tracks in CR-39 when Pd/D co-deposition was done on a Ni screen.[22] The electric field used in these experiments had a 6% AC ripple which allowed the electric field to couple into the cathode. Figure 3.2-2a shows a photograph of a CR-39 detector used in Pd/D codeposition experiment done on Ni screen in the absence of an external electric/magnetic field. No tracks were observed in the CR-39 detector. Instead the impression of the Ni screen was observed. At higher magnification, hollows are observed where the Pd plated inside the eyelets of the Ni screen. The emission of X-rays has been observed for Pd/D co-deposition.[12] Figure 3.2-2b shows fogging of photographic film after a Pd/D co-deposition experiment conducted on the Ag disk of a piezoelectric crystal. The circular shape of the cathode can be seen and the emission of soft X-rays is not homogeneous over the surface of the cathode. It is therefore possible that the

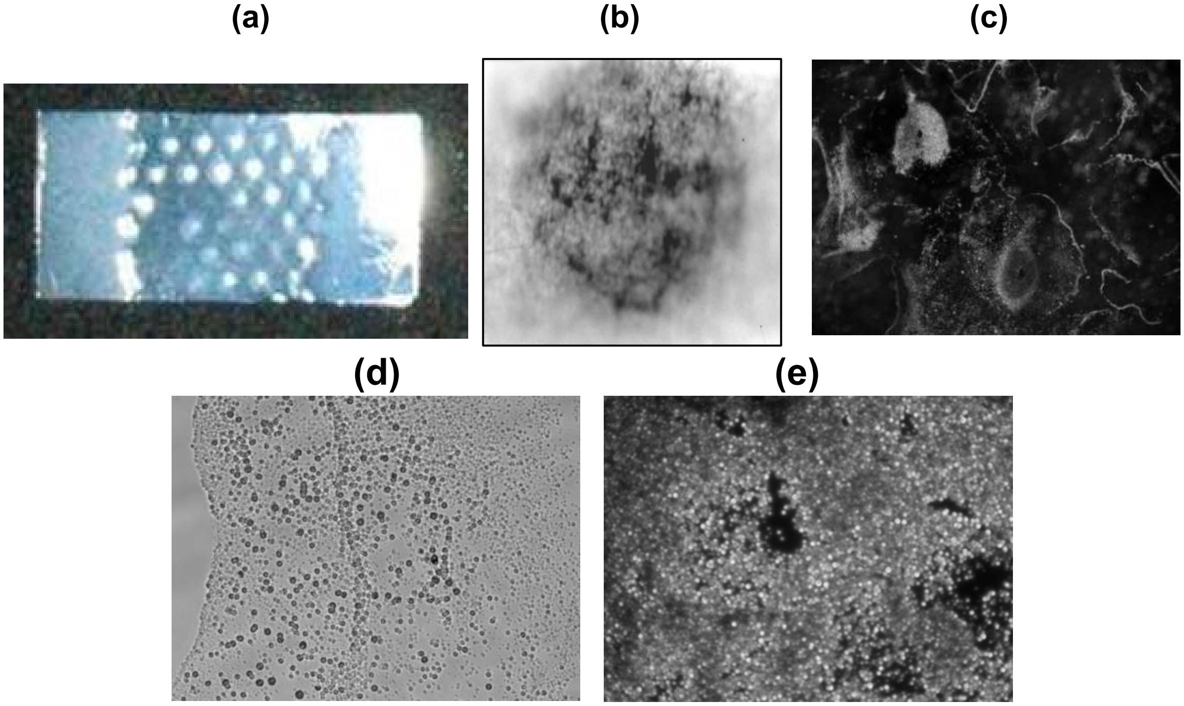

Figure 3.2-2. CR-39 results for Pd/D co-deposition done on Ni screen cathodes. (a) Photograph of CR-39 used in an experiment performed in the absence of an external field. The impression of the Ni screen is observed. Photograph was obtained from S. Krivit, New Energy Times. (b) Fogging of photographic film after three days exposure to Pd deposited on an Ag disk cathode (thin Mylar separated the film and the cathode). Results of Pd/D co-deposited film that was subjected to an external magnetic field. Microscope images of the CR-39 detector that was in contact with the Pd film deposited on a Ni screen obtained using magnifications of (c) 20x and (d), (e) 200x.

damage observed in the CR-39 detector in the absence of an external electric/magnetic field may be due to soft X-ray emissions. To determine the effect of X-rays and γ-rays on CR-39, Cu screen was wrapped around two CR-39 detectors. One detector was placed inside an XRD and irradiated with X-rays while the other was exposed to a ^{137}Cs γ-ray source. After etching, the impression of the Cu screen was observed on the surface of both CR-39 detectors. Therefore, the damage observed for the Pd/D co-deposition experiment on Ni screen in the absence of an external field is consistent with X-ray/gamma ray damage.

Figure 3.2-2c shows a photomicrograph of a CR-39 detector obtained at 20x magnification that had been used in a Pd/D co-deposition experiment done on Ni screen in the presence of an external magnetic field. The jagged outline of the Ni screen can be seen in the image as well as cloudy areas. Higher magnification of the cloudy areas, Figures 3.2-2d and e, shows the presence of thousands of pits. The density of pits is denser where the Pd deposit is the thickest, *i.e.*, inside the eyelet of the Ni screen as shown in Figure 3.2-2e. The results obtained using a Ni screen cathode indicates that the tracks occur where the Pd is in contact with the CR-39 detector and only when either an external electric or magnetic field is applied. In contrast, when the cathode substrate was Ag, Au, or Pt wires, tracks were observed in both the presence and absence of an external field.

3.2.2 Summary of composite cathode results

In 2010, DoE Electrochemist Shanahan[37] proposed that the source of the pitting observed in the CR-39 detectors used in Pd/D co-deposition experiments was either due to O_2 attack or to damage due to shockwaves resulting from D_2/O_2 recombination. Experience has shown that once the Pd deposit is wet, recombination of the D_2 and O_2 does not occur. In these experiments, the Pd deposit was completely immersed in the solution. Consequently, it is unlikely that D_2 and O_2 recombination is occurring. However, additional experiments were conducted to rule out O_2 attack or D_2/O_2 recombination shockwaves as the source of the pitting observed in the detectors.

One experiment took advantage of what was observed for Pd/D co-deposition on different metal substrates. In this particular experiment, Pd/D co-deposition experiment was done using a composite cathode in the absence of an external electric/magnetic field.[38] A photograph of the composite electrode is shown in Figure 3.2-3a. The composite electrode was a Ni screen. As shown in Fig. 3.2-3a, half the Ni screen is bare. Metallic Au has been plated on the other half. At the end of the experiment, the detector was etched and analyzed. The results show that no tracks were obtained on the bare half of the cathode, Figure 3.2-3b. The impression of the Ni screen is observed. However, tracks were obtained on the Au-coated Ni screen, Figure 3.2-3c.

Both halves of the cathode experienced the same chemical and electrochemical environment at the same time. If Shanahan's suppositions were correct that the pitting in CR-39 is caused by either explosions due to chemical reactions or to O_2 attack or to shockwaves resulting from D_2/O_2 recombination, those reactions would have occurred on both the bare Ni and Au-coated Ni halves of the cathode and both halves would have shown pitting of the CR-39 detector. This was not observed. While no tracks were observed on the bare Ni half of the composite cathode, tracks were seen on the Ni/Au half of the cathode.

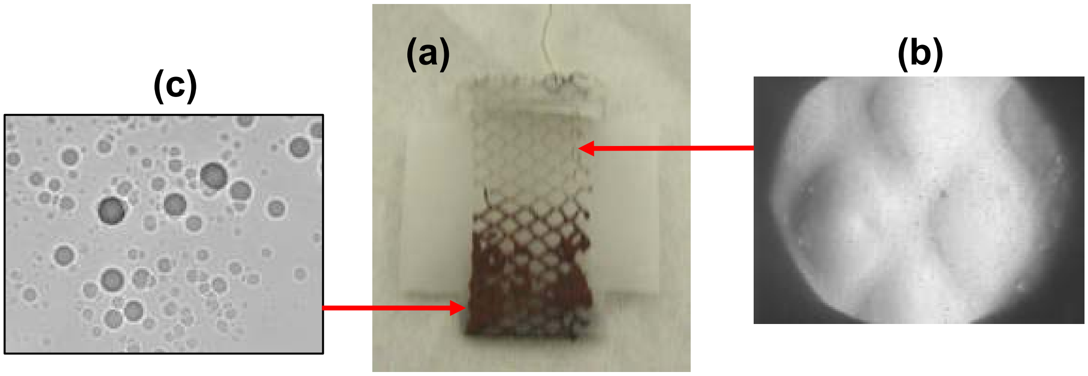

Figure 3.2-3 CR-39 results for Pd/D co-deposition done on a composite cathode. (a) Photograph of the composite electrode used in a Pd/D co-deposition experiment done in the absence of an external electric/magnetic field. The top half of the cathode is bare Ni screen, the bottom half is Au-plated Ni screen. (b) Photomicrograph of CR-39 in contact with the bare Ni half, 20x magnification. The impression of the Ni screen is observed. (c) Photomicrograph of CR-39 in contact with the Au-coated Ni half, 1000x magnification. Tracks are observed.

3.2.3 Summary of two-chamber cell results

Additional experiments were done using two chamber cells, shown schematically in Figure 3.2-4. These cells separated the anode and cathode chambers, thereby impeding the mixing of D_2 and Cl_2 / O_2 gases generated at the cathode and anode, respectively. The Cl_2 gas evolution only occurs during the plating phase of the co-deposition process. Tracks were observed on both the front and back surfaces of the CR-39 detectors used in these Pd/D co-deposition experiments. Representative photomicrographs of these front and back side tracks are shown in Figures 3.2-5a and b, respectively. The front tracks corresponded to the placement of the cathode wires. Because the anode and cathode are in separate compartments, the tracks are not due to either chlorine or oxygen attack. Furthermore, impeding the mixing of the D_2/O_2 gases prevents recombination from occurring on the Pd deposit. Since the CR-39 detectors used in these experiments are 1 mm thick, it is difficult to explain how a shockwave from a mini-explosion occurring on the front surface of the detector, as proposed by Shanahan, can propagate itself to cause pitting on the back surface without obliterating the detector. In addition triple tracks, such as the one shown in Figure 3.2-5c, have been observed in these experiments. This triple track is similar to the DT neutron-generated triple track shown in Figure 3.2-5d. The significance of triple tracks will be discussed *vide infra*. The results of both the two-chamber cell experiments and composite electrode experiment show that the pitting in the CR-39 detector is not due to either Cl_2 / O_2 attack or to D_2/O_2 recombination.

3.2.4 Comparison of Pd/D co-deposition tracks and ~1 MeV alpha tracks

Another critique of Pd/D co-deposition generated tracks is that the tracks are too large to be due to ~1 MeV alpha particles, that the majority of the tracks are circular in shape and not elliptical, and that the tracks are too shallow to be nuclear generated tracks.[39,40] In their critiques, the authors are not taking into account the effect water has on the energies of the charged particles. Figure 3.2-6a describes the processes involved when an alpha particle impacts a CR-39 detector used in a Pd/D co-deposition experiment.[41,42] An SEM of the Pd deposit is shown in Figure 3.2-6a. The deposit has a cauliflower-like morphology that traps pockets of water. As shown in the schematic in Figure 3.2-6a, after birth, the particles have to pass through the Pd

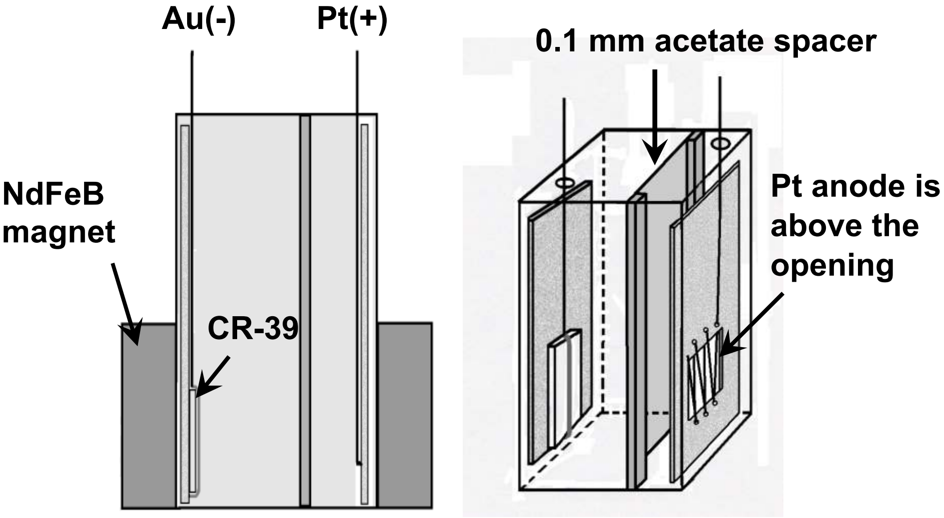

Figure 3.2-4. Schematics of the two chamber cell used to separate the anode and cathode.

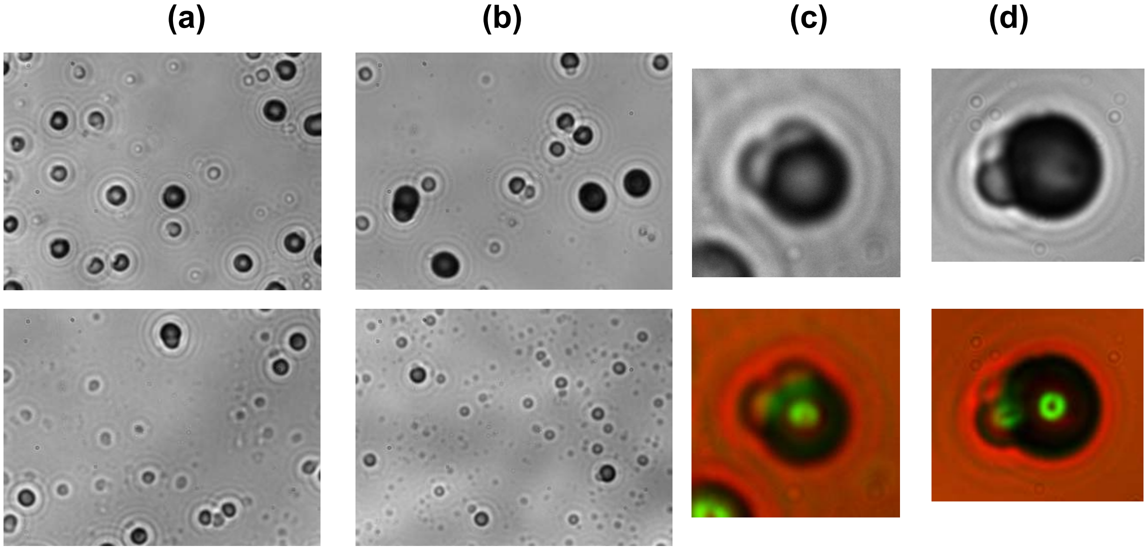

Figure 3.2-5. Tracks observed in CR-39 detectors used in Pd/D codepostion experiments with two chamber cells. (a) Tracks observed on the front surface. (b) Tracks observed on the back surface. (c) A Pd/D co-deposition generated triple track. (d) A DT neutron-generated triple track. In (c) and (d), the top images were obtained by focusing the microscope optics on the surface of the detectors and the bottom images overlay two images taken at different focusing depths (surface and the bottom of the pits).

lattice and the water layer before impinging the detector. Figure 3.2-6b shows LET curves calculated for protons, tritons, helium-3, and alpha particles in palladium and in water. These LET curves are used to determine the magnitude of the effect of Pd and water on the energies of the charged particles. The LET curve for Pd indicates that, in order for particles to be detected by a CR-detector, the particles need to originate near the surface of the Pd. Particles formed deeper inside the deposit will simply not have enough energy to exit the lattice and travel through the deposit and water layer to reach the CR-39 detector.

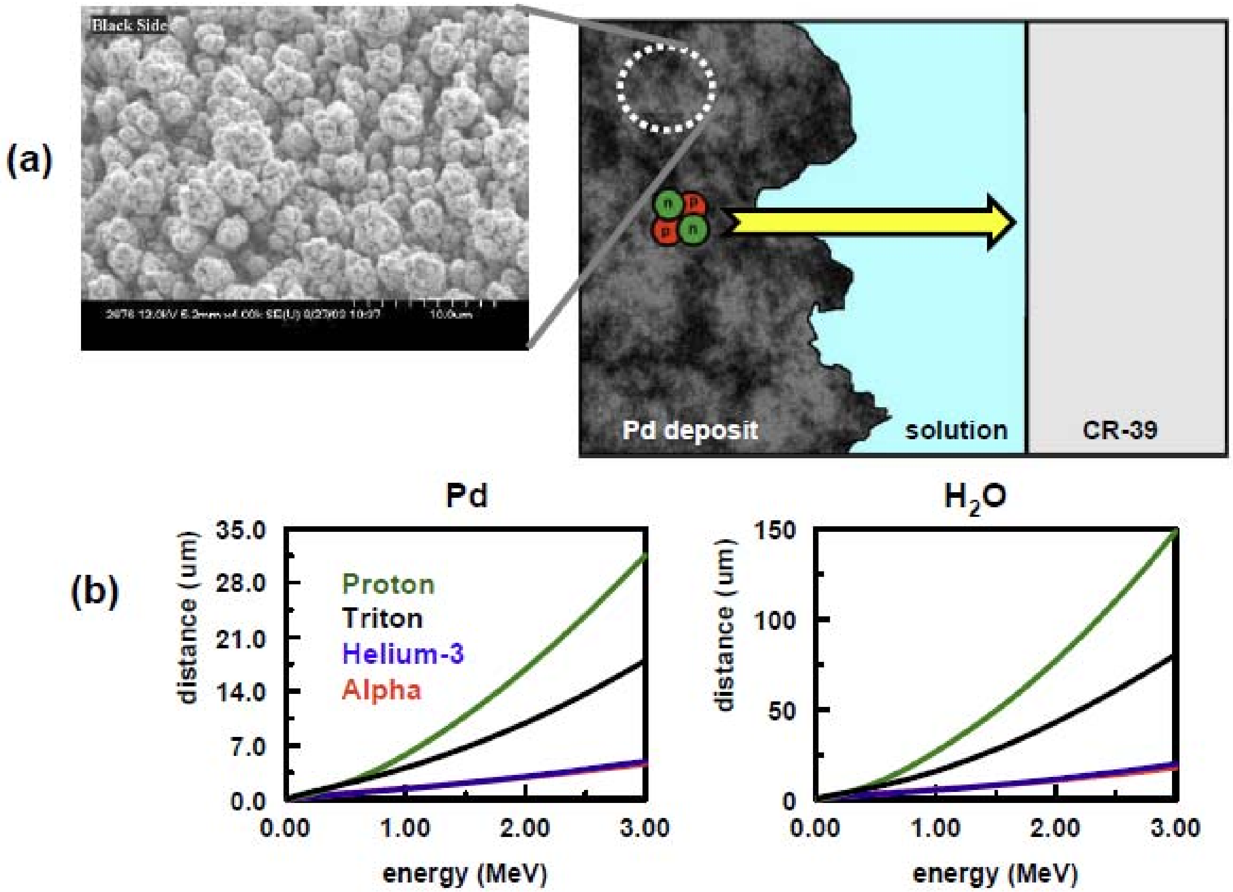

Figure 3.2-6 (a) Schematic describing the layers a charged particle has to negotiate before it impacts the CR-39 detector. An SEM of the Pd deposit formed as the result of the co-deposition process is shown. (b) LET curves calculated for charged particles traversing through palladium and water.

To simulate the effect of water on the transmission of charged particles, layers of Mylar were placed between a CR-39 detector and an ^{241}Am alpha source. Figure 3.2-7 shows a side-by-side comparison of Pd/D co-deposition tracks with ~1 MeV alpha tracks formed by placing 24 µm of Mylar between an ^{241}Am alpha source and a CR-39 detector. The Pd/D and ~1 MeV alpha tracks are indistinguishable. One of the main criticisms raised about the tracks observed in CR-39 detectors used in Pd/D co-deposition experiments is the scarcity of elliptical tracks. As shown in Figure 3.2-7a, the observed tracks are primarily circular in shape. Likewise the ~1 MeV alpha tracks are primarily circular in shape, Figure 3.2-7b. The results in Figure 3.2-7 indicate that only charged particles with trajectories normal to the surface have sufficient energy to get through the water layer, in the case of Pd/D co-deposition, and Mylar, in the case of the ^{241}Am alpha source, to impact the detector. Charged particles traveling at oblique angles are deflected and do not reach the detector.

SEM images of tracks obtained by placing 18 and 24 µm of Mylar between an ^{241}Am alpha source and a CR-39 detector are shown in Figure 3.2-8. The energy of the alphas impinging the CR-39 detector are ~1-2 MeV. While photomicrographs obtained using an optical microscope are two dimensional, images obtained using a SEM exhibit a three dimensional appearance. The

SEM images shows that the tracks due to 1-2 MeV are shallow and have rounded bottoms. The SEMs also indicate that the tracks created by these low energy charged particles have debris inside them. As the energetic particle traverses through the plastic, it creates an ionization trail that scissions CH_2, C-O-C, and CH bonds along its path. Treatment with an etching agent removes the fragments created by the scissioning of the chemical bonds. The higher the particle energy, the greater the degree of damage to the plastic. The debris observed inside the tracks of the SEM images is probably due to undamaged plastic. Similar results were reported by Składnik-Sadowska *et al.*[43] Using an optical microscope, magnifications > 1000x, and Image-Pro Plus software, Składnik-Sadowska *et al.* were able to generate three-dimensional track images of the deuteron tracks. The resultant 200 keV deuteron track images, both optical and three-dimensional, were analogous to the SEM images obtained for the 1-2 MeV alpha tracks shown in Figure 3.2-8.

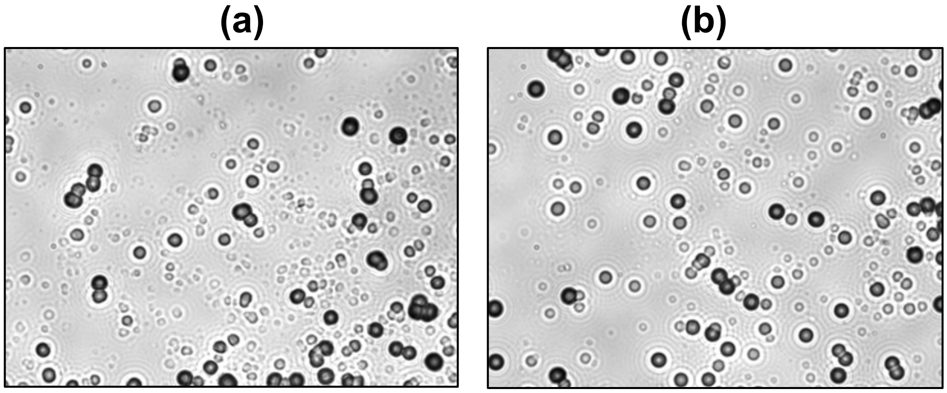

Figure 3.2-7. Photomicrographs obtained at 500x magnification for (a) Pd/D co-deposition tracks and (b) ~1 MeV alpha tracks

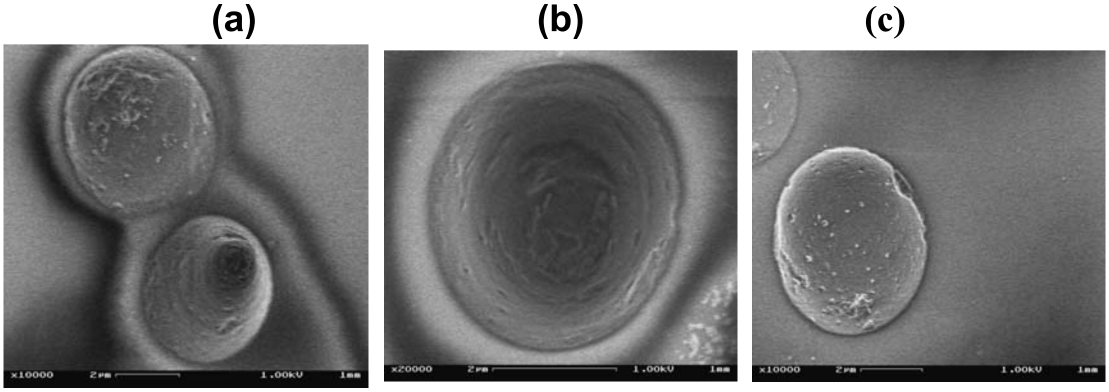

Figure 3.2-8. SEM micrographs of alpha particle tracks obtained by placing (a), (b) 18 µm and (c) 24 µm thick Mylar films between the CR-39 detectors and the ^{241}Am source.

Figure 3.2-9 shows optical and SEM images of tracks obtained as the result of a Pd/D co-deposition experiment conducted on an Au wire cathode. The observed tracks are mostly circular in shape, *i.e.*, the three tracks circled in the lower half of Figure 3.2-9a. The end points of these tracks, Figure 3.2-9b, are in the center indicating that the particles responsible for creating these tracks entered nearly perpendicular to the surface of the detector. In the upper half of Figure 3.2-9a, two elliptical tracks are circled. Focusing inside the tracks, Figure 3.2-9b, it can be seen that there are streaks instead of a distinct bright spots. The elliptical shape of the tracks as well as the streak seen when focusing deeper inside the track indicate that the particles creating these tracks entered the detector at oblique angles.

SEMs micrographs of the areas circled in Figure 3.2-9a were obtained. Figure 3.2-9c shows the three circular tracks at a magnification of 5000x. The three tracks are shallow with rounded bottoms. They look very similar to the SEM images of the 1-2 MeV tracks shown in Figure 3.2-8. Figure 3.2-9d shows an SEM image of the left-hand elliptical track, circled in Figure 3.2-9a, obtained at a magnification of 10000x. It can be seen that one end of the track is larger than the other end. This is the expected behavior for a particle that enters the detector at an oblique angle. The SEM images of the circular and elliptical tracks have debris inside of them similar to that seen in the SEM images obtained for the 1-2 MeV alphas, Figure 3.2-8.

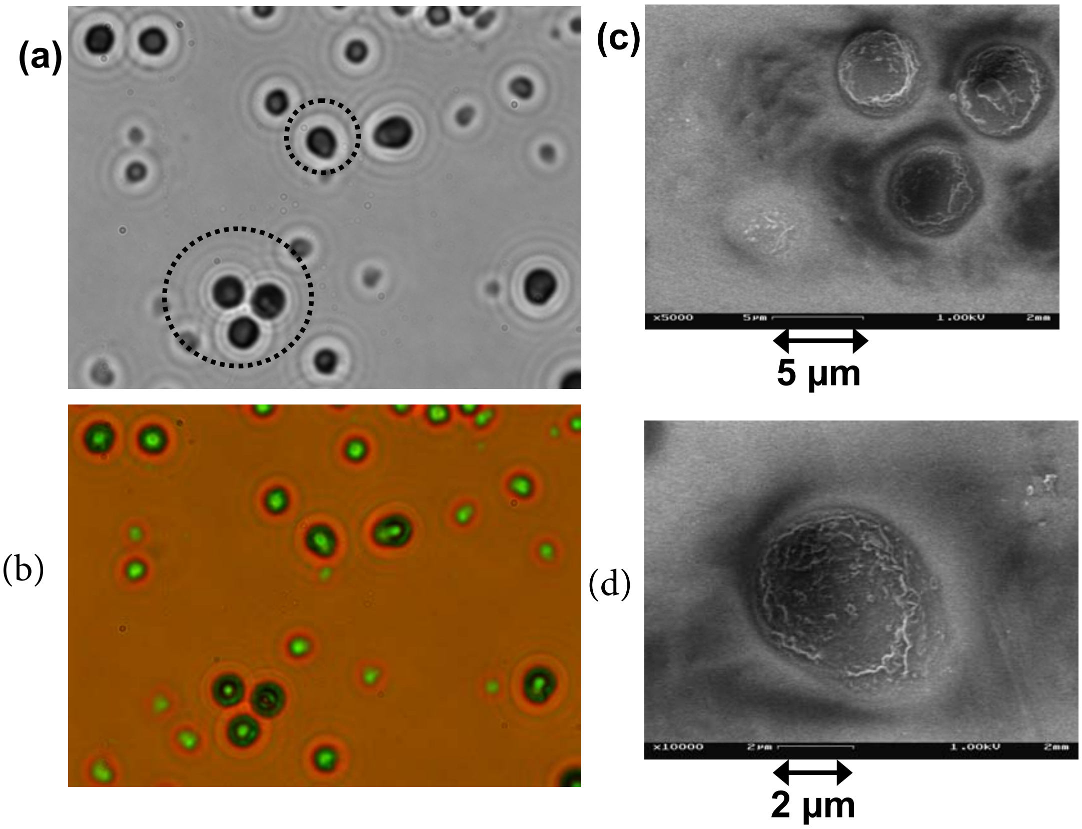

Figure 3.2-9. Optical micrographs obtained for tracks generated as the result of Pd/D co-deposition. In this experiment, the cathode was a Au wire. Magnification used to obtain the images was 1000x. (a) Image taken by focusing the optics on the surface of the detector. (b) Image is the result of overlaying two images taken with the optics focused on the surface and the bottom of the tracks. SEMs were taken of the circled areas in (a). The SEM images were taken at magnifications of (c) 5000x and (d) 10,000x.

3.3 Comparison of DT and Pd/D Co-deposition Generated Triple Tracks in CR-39 Detectors

3.3.1 Neutron interactions with CR-39 detectors

Besides charged particles, CR-39 detectors have been used in the inertial confinement fusion (ICF) community to measure neutron yields from DD and DT implosions.[44] In order to detect neutrons with CR-39, the neutron must either scatter or undergo a nuclear reaction with the proton, carbon, or oxygen atoms comprising the detector to form a moving charged particle. It is the track of this neutron-generated charged particle that is revealed upon etching. Figure 3.3-1a summarizes the possible interactions of DD neutrons (2.45 MeV) and DT neutrons (14.1 MeV) with CR-39. In the interaction shown in case 1, the DD and DT neutrons can scatter elastically, producing recoil protons, carbons, or oxygen nuclei in the forward direction. But, DT neutrons can also undergo two inelastic (n,p and n,α) reactions with carbon or oxygen, case 2 and case 3, respectively in Fig. 3.3-1a. These inelastic reactions result in charged particles that can produce tracks on the front and/or the back side of the CR-39 detector. As indicated in Fig. 3.3-1a, knock-on tracks resulting from fast neutrons should appear uniformly throughout the CR-39 detector which would be revealed by sequential etching of the detectors.

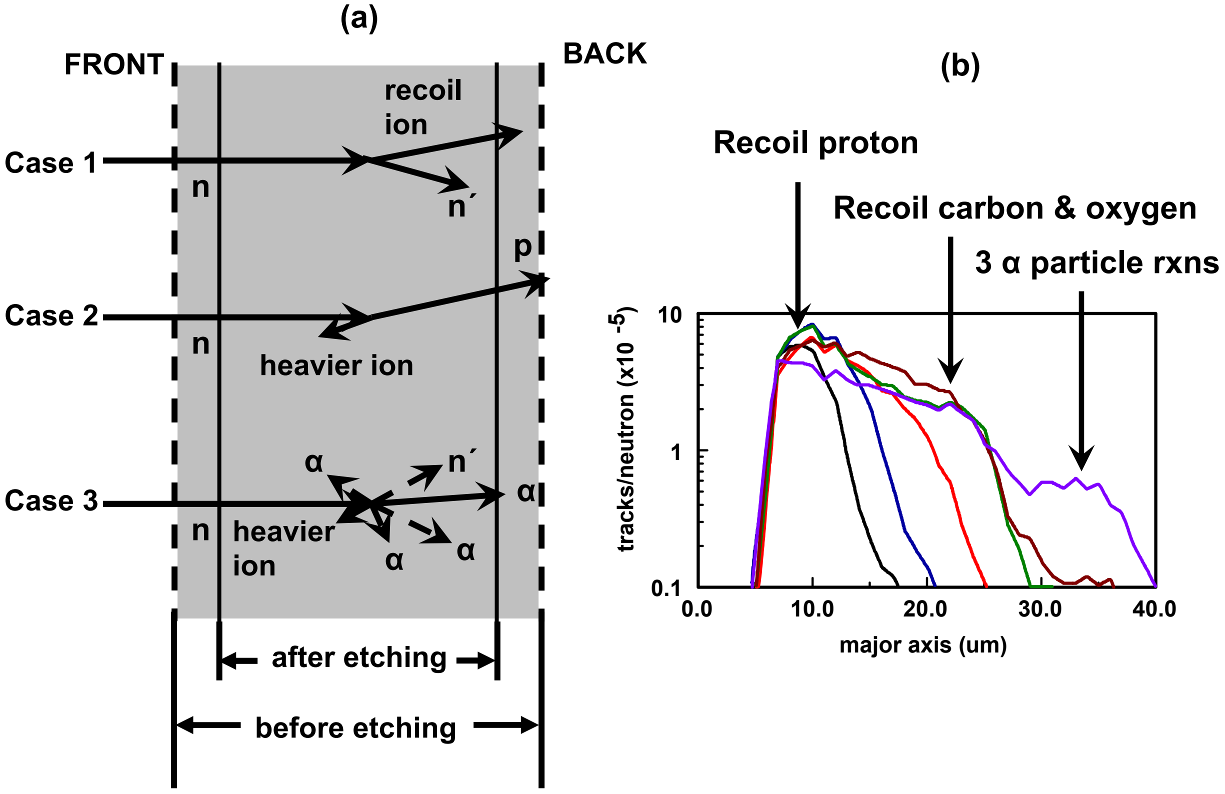

Fig. 3.3-1 (a) Schematic drawing of the CR-39 track detector and the neutron interaction processes that can take place inside the plastic.[44] The drawing is not to scale. Case 1 summarizes the DD neutrons interaction with CR-39. Cases 1–3 describe the DT neutron interactions with CR-39. (b) Track size distribution for CR-39 detectors that have been exposed to monoenergetic neutrons.[25] The energies of the neutrons, in MeV, are, from left to right, 0.114 MeV, 0.25 MeV, 0.565 MeV, 1.2 MeV, 8.0 MeV, and 14.8 MeV

Phillips *et al.*[25] have shown that neutron spectrometry can be done using CR-39. At low neutron energies (0.144 MeV), only recoil protons are seen and are observed to occur as a peak at ~ 10 µm, Figure 3.3-1b. As the neutron energy increases, a broadening of the proton recoil peak at ~ 10 µm is observed. At 1.2 MeV neutron energy, a second peak is visible at ~ 25 µm. This second peak is attributed to recoil carbon and oxygen atoms. For neutron energies between 1.2 and 8.0 MeV, the size distributions of tracks observed in the CR-39 detectors are roughly similar. As discussed *vide supra*, Roussetski and Lipson[27] have developed a sequential etching method which allows them to differentiate between 1.2 and 8.0 MeV recoil protons. In the CR-39 detector exposed to 14.8 MeV neutrons, a decrease in the proton recoil at ~ 10 µm is observed, Figure 3.3-1b, and a peak is observed at ~35 µm which is attributed to the carbon break-up reaction. The signature of this reaction in CR-39 detectors is the triple track, in which three alpha particles break away from a center point.

3.3.2 DT neutron generated *vs.* Pd/D co-deposition generated triple tracks

Figure 3.3-2a shows a photomicrograph, at 200x magnification, of a CR-39 detector that had been used in a Pd/D co-deposition experiment. This region showed a relatively low density of tracks. All the tracks are solitary except for the one that is circled. This track is shown at 1000x magnification in Figure 3.3-2b. The top image was taken with the microscope optics focused on the surface of the detector and the bottom image is an overlay of two images obtained at different focusing depths (surface and the bottom of the tracks). It can be seen that the two lobes of the track are breaking away from a single center point. This contrasts with what is observed for overlapping tracks. When the microscope optics are focused inside overlapping tracks, each track in the cluster shows a separate, distinct, bright spot.[16,45]

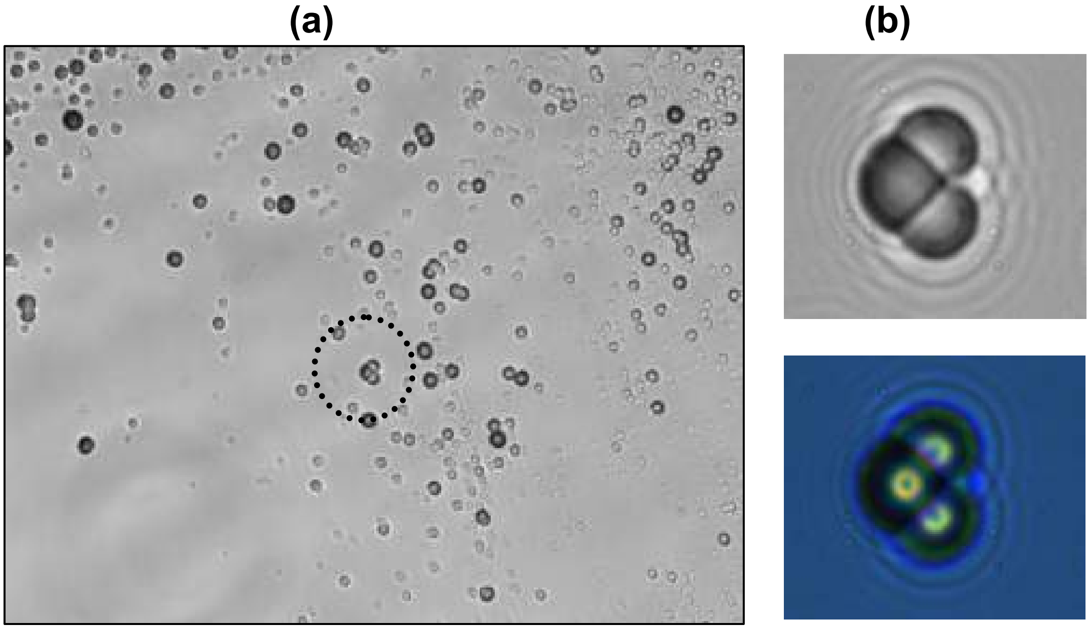

Figure 3.3-2. (a) Image of a triple track (circled) among the solitary tracks (magnification 200x) in a CR-39 detector used in Pd/D co-deposition experiment. (b) Image of the triple track shown in (a) at magnification 1000x. The top image was obtained by focusing the optics on the surface of the CR-39 detector while the bottom image is an overlay of two images taken at two different focal lengths (surface and bottom of the pits).

CR-39 detectors were then exposed to DT neutrons. Figure 3.3-3 shows examples of triple tracks that look very similar to the one seen in Figure 3.3-2b. These two examples show two alpha particle tracks breaking away from a center point. The subtle differences between the triple tracks shown in Figures 3.3-2b and 3.3-3 has to do with the fact that the $^{12}\mathrm{C}(\mathrm{n},\mathrm{n}')3\alpha$ carbon breakup reaction is anisotropic. While the carbon break up reaction that yielded the triple tracks shown in Figure 3.3-2b and 3.3-3b occurred more or less parallel to the plane of the detector, the one that resulted in the triple track in Figure 3.3-3a occurred at ~45° angle inside the plastic.

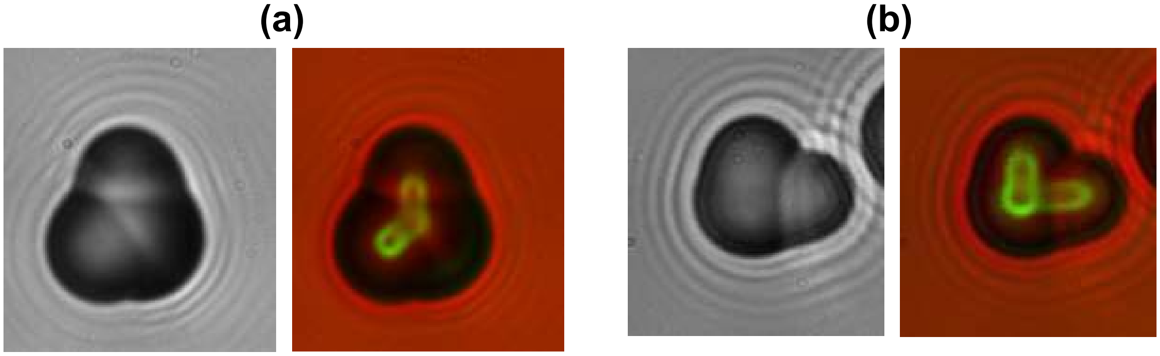

Figure 3.3-3. (a) and (b) Photomicrographs of DT neutron generated triple tracks in CR-39 detectors that are similar to the Pd/D co-deposition generated triple track shown in Figure 3.3-2. For both (a) and (b), the left hand images were obtained by focusing the optics on the surface of the CR-39 detector while the right hand images are overlays of two images taken at two different focal lengths (surface and bottom of the pits).

Figures 3.3-4 and 3.3-5 show other examples of symmetric and asymmetric triple tracks, respectively, that have been observed in CR-39 detectors used in Pd/D co-deposition experiments, along with their analogous DT neutron generated triple tracks. The examples of Pd/D and DT neutron generated tracks shown in Figure 3.3-4 do not have the exact same shape. For the tracks shown in Figures 3.3-4a and d, the lobes making up the triple track do not all have the same size. Clearly one lobe is bigger than the other two, which are of similar size. The n + $^{12}\mathrm{C}$ reaction can proceed to the four-body final state through one or more of the following reaction mechanisms:[46]

$$\mathrm{n} + {}^{12}\mathrm{C} \rightarrow \mathrm{n}' + {}^{12}\mathrm{C}(\alpha)\,{}^{8}\mathrm{Be}(2\alpha) \tag{1}$$

$$\mathrm{n} + {}^{12}\mathrm{C} \rightarrow \alpha + {}^{9}\mathrm{Be}(\mathrm{n}')\,{}^{8}\mathrm{Be}(2\alpha) \tag{2}$$

$$\mathrm{n} + {}^{12}\mathrm{C} \rightarrow \alpha + {}^{9}\mathrm{Be}(\alpha')\,{}^{5}\mathrm{He}(\mathrm{n}', \alpha) \tag{3}$$

$$\mathrm{n} + {}^{12}\mathrm{C} \rightarrow {}^{8}\mathrm{Be}(2\alpha) + {}^{5}\mathrm{He}(\mathrm{n}', \alpha) \tag{4}$$

$$\mathrm{n} + {}^{12}\mathrm{C} \rightarrow \mathrm{n}' + \alpha + \alpha + \alpha \tag{5}$$

The observed relative sizes and shapes of the lobes comprising the triple tracks in Figure 3.3-4 may be reflective of these different processes. For example, the $^{9}\mathrm{Be}$ recoil has a higher ionization rate and, since the cone angle decreases with increasing ionization rate, has a smaller cone angle.[48]

Examples of asymmetric, two-pronged, tracks for the carbon breakup reaction are shown in Figure 3.3-5. Such tracks could be due to the fact that the third prong is below the plane of the detector and is, therefore, not visible. It could also be due to energetics. One of the three alphas particles may not have sufficient energy to make an etchable track and, consequently, cannot be observed.[47] For CR-39, they could also be due to reactions of the type $^{12}\mathrm{C}(n, \alpha)^{9}\mathrm{Be}$ or

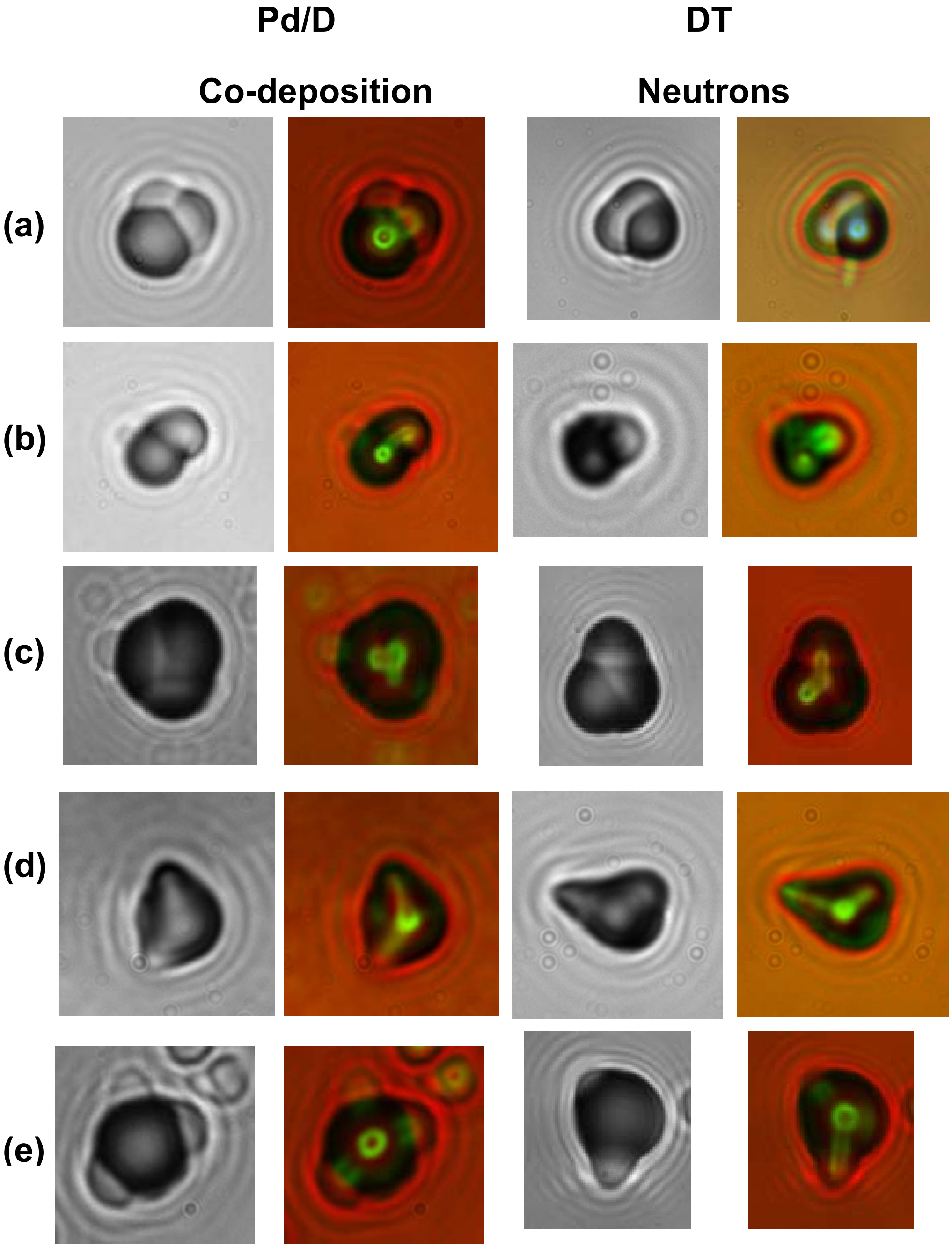

Figure 3.3-4. Comparison of symmetric Pd/D co-deposition generated triple tracks and DT neutron generated triple tracks. The the left hand images were obtained by focusing the optics on the surface of the CR-39 detector while the right hand images are overlays of two images taken at two different focal lengths (surface and bottom of the pits).

$^{16}O(n, \alpha)^{13}C$.[48] The track caused by these reactions typically has one prong with a bigger cone angle than the other which are attributed to the alpha particle and the recoiling residual nucleus, respectively.

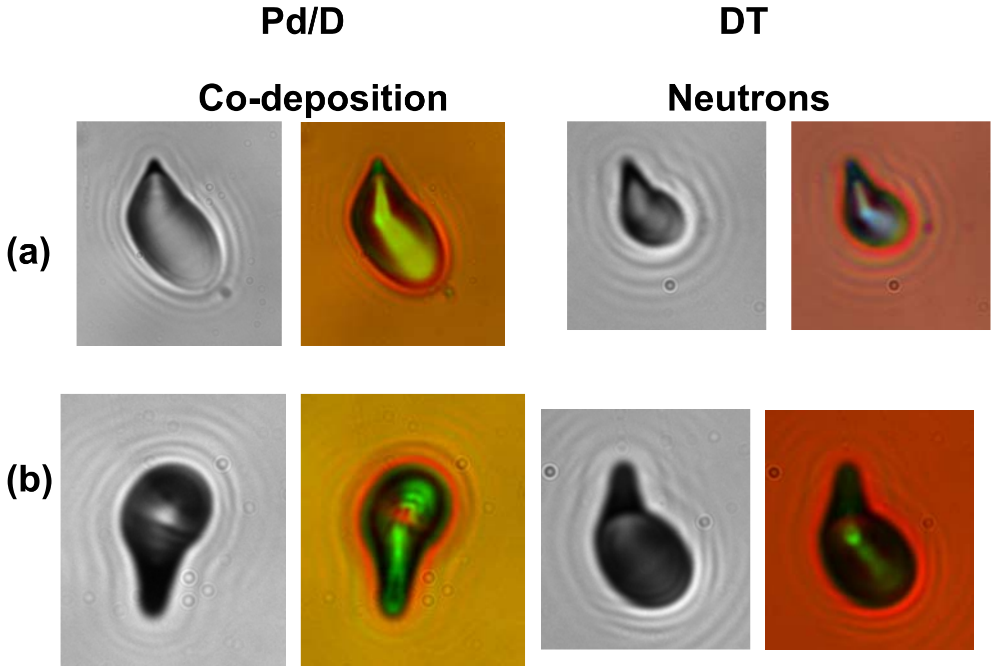

Figure 3.3-5. Comparison of asymmetric Pd/D co-deposition generated triple tracks and DT neutron generated triple tracks. The the left hand images were obtained by focusing the optics on the surface of the CR-39 detector while the right hand images are overlays of two images taken at two different focal lengths (surface and bottom of the pits).

3.3.3 Optical and SEM analysis of triple tracks

Besides optical imaging, the triple tracks observed in CR-39 have also been subjected to SEM analysis. Figure 3.3-6a shows optical images of a symmetric triple track observed in a Pd/D co-deposition experiment. Optical images of a DT neutron-generated triple track are shown in Figures 3.3-6b and c. The Pd/D generated and the DT-neutron generated triple tracks are indistinguishable. In Figures 3.3-6a, b and c, the top images were taken with the microscope optics focused on the surface of the detector and the bottom images are an overlay of two images taken with the optics on the surface and the bottom of the pits. The large lobes of the triple tracks show a bright streak in the center, bottom images of 3.3-6a, b and c. This indicates that this lobe is shallow and rounded. The SEM image of the Pd/D co-deposition triple track, Figure 3.3-6d, supports this conclusion. Besides the large lobe, the Pd/D co-deposition generated triple track has two smaller lobes on the left-hand side, Figure 3.3-6a. The bottom overlay image shows no bright centers or streaks in the two smaller lobes of this triple track. This suggests that there are either steep track walls or that the track has a conical shape. As shown in the SEM image, Figure 3.3-6d, one of the smaller lobes has a conical shape. These results show that optical and SEM imaging of tracks compliment one another.

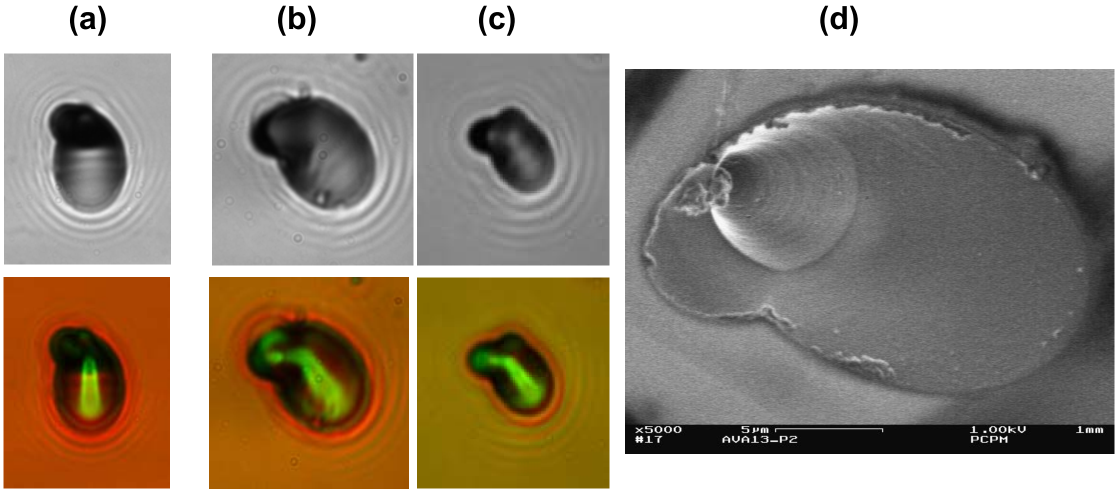

Figure 3.3-6. (a) Optical microphotographs of a Pd/D co-deposition generated triple track obtained at 1000x magnification. (b) and (c) Optical microphotographs of analogous symmetric DT-neutron generated triple tracks obtained at 1000x magnification. In (a) -(c) the top images were taken by focusing the microscope optics on the surface of the CR-39 detector and the bottom images are overlays of two images taken at the surface of the detector and the bottom of the pits. (d) An SEM image of the same Pd/D co-deposition generated triple track shown in (a) taken at 5000x magnification.

3.3.4 Summary of blanks and control experiments

Blank detectors, not used in Pd/D co-deposition experiments, show solitary tracks. The track density is ~85 tracks cm^{-2}. No triple tracks were observed in these blank detectors indicating that the triple tracks observed in the Pd/D co-deposition experiments were not the result of DT neutron irradiation of the detectors or to cosmic ray spallation neutrons. Nakamura *et al.*[49] have measured the energy spectrum of cosmic ray-induced spallation neutrons and found it consists of three peaks: thermal, 1 MeV evaporation and a cascade peak at 100 MeV. The evaporation peak overlaps the DD fusion 2.45MeV neutron energy. However, the 12−17 MeV neutron energies, overlapping DT Fusion neutrons with a nominal 14.1 MeV energy, occur an order of magnitude less frequently than either evaporation or cascade neutrons. The total measured background spallation neutron flux was 7.5×10^{-3} n cm^{-2} s^{-1}, with $<10^{-4}$ n cm^{-2} s^{-1} in the DT fusion neutron energy range. This, coupled with the CR-39 relative neutron detection inefficiency, $<10^{-6}$ for triple tracks,[25] accounts for the complete absence of triple tracks in the background.

The $CuCl_2$ control experiment discussed in Section 3.1 indicates that the triple tracks observed in the CR-39 detectors used in the Pd/D co-deposition experiments are not due to either chemical or mechanical damage nor are they due to artifacts in the plastic. As discussed in section 3.1, for both the Pd and Cu electroplating, similar chemical and electrochemical reactions are occurring on the surfaces of the electrodes, *i.e.* a metal plates out in the presence of evolving deuterium gas at the cathode while oxygen and chlorine gas evolution occurs at the anode. Both Cu and Pd deposits exhibit cauliflower-like morphologies. The only significant difference between the Cu and Pd electroplating experiments is that metallic Pd absorbs deuterium and Cu does not. Because similar chemical and electrochemical reactions are occurring on like morphologies, it is expected that the electrical double layers for the two systems will be comparable. Upon etching, no triple tracks were observed in the CR-39 detector used in the Cu electroplating control. The number of solitary tracks was comparable to what was observed in blank detectors.

3.3.5 Quadruple tracks

Figure 3.3-7 shows images of the only two quadruple tracks that were observed in the CR-39 detectors that had been exposed to DT neutrons. Quadruple tracks, where four alpha particles are breaking away from a center point, are signatures of the oxygen shattering reaction:[50]

$$^{16}O + n \rightarrow 4\alpha + n' \qquad (6)$$

The neutron threshold energy for this reaction to occur is 15.44 MeV. No such tracks have been observed in the CR-39 detectors used in Pd/D co-deposition experiments. These observations indicate that the energetic neutrons formed during Pd/D co-deposition fall in an energy range between 9.6 and 15.44 MeV.

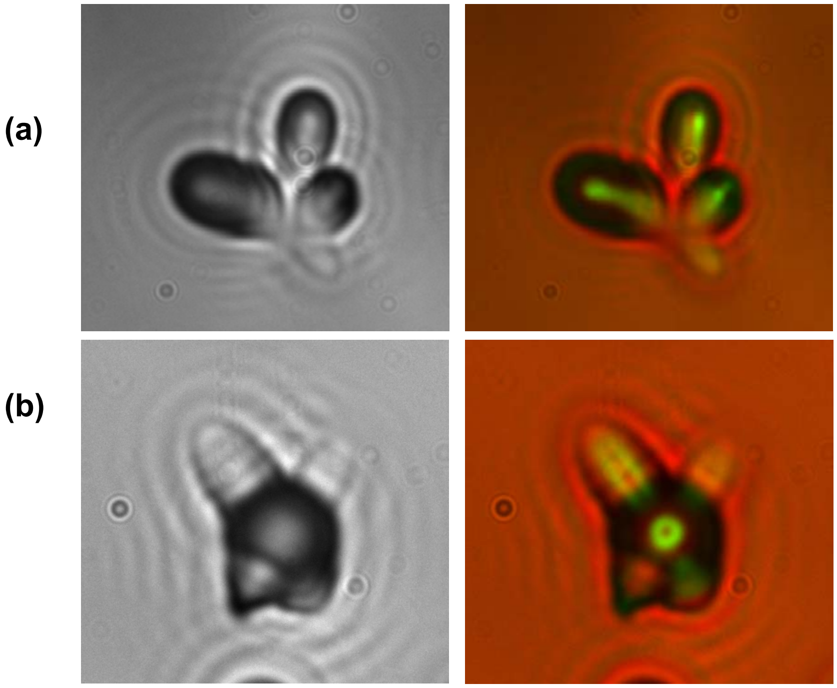

Figure 3.3-7 (a) and (b). Photomicrographs of quadruple tracks observed in CR-39 detectors that had been exposed to DT neutrons. Magnification is 1000x. The left hand images were obtained by focusing the optics on the surface of the CR-39 detector while the right hand images are overlays of two images taken at two different focal lengths (surface and bottom of the pits).

3.3.6 Discussion of the origins of triple tracks in Pd/D co-deposition experiments

The triple tracks observed in the CR-39 detectors used in the Pd/D co-deposition experiments indicate that neutrons with energies between 9.6 and 15.44 MeV are formed. What are the origins of these neutrons? The primary, (7) and (8), and secondary, (9) and (10) plasma fusion reactions are:[44]

$$\mathrm{D+D} \rightarrow \mathrm{T}\ (1.01\ \mathrm{MeV}) + \mathrm{p}\ (3.02\ \mathrm{MeV}) \tag{7}$$
$$\mathrm{D+D} \rightarrow \mathrm{n}\ (3.45\ \mathrm{MeV}) + {}^{3}\mathrm{He}\ (0.82\ \mathrm{MeV}) \tag{8}$$
$$\mathrm{D+T}\ (\leq 1.01\ \mathrm{MeV}) \rightarrow \alpha\ (6.7-1.4\ \mathrm{MeV}) + \mathrm{n}\ (11.9-17.2\ \mathrm{MeV}) \tag{9}$$
$$\mathrm{D}+{}^{3}\mathrm{He}\ (\leq 0.82\ \mathrm{MeV}) \rightarrow \alpha\ (6.6-1.7\ \mathrm{MeV}) + \mathrm{p}\ (12.6-17.5\ \mathrm{MeV}). \tag{10}$$

LENR researchers have seen evidence of these neutrons and charged particles. As discussed in section 3.1, Lipson and Roussetski saw 3.03 MeV proton tracks and proton recoils due to 2.3-2.5 MeV neutrons in CR-39 detectors used in Pd/D co-deposition. Zhou identified 9.75 and 11.5-12 MeV protons as well as 2-15 MeV alpha particles. In experiments involving Au/Pd/PdO heterostructures, Lipson *et al.*[51] saw evidence of protons, tritons, and ^{3}He particles in CR-39 detectors due to DD reactions. Using a liquid scintillator, they detected 2.45 MeV neutrons. Using a silicon barrier detector and Pd foils and films, Taniguchi *et al.*[52] detected 3.03 MeV protons. In 2000, Roussetski[53] was the first to report on seeing triple tracks in CR-39 detectors used in his experiments with Au/Pd/PdO heterostructures. He indicated that "the presence of three α-particle tracks outgoing from a single point allows us to separate these (carbon break-up) reactions from other neutron interactions with CR-39 detectors". From his analysis of the CR-39 detectors used in the Au/Pd/PdO heterostructures experiments, Roussetski concluded that the number of tritons needed to account for the observed triple tracks in the detectors was greater than the yield of tritons from DD reactions. He speculated that there was an unknown nuclear reaction that created the high-energy neutrons and suggested that the process may be the 3D and 4D fusion reactions predicted by Takahashi.[54]

Mosier-Boss *et al.*[45] offered an alternative explanation for Roussetski's observations. They suggested that the metal lattice creates conditions that favor the DT reaction. If this is the case, tritons will be consumed shortly after birth to create 11.9−17.2 MeV neutrons. This would explain Roussetski's observation that there are more triple tracks than can be accounted for by the number of tritons as only those tritons not consumed in the secondary reaction shown in equation (9) will be registered on the CR-39 detector. There are two conditions which must be met in order for DT reactions to occur – the triton needs to be energetic and it needs to encounter a deuterium atom. As discussed above, there is evidence of energetic tritons from the work done by Lipson *et al.*[51] and Taniguchi *et al.*[52]. With regards to the second condition, it has been shown that the deposit formed as a result of Pd/D co-deposition is fully loaded with deuterium, *i.e.*, D/Pd > 1.[4] LET calculations indicate that a 1 MeV triton will traverse through 4.12 μm of Pd. Given the high density of D inside the Pd lattice, it is highly likely that the energetic triton will encounter a D atom as it races, in any direction, through the lattice. In addition, the cross section of DT fusion is higher than that of DD fusion.[55] What may be occurring inside the Pd lattice is analogous to what is observed in accelerator experiments involving stationary targets and ion beams such as the neutron generator used to create the DT neutron tracks. The significant difference is that, in the Pd/D system, the triton beam is essentially produced *in situ.*

3.4 Pd/D Co-deposition Experiments Conducted using Uranium as a Witness Material

3.4.1 Introduction

Uranium has three naturally occurring isotopes: ^{234}U (0.0054%), ^{235}U (0.7204%), and ^{238}U (99.2742%). In 2003, Cravens and Letts[56] reported on using uranium as a chemical additive to trigger heat production in their Pd/D co-deposition experiments. In our investigations, the use of uranium as a witness material was explored to determine the energies of the neutrons produced during Pd/D co-deposition.^{235}U is fissioned by thermal and higher energy neutrons while ^{238}U is fissioned by >2 MeV neutrons. The cross section for interaction with fast neutrons is equivalent for ^{235}U and ^{238}U, on the order of < 2 barns (as compared to >500 barns for the thermal fission of ^{235}U. The nuclear diagnostics used in these experiments were HPGe for real time gamma-ray measurements, CR-39 detectors, and liquid scintillation for detection of beta, gamma, and alpha emitters in the solution and cathode upon termination of the experiment.

3.4.2 Results of real-time gamma emissions using HPGe

Figure 3.4-1a shows a photograph of one of the cells used in these experiments. Pd/D co-deposition was done on a cathode comprised of an Au wire with a 1 cm long, native U wire as a witness material. Figure 3.4-1b shows the 10% HPGe detector with an Al window inside a Pb cave. Figure 3.4-1c shows the placement of the cell and face of the HPGe detector inside the Pb cave. Figure 3.4-2 shows spectra obtained during the early stages of Pd/D co-deposition. The applied current was -0.4 mA. The HPGe detector has an Al window that cuts off at 25 keV. This cut off is indicated by the dashed line in Figure 3.4-2. At 0830, lines due to ^{235}U and the daughters of ^{238}U are observed on top of a raised baseline. Arrows indicate three broad peaks at 14, 118, and 194 keV observed on this raised baseline. With additional time, these broad peaks disappear. The 14 keV peak is not due to a gamma ray as the Al window blocks all gamma rays below 25 keV. The broadness of the peaks also indicate that they are not due to gamma rays. According to Dr. Patrick McDaniel, a nuclear engineer from Sandia National Lab, general peak broadening occurs as a result of neutron damage. It is noteworthy that these neutrons were observed to occur during the early stages of the plating phase of Pd/D co-deposition. These observations agree with the BF_3 neutron measurements done by SRI during their replication of the SSC-Pacific protocol discussed *vide supra.*

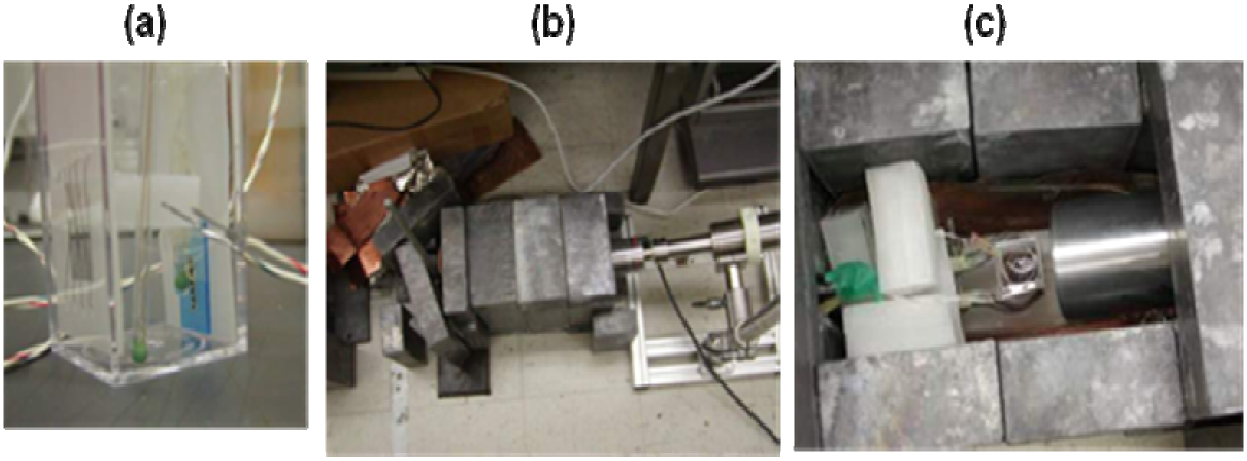

Figure 3.4-1 (a) Photograph of a cell used in a Pd/D co-deposition experiment done on a Au/U cathode. (b) Photograph of the HPGe detector inside a Pb cave. (c) Photograph of the cell inside a Pb cave for real-time gamma measurements.

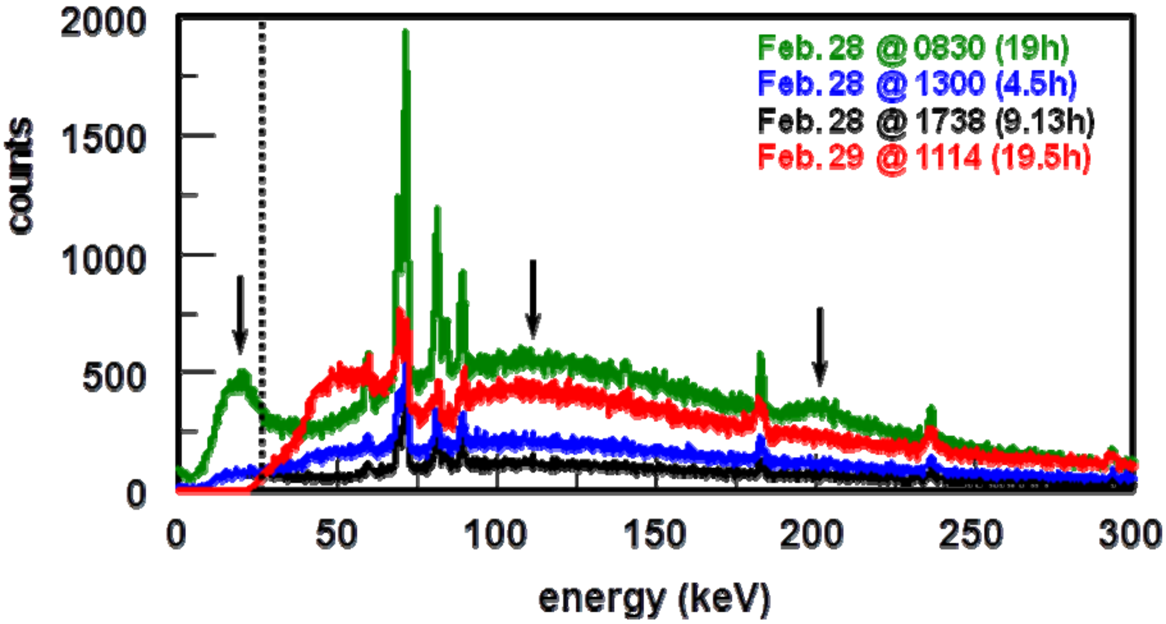

Figure 3.4-2. Gamma ray spectra (not time normalized) obtained as a function of time for a Au/U/Pd/D co-deposition experiment. Date and time spectra were obtained are indicated as well as the acquisition time (in parentheses). The dashed line at 25 keV indicates the cut off of the Al window. The arrows indicate peaks due to elastic neutron recoils with Ge.

Figure 3.4-3a show the time-normalized, baseline corrected gamma ray spectra between 55 and 95 keV. These are the same spectra as shown in Figure 3.4-2. On 2-28 at 1300, the spectral lines are similar to that observed on 2-28 at 0830. By 2-28 at 1738, the lines are less intense and appear to be broadening. On 2-29 at 1114, the peaks are clearly less intense and broadened. Figure 3.4-3b shows the ^{40}K line at 2-28 0830 and at 2-29 1114. On 2-28 at 0830, the ^{40}K line fits to a single Gaussian line. By 2-29 at 1114, the ^{40}K line has lost intensity and shows a tail on the low frequency side. This peak fits to two Gaussians, as shown in Figure 3.4-3b. The changes observed in the gamma ray lines are consistent with neutron damage to a HPGe detector.[57-59]

The observed changes in the spectra observed during February 28 are not due to gain shift. This is most noticeable comparing peaks for the background ^{40}K gamma line (1.46 MeV) in Figures 3.4-3b and 3.4-4b. In each case, the ^{40}K line is centered near channel 8380. The February 28th spectrum shows a single symmetric Gaussian peak whereas the February 29th, and in the next Figure spectra from March 6th and April 23rd , show the same, unshifted double Gaussian fit consistent with neutron damage. Since the center-of-mass of the spectra hasn't moved, there has been no gain shift. A gain shift would result is a symmetric broadening of the original Gaussian, not an asymmetric lowering of the peaks and a broadening towards lower energy. In addition, a gain shift would apply nearly equally to all peaks. The background spectra at lower energy, peaks in Figures 3.4-3a between 55 keV and 95 keV, have not shifted relative to the same peaks a month later in Figure 3.4-4a between channels 325 and 525. Furthermore, the spectra in Figure 3.4-3 were shown to engineers at Ortec, who confirmed that the HPGe detector had sustained neutron damage.

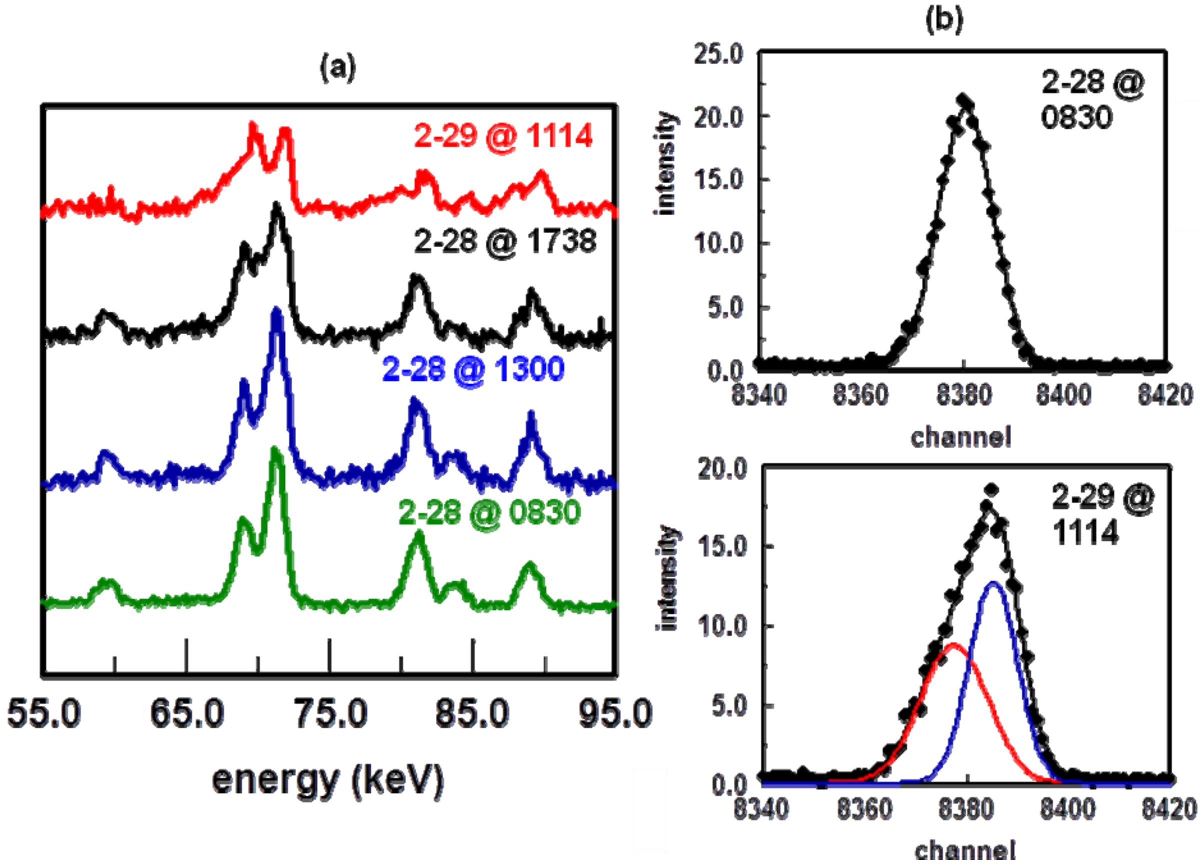

Figure 3.4-3. (a) Time normalized, baseline corrected gamma ray spectra obtained as a function of time for an Au/U/Pd/D co-deposition experiment. Date and time spectra were obtained are indicated. (b) Time normalized spectra of the K-40 line. The top spectrum was obtained at 2-28 @ 0830. The bottom spectrum was obtained on 2-29 @ 1114.

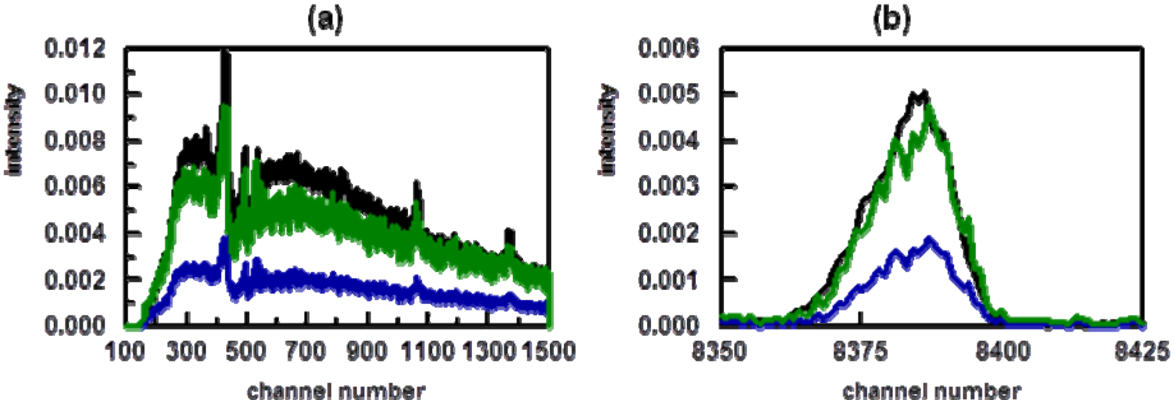

Figure 3.4-4. Time normalized spectra obtained for (a) the energy region between 25-250 keV (channels 100-1500) and (b) the K-40 line. Black refers to the spectrum obtained on March 6, blue was obtained on April 23, and green is the blue spectrum multiplied by a factor of 2.5.

The broad, asymmetric gamma ray peaks at 596 and 691.3 keV, originating from inelastic neutron scattering ((n,ń) reaction) on ^{74}Ge and ^{72}Ge, respectively, are commonly used to estimate the fast neutron flux.[60] This is true for neutrons with energies ≤ 1 MeV.[61] For neutrons with energies > 1 MeV, the peaks due to ^{74}Ge and ^{72}Ge broaden and flatten out. For neutron energies much larger than 4 MeV, it becomes difficult to separate the peaks from the background. Since the calculated average neutron energy was 4.5 MeV, no peaks were observed at 596 and 691.3 keV in the gamma ray spectra obtained on Feb. 28 and Feb. 29.

According to McDaniel, the baseline grows and the peak broadens due to crystal dislocations that create holes that trap electrons. Thus an event that happens near the outer electrode is collected very rapidly and one gets a full height peak. One that occurs near the center, is collected slowly and the shaping constants in the amplifier only allow part of it to be collected.

McDaniel took the Feb. 28 @ 0830 data in Figure 3.4-2 and noted a raised baseline out to 350 keV. He then calculated the 6.3-6.83 MeV neutron curve shown in Figure 3.4-5 after modeling the neutron eleastic scattering by Ge nuclei.

When a high energy neutron elastically scatters a germanium nucleus, it leaves an ionization trail that is proportional to the energy given to each germanium nuclei encountered. The maximum energy that can be transferred to the germanium nucleus is (1-alpha) times the energy of the neutron, where alpha is defined as [(A-1)/(A+1)] squared. For a maximum recoil energy of 350 keV and the various germanium nuclei give the energy maxima tabulated in Table 3.4-1.

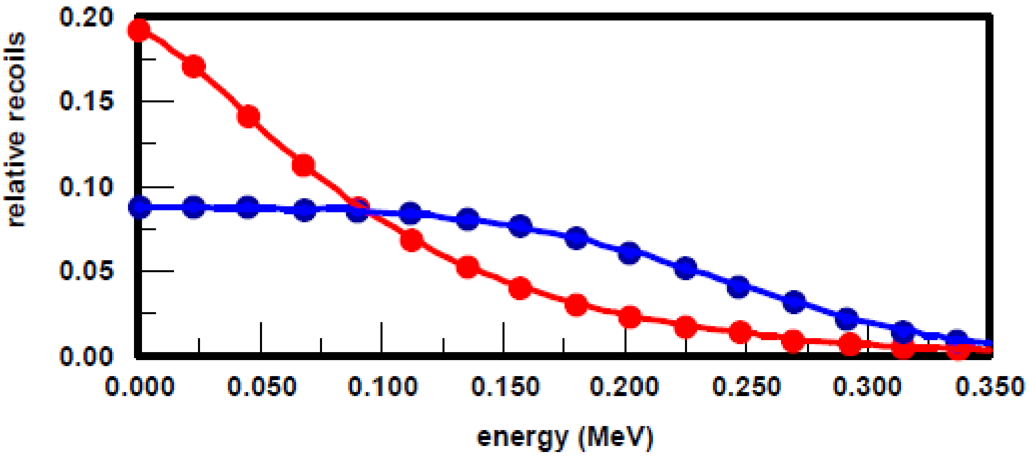

Figure 3.4-5. Fission neutron (blue) and 6.3-6.83 MeV neutron (red) curves calculated by Pat McDaniel using the Feb. 28 @ 0830 spectrum shown in Figure 3.4-2.

If the germanium were composed of a single nuclear species, for example ^{76}Ge, and it scattered isotropically in the center of mass system, there would be recoils resulting in signals from 350 keV down to 0.0 keV. However, the signal tapers down at the high end due to two effects. The first, the maximum recoil energy drops with the Ge mass number. Second, the scattering is not isotropic in the center of the mass system due to a forward scattering preference. This reduces the number of recoils at higher energies.

Table 3.4-1. Calculated energy maxima of germanium nuclei.

Ge Isotope	Alpha	$E_{neutron}$ (MeV)	Recoil Energy (keV)	Natural Abundance (%)
70	0.055545	6.30	323	20.5
72	0.054044	6.47	332	27.4
73	0.053324	6.56	336	7.8
74	0.052622	6.65	341	36.5
76	0.051273	6.83	350	7.8

McDaniel then modeled both a fission neutron spectrum and the PdD neutron spectrum in Figure 3.4-5, where he found that the PdD neutron spectrum is harder than that from fission alone. It is worth noting that the observed PdD spectrum likely consists of fission neutrons, derived from the U witness material; 2.5 MeV DD fusion neutrons; and 14.1 MeV DT fusion neutrons. The hardness of the spectrum also indicates a larger contribution of higher energy neutrons, possibly from other nuclear reactions, such as stripping.

Figure 3.4-6 shows gamma ray spectra obtained using a HPGe detector in a Compton suppressed cave. Clearly new gamma lines are present after Pd/D co-deposition. However, the species responsible for these lines have not yet been identified.

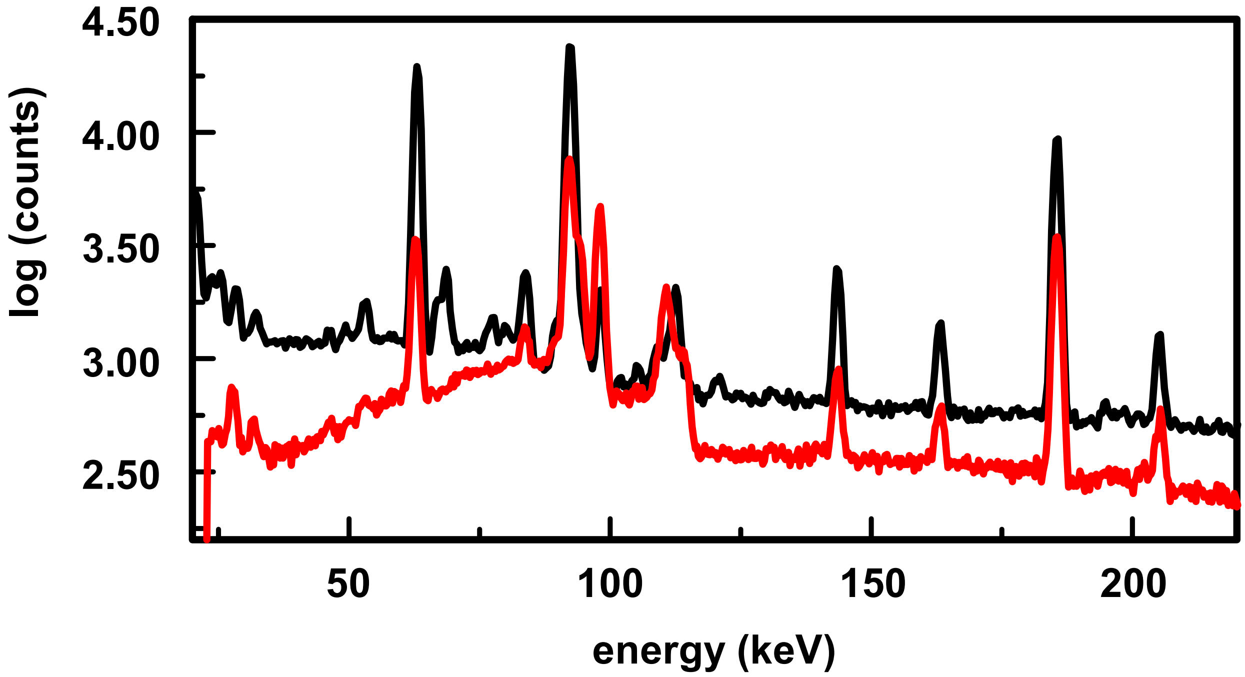

Figure 3.4-6. Gamma ray spectra of uranium before (red) and after (black) Pd/D co-deposition.

3.4.3 CR-39 results

Another diagnostic used in the uranium experiments was CR-39 detectors. Figure 3.4-7 shows a photomicrograph of tracks observed in CR-39 used in one such experiment. Among the alpha tracks due to the decay of uranium's daughters, large cylindrical tracks as the one indicated by the arrow in Figure 3.4-7a were observed. As shown by the bright streak in the overlay image, Figure 3.4-7b, this track is shallow. Such tracks have not been observed in CR-39 detectors exposed to uranium wire that had not been subjected to Pd/D co-deposition. The large track is approximately 40 µm long and 10 µm wide. It is unlikely that these tracks are due to neutrons. Figure 3.4-7 (a-c) show examples of solitary tracks observed in Au/U/Pd/D co-deposition experiments and their corresponding DT neutron tracks. These tracks are cone shaped and not cylindrical like the one shown in Figure 3.4-7. Such shallow, cylindrically shaped tracks like the one shown in Figure 3.4-7 have been attributed to higher Z charged particles.[62] Therefore, the track shown in Figure 3.4-7 is probably indicative of a fission fragment.

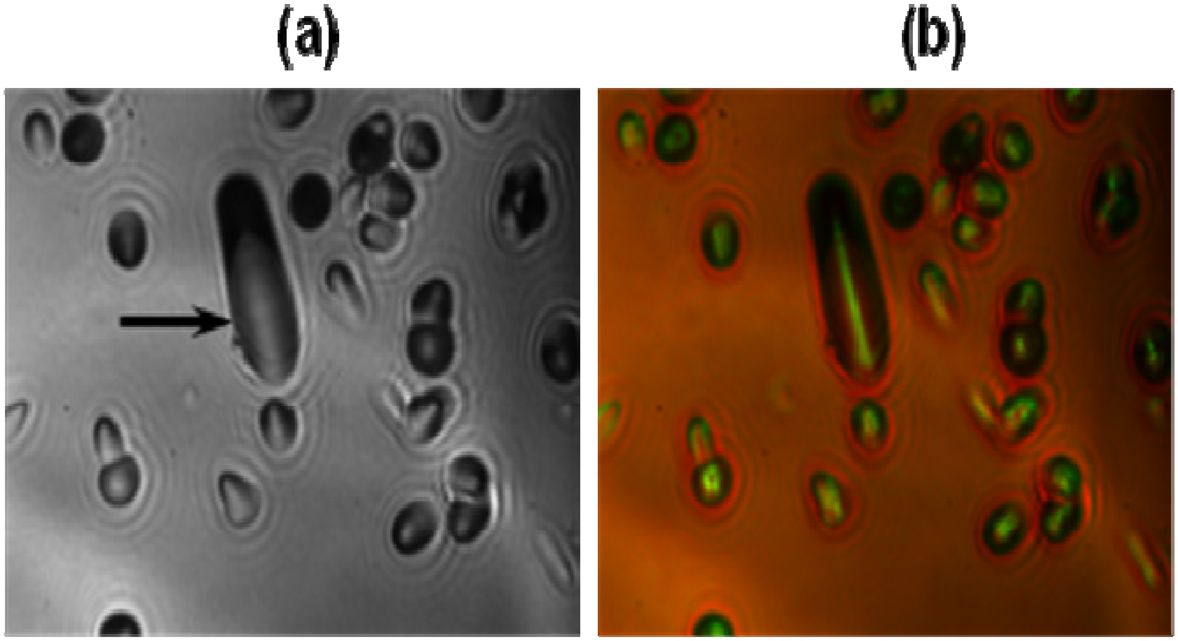

Figure 3.4-7. Photomicrographs of a CR-39 detector used in a Pd/D co-deposition experiment conducted on an Au/U cathode. Magnification 1000x. (a) Image obtained with the optics focused on the surface of the detector. (b) Overlay of two images taken at different focusing depths (surface and the bottom of the tracks). Arrow indicates a large elongated track among uranium alpha tracks.

Figure 3.4-8a, b, and c show examples of neutron generated tracks observed in the detectors used in the uranium Pd/D co-deposition experiments. Figure 3.4-8d shows an asymmetric track observed in an Au/U/Pd/D co-deposition experiment as well as a corresponding DT neutron generated asymmetric track. Examples of symmetric triple tracks are shown in Figure 3.4-9. As discussed *vide supra*, triple tracks in CR-39 detectors are diagnostic of >9.6 MeV neutrons.

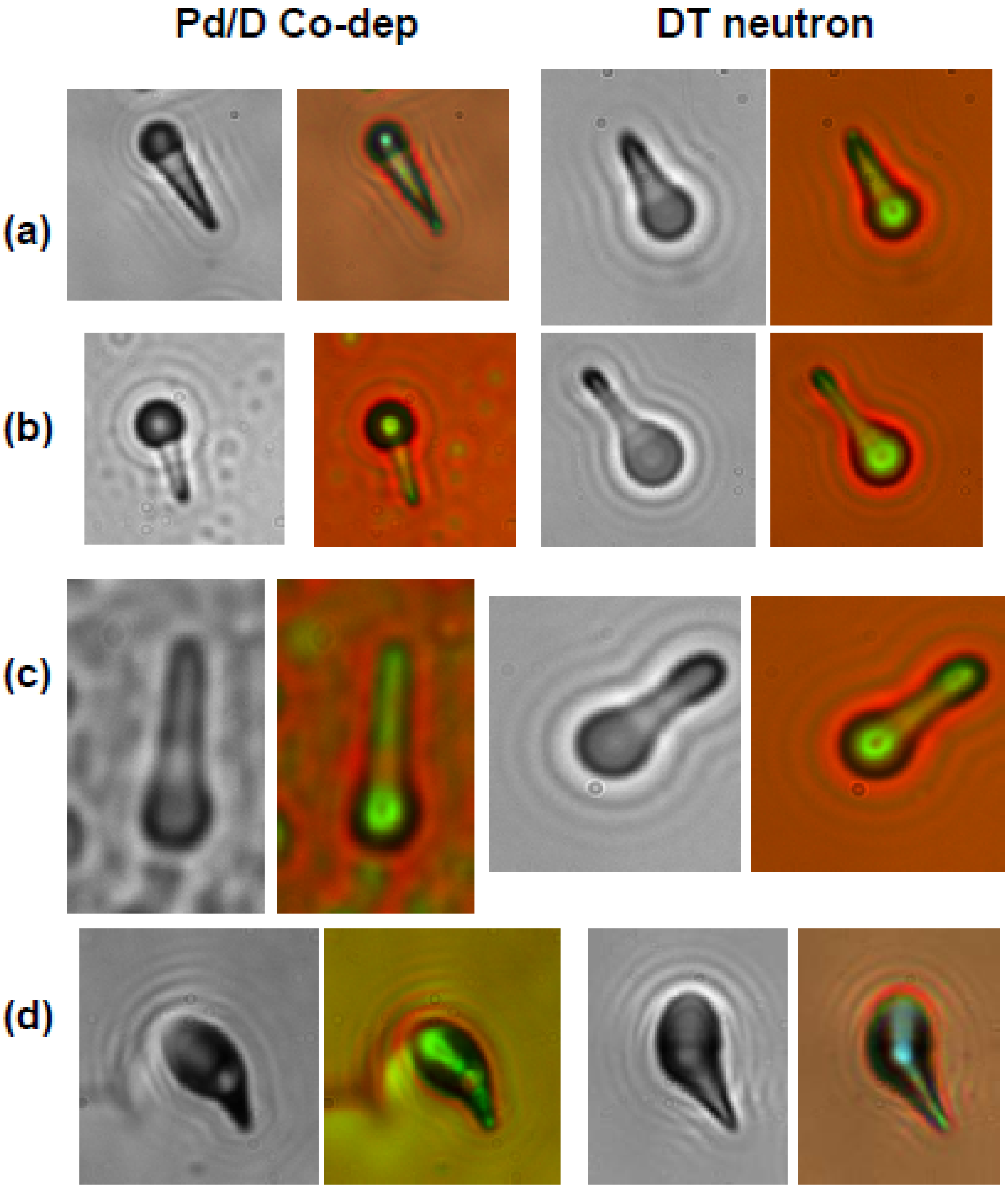

Figure 3.4-8. Photomicrographs of tracks observed in CR-39 detectors used in Pd/D co-deposition experiment conducted on an Au/U cathode and their corresponding DT neutron tracks. Magnification 1000x. The left hand images were obtained by focusing the optics on the surface of the CR-39 detector while the right hand images are overlays of two images taken at two different focal lengths (surface and bottom of the pits)

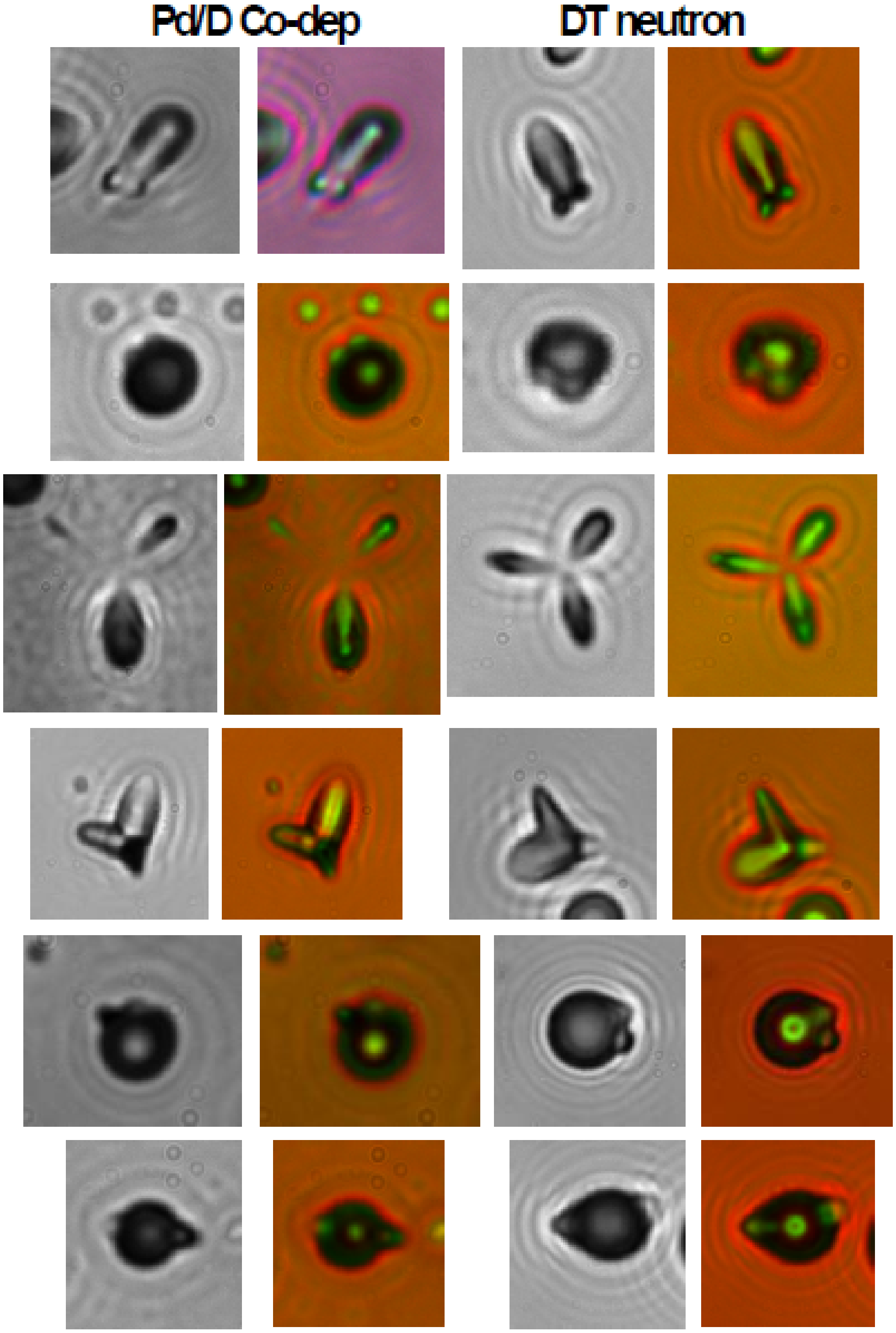

Figure 3.4-9. Photomicrographs of symmetric triple tracks observed in CR-39 detectors used in Pd/D co-deposition experiment conducted on an Au/U cathode and their corresponding DT neutron tracks. Magnification 1000x. The left hand images were obtained by focusing the optics on the surface of the CR-39 detector while the right hand images are overlays of two images taken at two different focal lengths (surface and bottom of the pits)

3.4.4 Liquid-scintillation results

The liquid scintillation technique detects gamma rays, beta emissions, and alpha particles. At the end of the Au/U/Pd/D co-deposition experiments, samples of the cathode deposit were placed in a vial containing scintillating cocktail and the spectra were obtained as a function of time. Figure 3.4-10a shows spectra of a piece of native uranium starting material as a function of time over a three month period. As can be seen, the spectra overlap. The spectrum is divided into three channels – tritium, carbon-14, and phosphorous-32. The counts per minute (cpm) for all three channels as a function of time over a three month period are plotted in Figure 3.4-10b. Within the uncertainties, the count rate for all three channels remained constant.

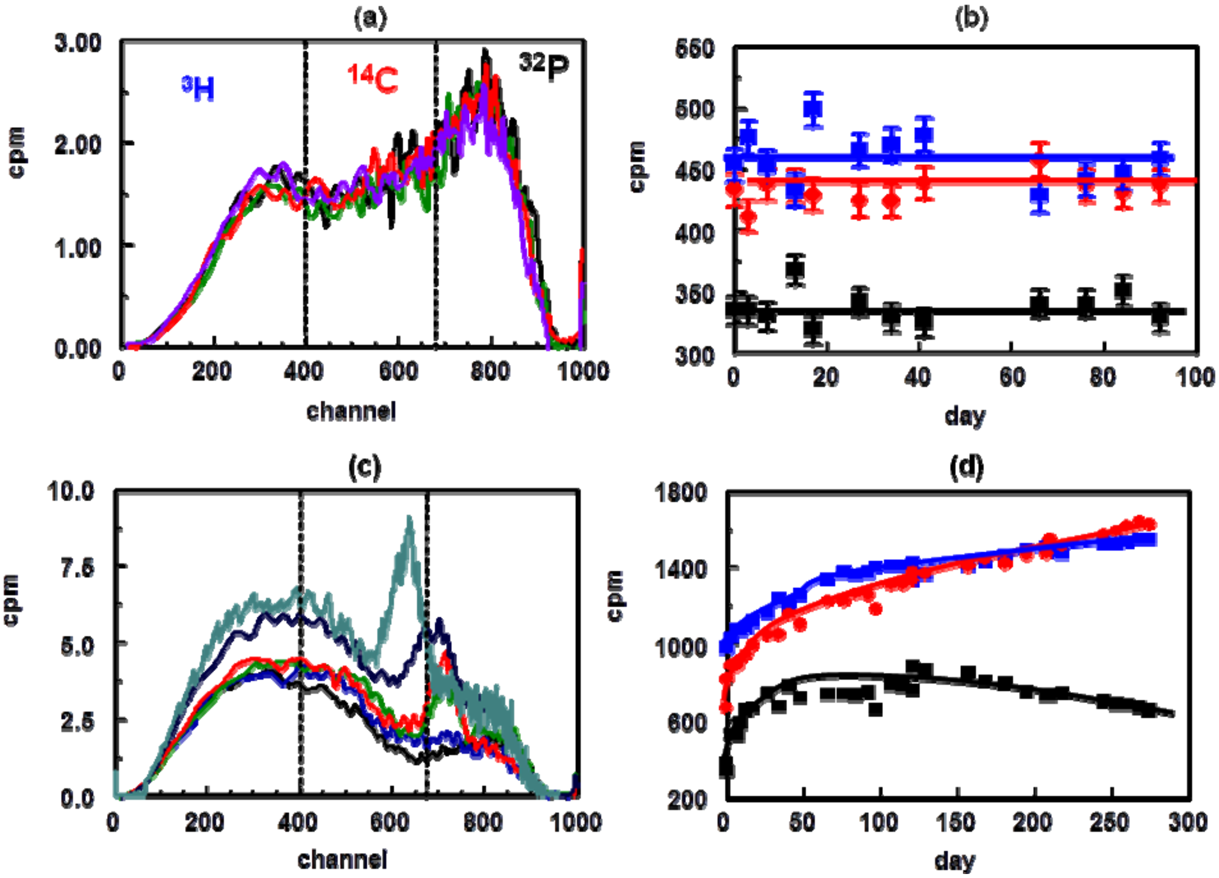

Figure 3.4-10. (a) Liquid-scintillator spectra obtained as a function of time for a piece of native uranium starting material. (b) Counts per minute (cpm) for the tritium channel (blue), carbon-14 channel (red) and phosphorous-32 channel (black) as a function of time for native uranium . (c) Liquid scintillator spectra obtained as a function of time for cathode deposit from an Au/U/Pd/D co-deposition experiment. (d) Counts per minute (cpm) Counts per minute (cpm) for the tritium channel (blue), carbon-14 channel (red) and phosphorous-32 channel (black) as a function of time for the Au/U/Pd/D cathode deposit.

Figure 3.4-10c shows spectra of the Au/U/Pd/D deposit as a function of time obtained over an eight month period. Initially a broad hump centered on channel 300 and a smaller hump centered on channel 800 were observed. Broad bands are due to gamma and beta emitters. With time, the broad hump grew larger and a narrow peak centered on channel 710 grew in (red spectrum). Narrow peaks are caused by alpha emitters. The dark blue spectrum shows what appears to be two overlapping alpha peaks centered on channels 675 and 700. With additional time, the alpha peak becomes one and shifts to lower energy (centered on channel 650). These results indicate the presence of three alpha emitters and that species are decaying to lower energy. The counts per minute (cpm) for all three channels as a function of time over an eight month period are plotted in Figure 3.4-10d. With time, the higher energy species in the phosphorous-32 channel are decaying to lower energy species in the carbon-14 and tritium channels.

3.4.5 Conclusions

The real-time HPGe spectral results obtained during the Au/U/Pd/D co-deposition experiment indicated that neutrons were generated at low current density during the plating phase. This was in agreement with the early SRI BF_3 neutron measurements discussed *vide supra.* McDaniel calculated that the average neutron energy was 6.30 and 6.83 MeV. CR-39 results showed the presence of triple tracks. These triple tracks are diagnostic of ≥ 9.6 MeV neutrons. The CR-39 results also showed the presence of large cylindrical tracks that are due to fission fragments. Both the HPGe measurements done of the cathode at the end of the experiment and the liquid scintillator spectral results provide additional evidence of the fissioning of uranium.

3.5 The Apparent Discrepancy Between CR-39 and X-ray Measurements to Detect Charged Particles

3.5.1 Introduction

Prior to the use of CR-39 to detect charged particles in these experiments, attempts were made to detect the Pd X-rays resulting from the refilling of the K shell electron orbits ionized by the passage of charged particles through the Pd lattice.[63,64] Both Bennington *et al.*[63] and Deakin *et al.*[64] used lithium drifted silicon (SiLi) detectors to detect the X-ray emissions in real time. In these experiments, no X-rays above background were detected. The main difference between the two approaches to detect charged particles is that CR-39 is a constantly integrating detector while the measurement of the X-rays using a SiLi was done in real time. The apparent discrepancy between the two approaches in detecting charged particles in the Pd/D system was examined.

3.5.2 The use of americium-241 to stimulate X-ray emissions in Pd

Bennington *et al.*[63] had shown that Pd X-rays could be stimulated by exposing a Pd foil to an ^{241}Am source. ^{241}Am is an alpha emitter. Figure 3.5-1a shows alpha spectra obtained by placing Mylar sheets between an ^{241}Am source and a silicon surface barrier (SSB) detector. It can be seen that the Mylar decreases the energy of the alphas and also causes a decrease in the number of alpha particles that can get through to reach the SSB detector. If the alpha particles emitted by the ^{241}Am source are responsible for stimulating the Pd K-shell X-rays, a corresponding decrease in the intensity of the Pd K shell X-rays is expected when Mylar is placed between the ^{241}Am source and Pd foil. Looking at Figure 3.5-1a, 18 μm of Mylar should result in a 75% decrease in intensity of the Pd K shell X-rays. Figure 3.5-1b shows X-ray spectra of the ^{241}Am source and Pd foil in the presence and absence of 18 µm of Mylar. These spectra were taken using a 15% HPGe with a beryllium window. The Pd Kα and Pd Kβ lines are identified. Additional X-ray lines are observed in these spectra. The ^{241}Am source is mounted in a metal housing. These additional lines are due to X-rays from the constituents of the metal housing that are stimulated by the emissions of the ^{241}Am source. As can be seen in Figure 3.5-1b, no decrease in X-ray intensity was observed when the 18 µm of Mylar was placed between the ^{241}Am source and the Pd foil. This indicates that something else is primarily responsible for stimulating the Pd K shell X-rays. Besides emitting alphas, ^{241}Am emits a gamma-ray at 59.54 keV. Figure 3.5-1c shows spectra of the ^{241}Am gamma-ray. When the ^{241}Am source is in contact with the Pd foil, it can be seen that the intensity of the gamma ray decreases. Figure 3.5-1c also shows that the 18 µm of Mylar has no additional affect on the intensity of the ^{241}Am gamma-ray. These results suggest that the Pd foil is absorbing the ^{241}Am gamma ray. It is the absorption of this ^{241}Am gamma ray by the Pd foil that stimulates the Pd K shell X-ray emissions. It is probably this gamma-ray, and not the ^{241}Am α particles, that stimulates the emissions observed for the housing of the ^{241}Am source, Figure 2a.

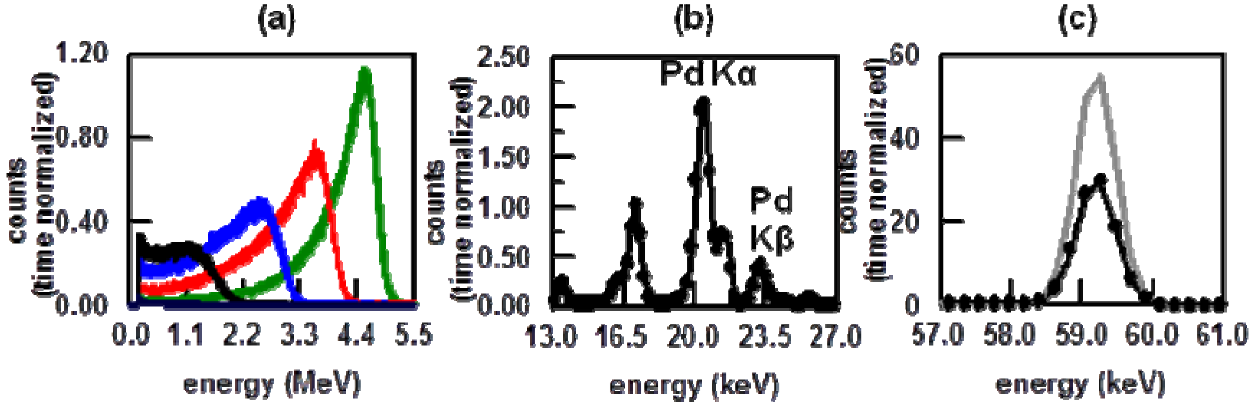

Figure 3.5-1. (a) Time normalized alpha spectra obtained by placing 0 (green), 6 (red), 12 (blue), and 18 (black) µm of Mylar between a silicon surface barrier (SSB) detector and an ^{241}Am source. (b) Time normalized X-ray spectra in the Pd K shell X-ray region obtained for a 25 µm thick Pd foil exposed to a ^{241}Am source in the presence (●) and absence (black line) of 18 µm of Mylar between the Pd foil and the ^{241}Am source. (c) Time normalized spectra of the ^{241}Am gamma-ray region where the gray line is that of the ^{241}Am source, the black line was obtained by placing the ^{241}Am source in direct contact with the 25 µm thick Pd foil, and (●) was obtained by placing 18 µm of Mylar between the ^{241}Am source and the 25 µm thick Pd foil.

To further verify that the ^{241}Am gamma ray is stimulating the Pd K shell X-rays, a 560 µm thick Cu foil was placed between the ^{241}Am source and Pd foil. The Cu foil will block all ^{241}Am alpha particles but not the ^{241}Am gamma-ray at 59.54 keV. Figure 3.5-2a (red line) shows an X-ray spectrum in the Pd X-ray region obtained for the ^{241}Am source in contact with the 560 µm thick Cu foil. The spectrum obtained by placing the 560 µm thick Cu foil between the ^{241}Am source and Pd foil is also shown in Figure 3.5-2a (black line). The observed spectrum is cleaner than that observed for ^{241}Am source in direct contact with the Pd foil, black line Figure 3.5-1b.

The results in Figure 3.5-2a shows that the Cu foil absorbs the majority of the gamma-ray induced emissions due to the source housing. Figure 3.5-2b shows the spectrum of the Pd foil in which the contributions of the ^{241}Am source and Cu foil are subtracted out. This difference spectrum shows Pd Kα X-rays at 21.1 keV and Pd Kβ at 23.85 keV. Figure 3.5-2c shows the spectra of ^{241}Am gamma ray of the ^{241}Am source alone and in contact with the Pd foil, Cu foil, and both Pd and Cu foils. These spectra show the absorption of the ^{241}Am gamma ray when the Pd and/or Cu foils are exposed to the source. Because the Cu foil is thicker, it attenuates the signal more.

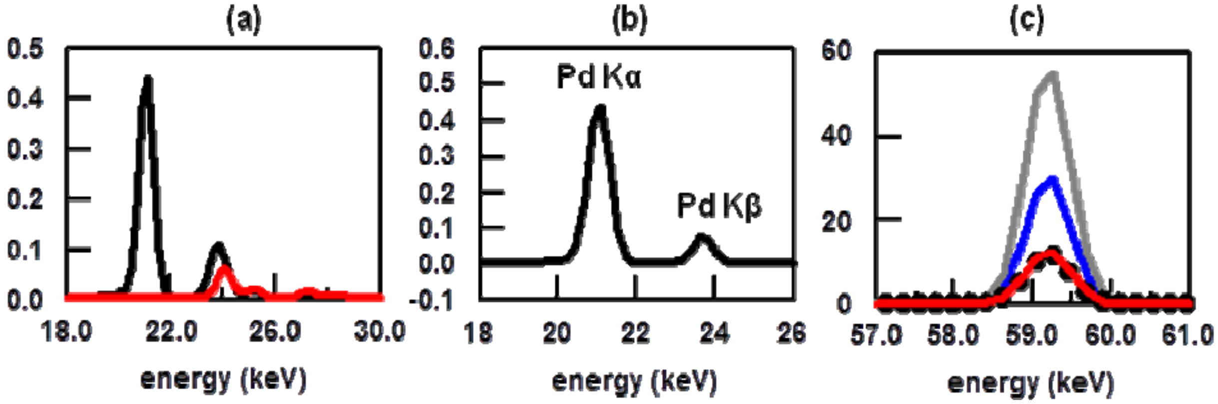

Figure 3.5-2. (a) Time-normalized X-ray spectra in the Pd K shell X-ray region where the red line was obtained with the ^{241}Am source in direct contact with the 560 µm thick Cu foil and the black line was obtained by placing the 560 µm thick Cu foil between the ^{241}Am source and the 25 µm thick Pd foil. (b) X-ray spectrum of the Pd foil in which the contributions of the ^{241}Am-Cu emissions have been subtracted out. The large line at 21.1 keV is due to the Pd Kα X-rays and the smaller line at 23.85 keV is assigned to the Pd Kβ X-rays. (c) Time normalized spectra of the ^{241}Am gamma-ray region where the gray line is that of the ^{241}Am source, the blue line was obtained by placing the ^{241}Am source in direct contact with the 25 µm thick Pd foil, the red solid line was obtained by placing the ^{241}Am source in direct contact with the 560 µm thick Cu foil, and (●) was obtained by placing the 560 µm Cu foil between the ^{241}Am source and the 25 µm thick Pd foil.

3.5.3 The use of polonium-210 to stimulate X-ray emissions in Pd

The experimental results obtained using an ^{241}Am source showed that the gamma-ray at 59.54 keV was primarily responsible for stimulating the Pd K shell X-ray emissions that were measured and not the alpha particles. This is due to the fact that gamma rays are much more penetrating than alpha particles. To evaluate the stimulation of X-rays by alpha particles, a source that decays purely by alpha emission, ^{210}Po, was obtained. The source, which was mounted in a plastic housing, had an initial activity of 0.1 µCi. Figure 3.5-3a shows alpha tracks in CR-39 obtained by exposing the detector to the ^{210}Po source for three minutes. The observed number of tracks is consistent with a 0.1 µCi alpha source.

A gamma-ray spectrum of the ^{210}Po source was obtained by placing the source inside the lead cave and pressed against the Be window of the HPGe detector. Figures 3.5-3b and c show spectra obtained for the lead cave with and without the ^{210}Po source. The spectra were time normalized. From the spectra, it can be seen that three new gamma/X-ray lines at 14.8, 21.9, and 121.7 keV are present in the ^{210}Po source spectrum. As ^{210}Po is a pure alpha emitter, these new lines cannot be due to ^{210}Po. Compared to the ^{241}Am gamma line at 59.54 keV, Figure 3d, the three gamma/X-ray lines seen in Figures 5d and 5e are very small and are attributed to gamma/X-ray emitting contaminant(s) in the ^{210}Po source.

While the presence of the contaminant in the ^{210}Po source was unexpected, it presented an opportunity to separate and quantify the alpha/gamma contributions in stimulating the Pd K shell X-rays. This was not possible using the ^{241}Am source due to the intensity of the ^{241}Am gamma ray. To isolate and quantify the alpha/gamma contributions, a 100 µm thick acrylic sheet was placed between the Pd foil and the ^{210}Po source. The acrylic sheet will block the alphas from the ^{210}Po but not the gamma/X-rays from the contaminant(s). The time normalized results are summarized in Figure 3.5-4. All spectra were obtained by placing the source in direct contact with the Be window of the HPGe detector. When the source is perpendicular to the Be window, no gamma/X-rays due to the contaminant or to Pd Foil in contact with the source are observed. In Figure 3.5-4, light green blocks indicate the regions of the gamma lines due to unknown contaminant(s) in the ^{210}Po source and the pink box indicates the region of the Pd Kα lines.

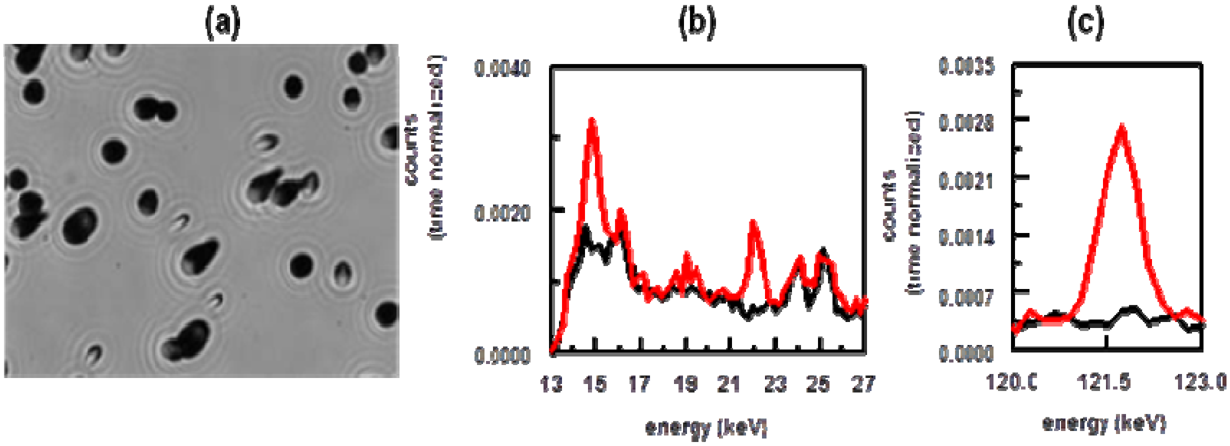

Figure 3.5-3. (a) Photomicrograph of alpha tracks, at 1000x magnification, obtained by exposing CR-39 to a 0.1 µCi ^{210}Po source for three minutes. Time-normalized, X-ray spectra obtained for the background (black line) and the 0.1 µCi ^{210}Po source (red line) for the spectral regions (b) 13-27 keV, and (c) 120-123 keV. The spectrum of the ^{210}Po source was obtained by placing the source in direct contact with the Be window of the HPGe detector.

Figure 3.5-4a shows the spectrum obtained for the Pd foil. The foil was 25 µm thick and had an area of 16.1 cm^2. A very small peak due to the Pd Kα shell X-rays was observed in the spectrum. The lead cave X-rays between 36 and 102 keV are probably responsible for stimulating the Pd K shell X-rays resulting in the peak seen in Figure 3.5-4a. Deakin *et al.*[64] also observed that room background radiation caused the Pd cathode to fluoresce and a line due to Pd K X-rays was present as an artifact in the background.

The spectrum obtained for the ^{210}Po source is shown in Figure 3.5-4b. Only noise is observed in the region of the Pd K shell X-rays. Two gamma/X- rays at 14.8 and 21.9 keV, due to unknown contaminant(s), were observed in the spectrum. The spectrum obtained when the Pd foil in contact with the ^{210}Po source is shown in Figure 3.5-4c. The line due to the Pd K shell X-rays is more prominent than that observed in the background. When a 100 µm thick acrylic sheet is placed between the Pd foil and the ^{210}Po source, a decrease in the line due to the Pd K shell X-rays is observed, Figure 3.5-4d.

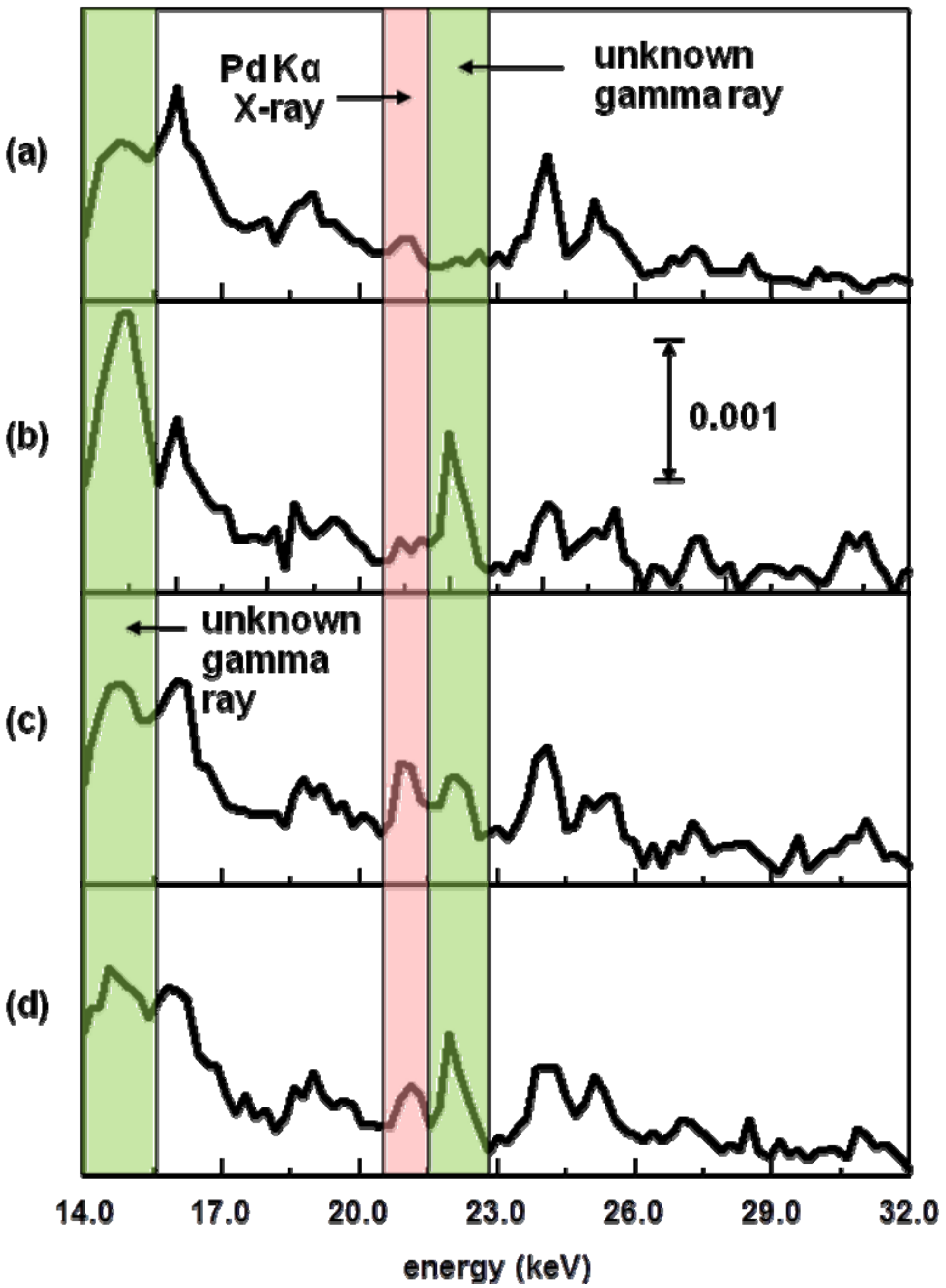

Figure 3.5-4. Time-normalized X-ray spectra in the Pd K shell X-ray region obtained with the sample in contact with the Be window where (a) is the 25 µm thick, 16.1 cm^2 area Pd foil, (b) is the ^{210}Po source, (c) is the Pd foil in direct contact with the ^{210}Po source, and (d) has a 100 µm thick acrylic film between the Pd foil and the ^{210}Po source. The green boxes indicate the regions of the gamma lines at 14.8 and 21.9 keV due to unknown contaminant(s) in the ^{210}Po source. The pink box indicates the region of the Pd Kα lines. All spectra were measured in a lead cave lined with Sn and Cu.

Compared to the ^{210}Po source spectrum, Figure 3.5-4b, a decrease is observed in the intensities of the unknown contaminant gamma rays at 14.8 and 21.9 keV. These spectra indicate that both the ^{210}Po α particles and the γ-rays from the unknown contaminant are stimulating the emission of Pd K shell X-rays.

Table 1 summarizes the measured intensities of the Pd Kα lines in Figure 3.5-4 as well as the sources of the stimulation. It is assumed that the background, ^{210}Po α-particle, and unknown contaminant γ-ray stimulations contribute equally to the Pd Kα emissions of the Pd-^{210}Po sample, Figure 3.5-4c. With this assumption, the estimated contributions of each source in stimulating the Pd Kα emissions are 35.2 % due to background, 44.4 % due to the ^{210}Po α-particles, and 20.4 % due to the unknown contaminant gamma/X-ray.

Table 3.5-1. Analysis of the Pd Kα line shown in the spectra in Figure 3.5-4.

Sample[a]	Intensity of Pd Kα line[b]	Cause of Stimulation[c]
^{210}Po source	0.00	none
Pd foil	0.00019	bkg
^{210}Po-Pd foil	0.00054	bkg + α + γ
^{210}Po-100 μm acrylic-Pd foil	0.00030	bkg + γ

a. All samples were measured in a Pb cave that was lined with Sn and Cu foil.
b. Spectra have been time normalized. Pd Kα line is shown in Figure 7.
c. Bkg = background stimulation, α = alphas from ^{210}Po source; γ = gamma rays from the unknown contaminant(s) in the ^{210}Po source

3.5.4 Implications to the CR-39 detection results

The Pd/D co-deposition experiments typically ran for two weeks. Figure 3.5-5a shows the experimental configuration used in an experiment in which an external 6000 V DC (with a 6% AC ripple) electric field was applied across the cell after the Pd had been plated out. The 6% AC component allows coupling of the electric field into the cathode. In this particular experiment, Pt, Ag, and Au wires were connected in series, over the CR-39 detector, as shown in Figure 3.5-5a. The detector used in this experiment was scanned using an automated scanning track analysis system to obtain quantitative information on the pits produced in the CR-39. The system has a high quality microscope optical system (Nikon cfi series) operating at a magnification high enough to discriminate between tracks and background. Figure 3.5-5b shows the spatial orientation of positively identified tracks in the CR-39 detector used in the three wire experiment. It can be seen that track density correlates with the placement of the wires.

Figure 3.5-6a shows a microphotograph of tracks in the CR-39 detector taken by the scanner. Each image taken by the scanner is then analyzed by the proprietary software. In Figure 3.5-6b, each numbered rectangle represents an object in the detector identified by the computer algorithm. The computer algorithm then makes 15 characteristic measurements of each object located in the image to provide reliable discrimination between etched tracks and background features present on or in the plastic detectors. These measurements include track length and diameter, optical density (average image contrast) and image symmetry. Based upon the measured properties of a feature, the computer algorithm of the automated scanning system determines whether or not the measured features are consistent with that of an energetic particle. The software algorithms ignore overlapping tracks. Figure 3.5-6c summarizes the results of this analysis. The green colored rectangles are positively identified tracks.

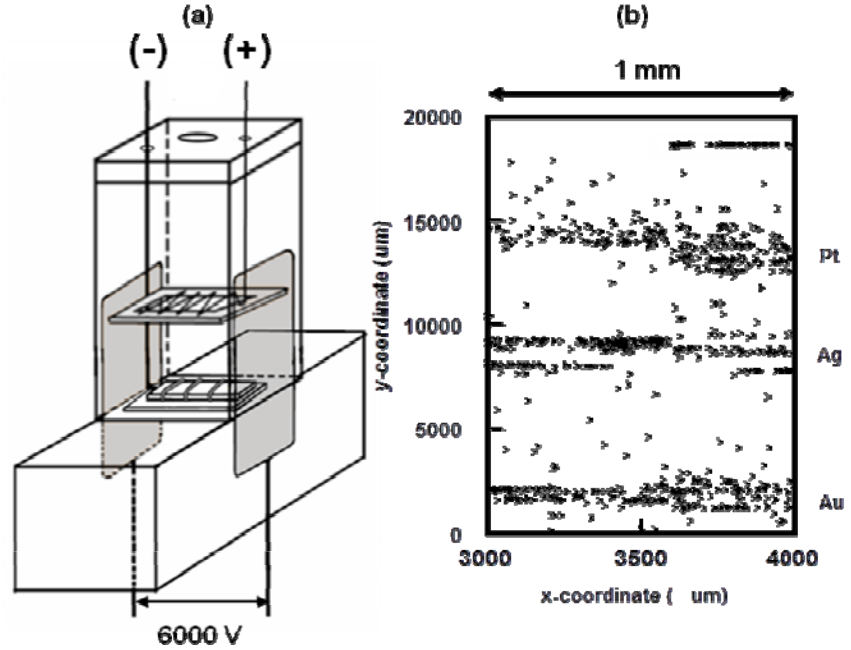

Figure 3.5-5. (a) Schematic of a cell used in an E-field experiment. The cathode is composed of a Pt, Ag, and Au wire electrodes connected in series. The external voltage applied is 6000 V DC with a 6% AC ripple. (b) Spatial distribution of positively identified tracks obtained by scanning a 1 mm x 20 mm area on a CR-39 detector used in a Pd/D co-deposition experiment done in the presence of an external E-field. Total number of positively identified tracks is 1079. Placement of the Pt, Ag, and Au wires is indicated.

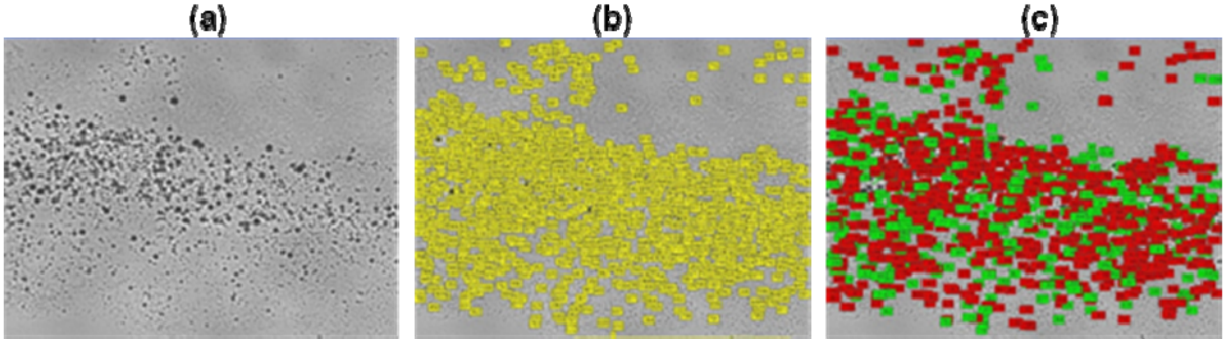

Figure 3.5-6. (a) Photomicrograph of tracks observed in a CR-39 detector used in a Pd/D co-deposition experiment. The photomicrograph was obtained using the automated system at a magnification of 200x. (b) The image shown in (a) after undergoing computer processing and objects have been identified and numbered. These objects are indicated by the yellow colored rectangles. (c) Based upon measurements of object symmetry and contrast, the computer algorithm identifies tracks whose properties are consistent with those of nuclear generated tracks. These tracks are indicated by the green colored rectangles.

The area of the CR-39 detector scanned in Figure 3.5-5b is 1mm x 20 mm. The total number of tracks positively identified by the scanner in this area was 1079. To determine whether or not Pd K shell X-rays would have been observed in the experiment, it is assumed that the observed tracks are due to charged particle interactions with the detector and not neutrons. As shown in Figure 3.5-6c, the number of tracks in this one image is undercounted by a factor of ~3. Therefore, at a minimum, the number of tracks is undercounted by a factor of 30. However, the charged particle stimulation of the Pd K shell X-rays will occur throughout the Pd deposit. Ignoring absorption of the Pd K-shell X-rays by the Pd deposit and cell components, in the worse-case scenario, it is estimated that the charged particles are undercounted by a factor of 1000. The total area of the detector is 10mm x 20 mm. Taking this larger detector area into account, the charged particles are estimated to be undercounted by a factor of 10000. Therefore, in this worst case scenario, the number of charged particles is 1.079×10^{7}. For a two week experiment (1.2096×10^{6} s), the rate of particle production is estimated to be 8.9 particles s^{-1}. The 0.1 μCi ^{210}Po α source decays at a rate of 3700 particles s^{-1}. As summarized in Table 1, the peak intensity due to the stimulation of the Pd K shell X-rays by 3700 α particles, in the time normalized spectrum, is 2.4×10^{-4}. The increase in peak intensity of 8.9 charged particles, in the time normalized spectrum, is calculated to be 5.8×10^{-7}. This is too small an increase in peak intensity to see in the measured spectrum. In addition, the experimental configuration for the E-field experiment is equivalent to the 'perpendicular to the window' configuration. In this configuration, no Pd K shell X-rays would have been observed.

3.5.5 Conclusions

In this investigation, Pd K shell X-rays were stimulated when a thin Pd foil was placed in contact with a ^{241}Am source. However, it was found that the ^{241}Am gamma ray at 59.54 keV, and not the alpha emissions, was primarily responsible for the stimulation of the Pd K shell X-rays. These results emphasize the need to properly characterize RAM sources when doing calibrations. This was particularly borne out when conducting experiments using a ^{210}Po source, which was supposed to be a pure alpha emitter. Measurements of the ^{210}Po source, using the HPGe detector, showed the presence of three weak gamma-/X-ray lines attributed to unknown contaminant(s). However, use of this source in these experiments made it possible to separate and quantify the alpha/gamma contributions in stimulating the Pd K-shell X-rays.

Using the 0.1 μCi ^{210}Po source, it was found that the orientation of the source relative to the HPGe detector head determined whether or not the Pd K-shell X-rays would be observed. The Pd K-shell X-rays were observed when the ^{210}Po source was directly facing the detector head. No Pd K-shell X-rays were seen when the ^{210}Po source was perpendicular to, or 'not-facing,' the HPGe detector head. Consequently, no Pd K-shell X-rays would have been detected in the electrolysis Pd/D co-deposition experiments. In addition, it was found that, although tracks significantly above background were observed in CR-39 detectors used in Pd/D co-deposition experiments, the rate of charged particle production was too low to be detected by the Pd K shell X-ray emissions.

3.6 Temporal Measurements of Radiation, Neutrons, and Charged Particles

3.6.1 Pd/D co-deposition experiment on Au

A Pd/D co-deposition experiment was done in a lead cave. The cell was similar to that shown in Figure 3.1-1. Instead of Ag wire, the cathode substrate was Au wire. The diagnostics were a 65% HPGe with an Al window and CR-39 in contact with the cathode. A 60 µm thick polyethylene film separated the cathode from the CR-39 detector.

Electrolyte was placed in the cell. The cell was put inside the Pb cave. The working and counter electrodes were hooked up to a potentiostat. Figure 3.1-1 shows spectra obtained with the HPGe. When no current was flowing, a peak at 59.6 keV was observed. No peaks due to the background appear at 59.6 keV. Even though no current is flowing, two dissimilar metals (Au and Pt) are immersed in an electrolyte and are connected via a potentiostat. This is essentially a battery. As shown in Figure 3.1-1b, when current is applied, this peak disappears with time. Figure 3.1-1c shows a plot of peak counts as a function of time.

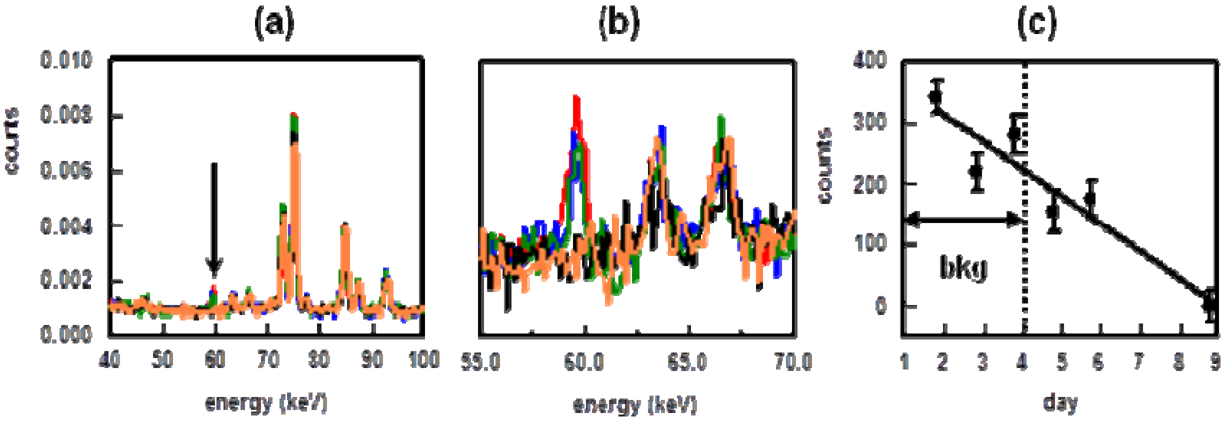

Figure 3.6-1. Time-normalized HPGe spectra obtained during the early stages of Pd/D co-deposition where (a) is the spectral region between 20 and 100 keV (arrow indicates a peak at 59.6 keV that is not a background peak) and (b) is the spectral region between 55 and 70 keV. Red is background with electrolyte in the cell, no current, experimental day 4, blue is electrolysis at -100 µA day 5, green is for day 6 at -200 µA, black is day 9 at -200 µA, and orange is day four of electrolysis at -200 µA. (c) Counts of the 59.6 keV peak as a function of time.

After the Pd plated out, the current was ramped up. Figure 3.6-2a shows spectra obtained when the electrolytic current was increased. The left hand side shows spectra between 20-100 keV. As the current increased, a broad peak at 25-35 keV grew in. These spectra also show γ-ray peaks due to the background. The narrowness of the background peaks indicate that the detector is operating properly and that the electronics are not drifting or malfunctioning. Therefore the broad peak between 25-35 keV is real and not an artifact.

The shape of the broad peak indicates that multiple species are present, as shown by the right hand spectra in Figure 3.6-2a, a single broad peak, centered at 28.7 keV, is observed when the applied current is -50 mA. The intensity of this peak increases for an applied current of -75 mA. For an applied current of -100 mA, two peaks centered at 28.4 and 31.6 keV are observed.

When the cell is turned off, the broad peak at 25-35 keV remains, Figure 3.6-2b. The background γ-ray lines are still narrow. The spectra on the right hand side, Figure 3.6-2b, shows a decrease on the high energy side. A plot of the peak area of this broad peak as a function of time is shown in Figure 3.6-3. This analysis was done by Dr. Patrick McDaniel. This plot shows that the peak area of this broad peak increases when the applied current increased. When the current was shut off, the peak area decreases. Two maxima were observed in the plot indicating the decay of multiple species.

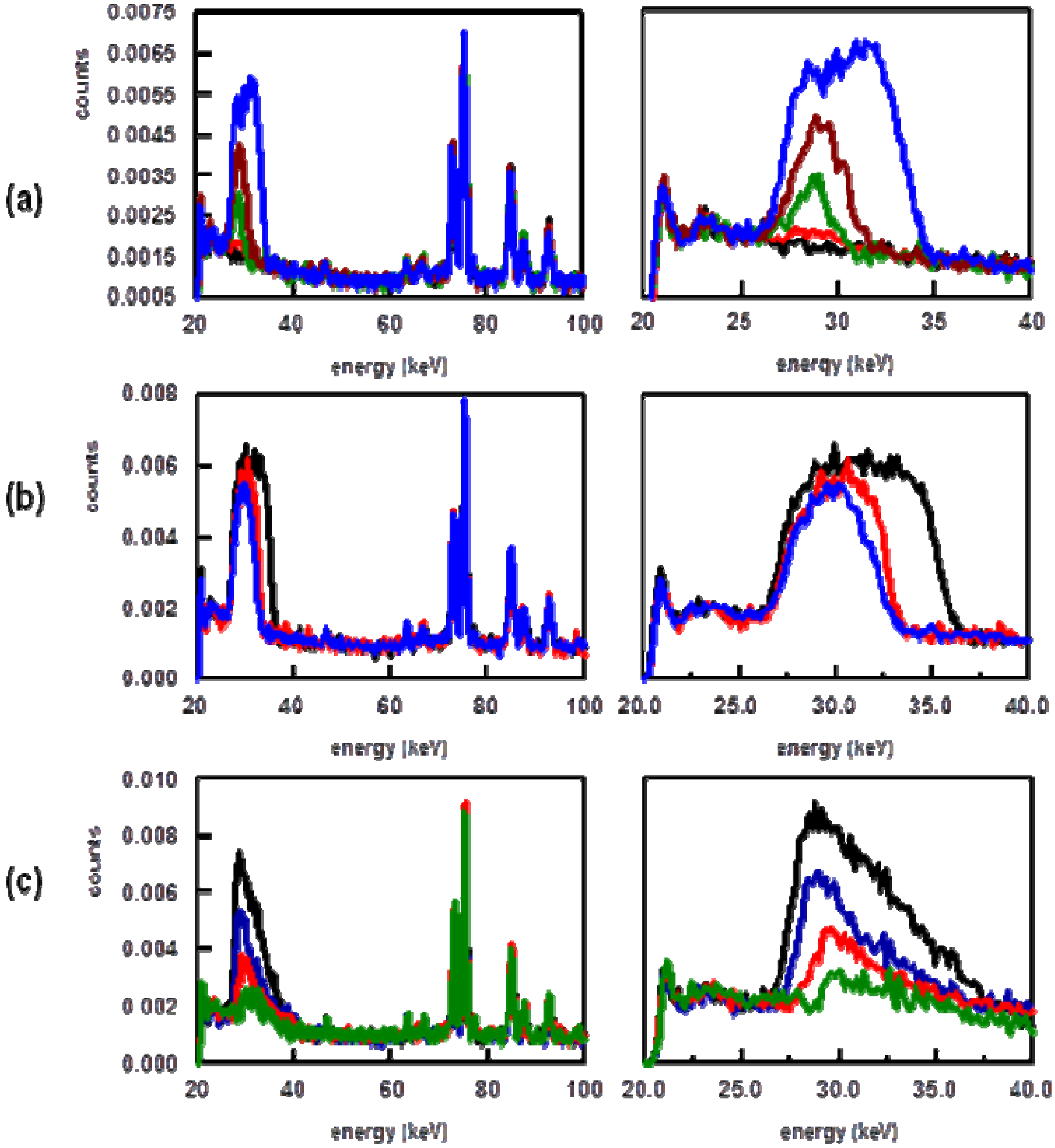

Figure 3.6-2. Time normalized HPGe spectra where: (a) spectra obtained during electrolysis (black = -0.5 mA; red = -25 mA; green = -50 mA; brown = -75 mA; blue = -100 mA); (b) spectra obtained with the cell turned off (black is day 1, red is day 9, and blue is day 11); and (c) spectra obtained with the cell removed from the Pb cave (black is day 2, blue is day 4, red is day 6, and green is day 9).

Upon seeing the data, Dr. McDaniel suggested pulling the cell out of the Pb cave and to resume data acquisition. This was done and the spectra obtained with the cell removed from the Pb cave are shown in Figure 3.6-c. The γ-ray peaks due to the background are still narrow indicating that the detector has not drifted or sustained neutron damage. After nine days the broad peak at 25-35 keV decayed away.

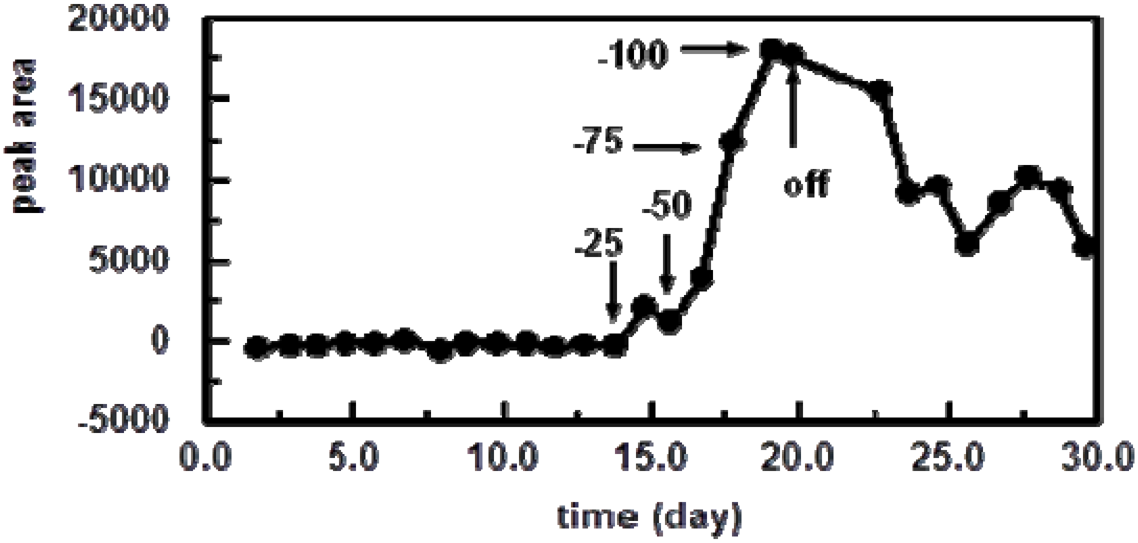

Figure 3.6-3. Plot of the peak area of the broad peak between 25-35 keV as a function of time. The cell was in the Pb cave the whole time. Applied current, in mA, is indicated.

The results summarized in Figure 3.6-2 indicate that the broad band between 25 and 35 keV is not due to a either γ- or X-rays. For an HPGe detector, lines due to γ- and/or X-rays are narrow. This is illustrated by the narrow γ-ray lines due to the background. The fact that there was still a broad peak observed when the cell was taken out of the Pb cave indicates that something inside the HPGe detector became activated. The only species that could have traveled away from the cell, gone though the Al window, and gotten inside the detector is neutrons. The broadness of the band between 25-35 keV indicates that the neutron-activated species is undergoing beta decay. The decaying spectra in 3.6-2c is characteristic of bremstrahlung radiation, in this case, induced by the beta decay of one or more activated elements within the detector, the detector housing or the cryostat.

Figure 3.6-4 shows tracks observed in the CR-39 detector used in the Au/Pd/D experiment. The tracks are similar to what had been described *vide supra*. A triple track is circled in Figure 3.6-4a. This triple track provides additional evidence of the production of high energy neutrons during the Pd/D co-deposition process. Shallow tracks are also observed. These are latent tracks which are deeper inside the plastic. These latent tracks could have been caused by either neutrons or high energy protons.

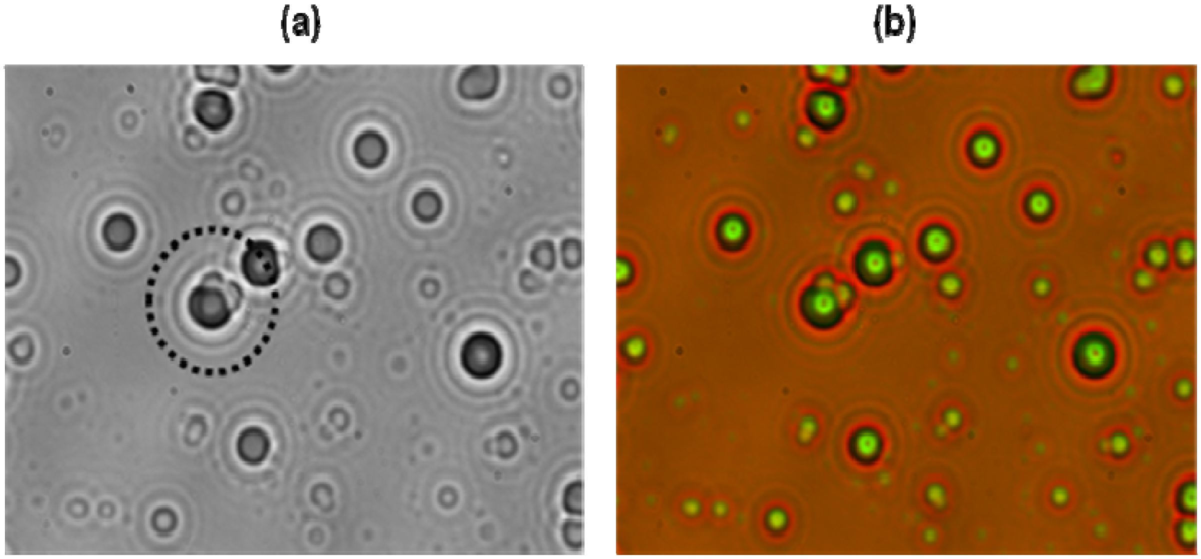

Figure 3.6-4. Photomicrographs of tracks observed in the CR-39 detector used in the Au/Pd/D co-deposition experiment where (a) was obtained with the microscope optics focused on the surface of the detector (a triple track is circled) and (b) was obtained with the microscope optics obtained at two focusing depths (surface and bottom of the pits).

3.6.2 Silicon surface barrier measurement

An experiment was conducted using a silicon surface barrier detector to detect charged particles in real time. Figure 3.6-5a shows a schematic of a cell that was assembled to conduct these real-time measurements. A circular hole was cut into the bottom of the butyrate cell. A 6 µm thick Mylar window was epoxied over the hole using aquarium RTV silicone. Figure 3.6-5b shows a schematic of the Au cathode. The Au wires making up the cathode are pressed against the Mylar window. To decrease scattering, a 100 µm thick acrylic collimator, shown in Figure 3.6-5b, was placed on the outside of the cell. The holes cut into the collimator line up with the gold wires. This collimator only allows particles traveling perpendicular to the surface to enter the silicon barrier detector. Once assembled the cell was filled with electrolyte and placed on top of a silicon barrier detector.

Results of the experiment are summarized in Figure 3.6-6. A plot of counts per day for the energy region 1.0 to 1.5 MeV is shown in Figure 3.6-6a. The arrow indicates when the current was applied to the cell. An increase in the number of counts was observed which immediately dropped down by the next day. This decrease is not surprising. As discussed *vide supra*, as Pd plates out, the increasing Pd deposit will impede charged particles from reaching the silicon barrier detector. There is also the effect of the Mylar window on the number of observed charged particles. Linear energy transfer curves indicate that the 6 µm thick Mylar window will cut off < 0.45 MeV protons, < 0.55 MeV tritons, < 1.40 MeV ^{3}He, and < 1.45 MeV alphas. In an earlier experiment[42] in which the CR-39 detector was outside the cell and a 6 µm thick Mylar film separated the cathode and the CR-39 detector, it was observed that ~ 90% of the charged particles was blocked.

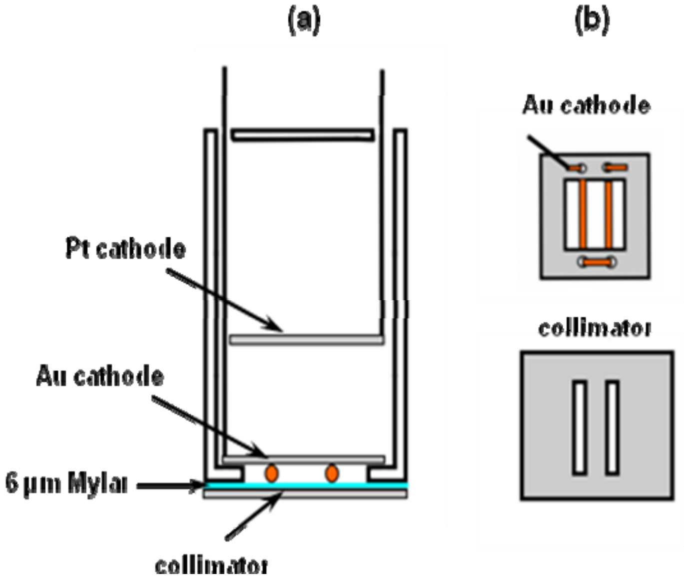

Figure 3.6-5 (a) Side view schematic of the cell used in the silicon surface barrier detector experiment. (b) Schematics of the Au-wire cathode and collimator used in the experiment.

Figure 3.6-6b is a plot of the count rate on the fourth day divided by the count rate on the third day *vs.* energy. It is an attempt to characterize the energy of the charged particles observed for the first day of electrolysis. The plot shows that the majority of the charged particles formed have energies between 1.0 and 2.0 MeV. These conclusions are in agreement with earlier CR-39 detector results showing the similarity between Pd/D co-deposition results and 1 MeV alpha particles, shown in Figure 3.2-7.

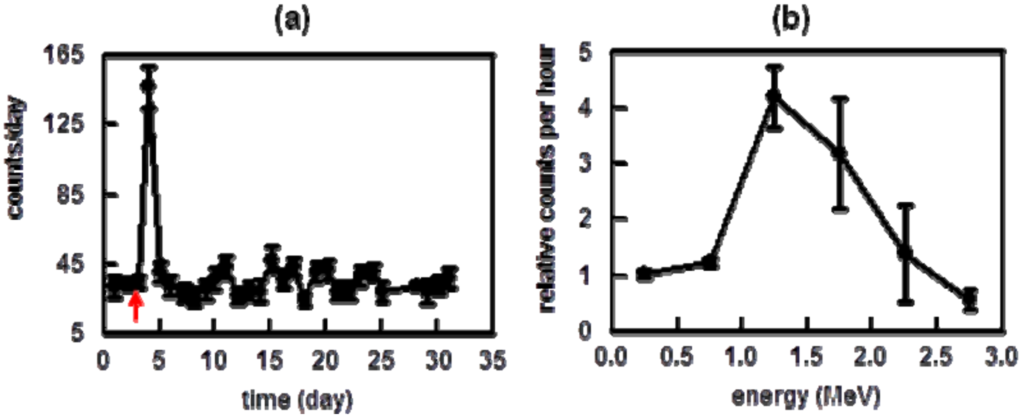

Figure 3.6-6 (a) Silicon barrier counts per day for the 1.0-1.5 MeV energy region. Arrow indicates when the current was turned on. (b) Relative counts per hour (day 4 count/day 3 bkg count) as a function of energy (MeV).

3.6.3 Summary of Pd/D co-deposition on Ni screen

Figure 3.6-7a shows a photograph of the cell used in a Pd/D co-deposition experiment done on Ni screen. The cell is equipped with a heater. When the photograph was taken, the Pd had completely plated out. During the plating phase, the cell was monitored using a NaI(Tl) scintillation detector to monitor for γ-/X-ray emissions. After plating was complete a bubble detector was placed close to the cell to detect neutron emissions. The bubble detector can be seen on the right hand side of the photograph. A second bubble detector was placed in another room to monitor the background. Bubble detectors are comprised of tiny droplets of superheated liquid that are dispersed throughout a clear polymer.[65] When a neutron strikes a droplet, the droplet immediately vaporizes forming a visible gas bubble trapped in the gel. Figure 3.6-7b shows a photograph of a bubble detector that had been exposed to neutrons from a Pu-Be source. Each bubble was caused by a single neutron. The sensitivity of bubble detectors to neutrons is 10^{-5}. Although easy to use, bubble detectors have a three month lifetime.

The bubble detector results are summarized in Figure 3.6-8. It can be seen that more bubbles were seen for bubble detectors near the cell than were observed for the background. It can also be seen that neutron emissions correlate with changes in current. No correlation was observed for neutron emissions and either heater pulses, addition of D_2O, or laser illumination of the cathode. Probability analysis was used to analyze the data. The results for the cell and background are summarized in Figure 3.6-9 and Table 3.6-1. From the analysis, the average number of neutrons per day for the cell was 69,200 ± 6,600 and the background was 12,600 ± 3,300. The neutron emission rate for the cell was estimated to be 0.8 n/s, which is in agreement with the neutron emission rate calculated by Lipson and Roussettski in their analysis of the CR-39 detector used in the SRI replication discussed *vide supra*.

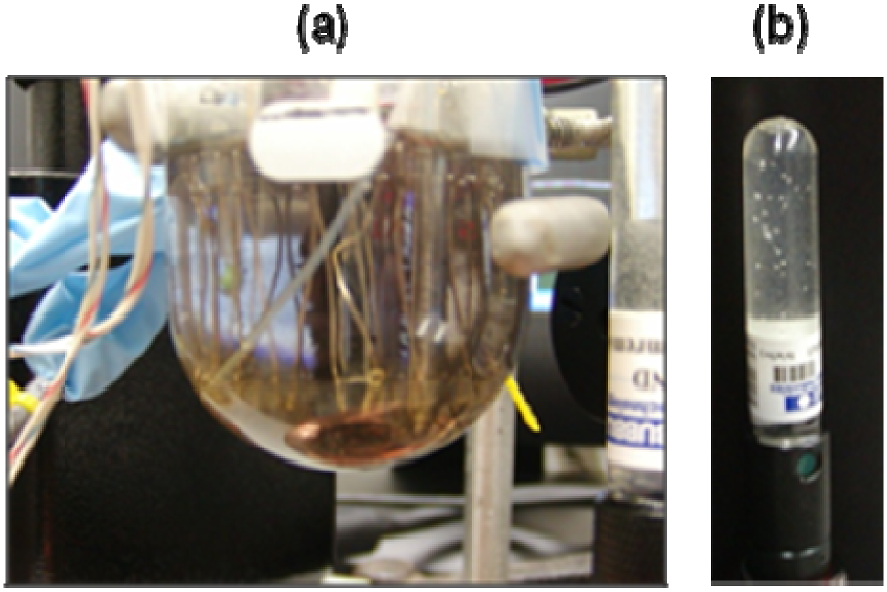

Figure 3.6-7 (a) Photograph of a cell used in a Pd/D co-deposition experiment. The cathode was Ni screen. A bubble detector is shown on the right hand side. (b) Photograph of a bubble detector that had been exposed to a Pu-Be neutron source.

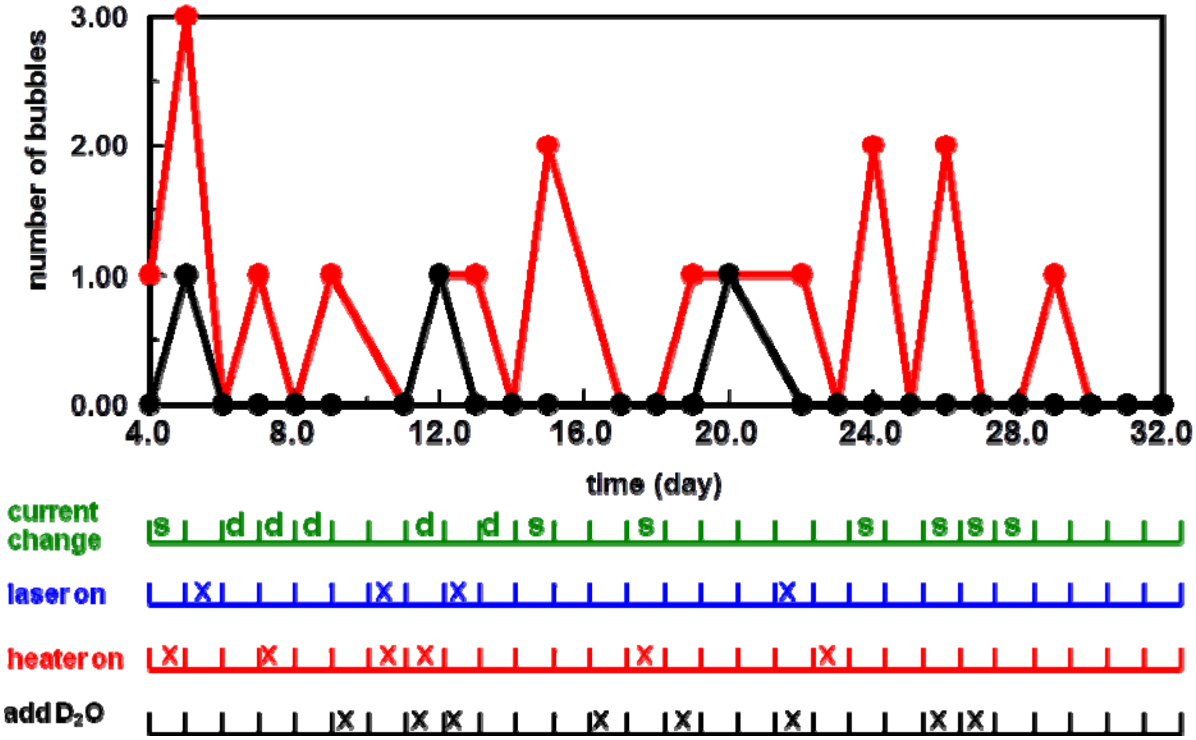

Figure 3.6-8. Bubble detector results where red is for the cell and black is the background. Measurements began after the Pd was plated out. Current changes (where S means superwave, d means DC), heater pulses, addition of D_2O, and HeNe laser illumination of the cathode are indicated.

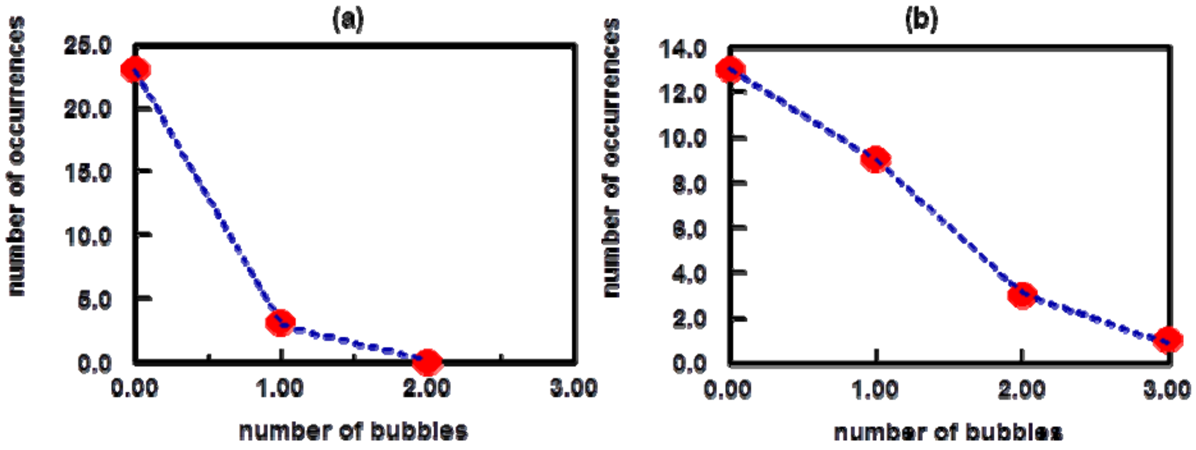

Figure 3.6-9. Summary of probability analysis done for (a) background and (b) cell. Data ponts are indicated by (●) and calculated by (▪▪▪▪▪▪▪).

Table 3.6-1. Results of probability analysis of bubble detectors.[a]

Sample	P_0 = average number of neutrons per day	Correlation
background	12,600 ± 3,300	0.99993
cell	69,200 ± 6,600	0.99964

a. Number of observations = 26

The advantage of NaI(Tl) detectors for these experiments are that they are sensitive. The disadvantage is that these detectors exhibit poor resolution. However some spectral information can be obtained using these detectors. The experiment ran from July 10 to August 18. In this experiment, the Pd was plated out onto the Ni screen using a current of -1 mA. Figure 3.6-10 summarizes the detector count rate as a function of time. The background level is indicated. When electrolysis is occurring, an increase in count rate was observed. The same was observed in earlier experiments that were monitored using a small HPGe detector.[12] The times at which current changes, addition of D_2O, heater pulses, and laser illumination of the cathode are indicated. It can be seen that the gamma/X-ray emissions do not correlate with either changes in cell current, laser excitation of the cathode, addition of D_2O, or heating of the cell. Furthermore, comparing the bubble counts, Figure 3.6-8, and NaI counts, Figure 3.6-10, as a function of time, it can be seen that the two sets of events do not correlate with one another.

After ten days of electroplating (on 7-19), the NaI count rate peaked near 300 cps, Figure 3.6-10, and a fairly sharp peak (for NaI), at channel number 160 (~ 240 keV), appeared in the NaI spectrum, Figure 3.6-11a. This peak disappeared the next day. When the plating had completed on 7-21, the current was increased to -100 mA and the superwave charging profile was applied. The count rate was observed to decrease, Figure 3.6-10. No new peaks appeared in the spectrum until 8-3 at which time the current was increased to -200 mA (superwave charging profile), Figure 3.6-11b. The new peak appeared at channel number ~1700 (~ 2670 keV). This activity was observed to die out and the count rate dropped back down to background levels, Figure 3.6-10.

When the current was increased to -500 mA (superwave charging profile) on 8-11, the count rate began to increase, Figure 3.6-10, and peaks at high energy appeared in the spectrum, Figure 3.6-11c. The activity died out when the current was changed to -600 mA (superwave) on 8-13, Figure 3.6-11c.

On 8-13, electrolysis was terminated. Bursts of gamma rays occurred, Figure 3.6-10. On 8-14, the spectrum shows two new broad peaks at channels 1050 (~1650 keV) and 1200 (~1900 keV), Figure 3.6-11d. Later on 8-14, those peaks had decayed and a new peak at channel 1100 (~ 1730 keV) appeared, Figure 3.6-11d. By 8-15, those peaks decayed away, Figure 3.6-11d. By 8-18, the count rate had dropped back down to background levels, Figure 3.6-10.

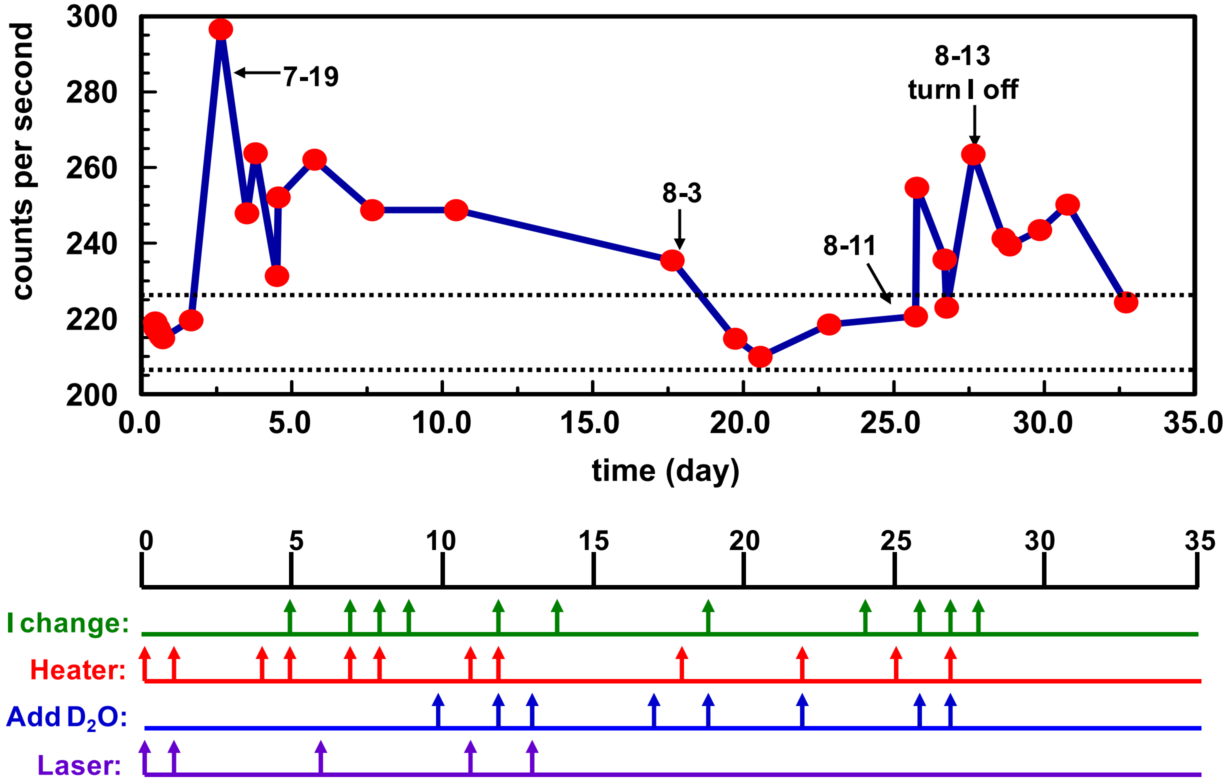

Figure 3.6-10. NaI count rate a function of time. Dates are indicated. The dashed lines between 205 and 225 cps represent the background count rate. Current changes, heater pulses, addition of D_2O, and HeNe laser illumination of the cathode are indicated. Dates are indicated where spectral data will be shown in Figure 3.6-11.

Given the broadness of the peaks, it is difficult to determine the identity of the species responsible for their existence. However, this broadness may be indicative of bremstrahlung radiation from beta decay within the detector. Other than gamma rays, only neutrons would be able to pass through the Al wall of the detector and activate, by neutron capture, various elements within the detector. Figure 3.6-10 may indicate both neutron capture with a beta decay (peak at 8-13 turnoff) with a second radioisotope that then also beta decays (2^{nd} peak on day 31).

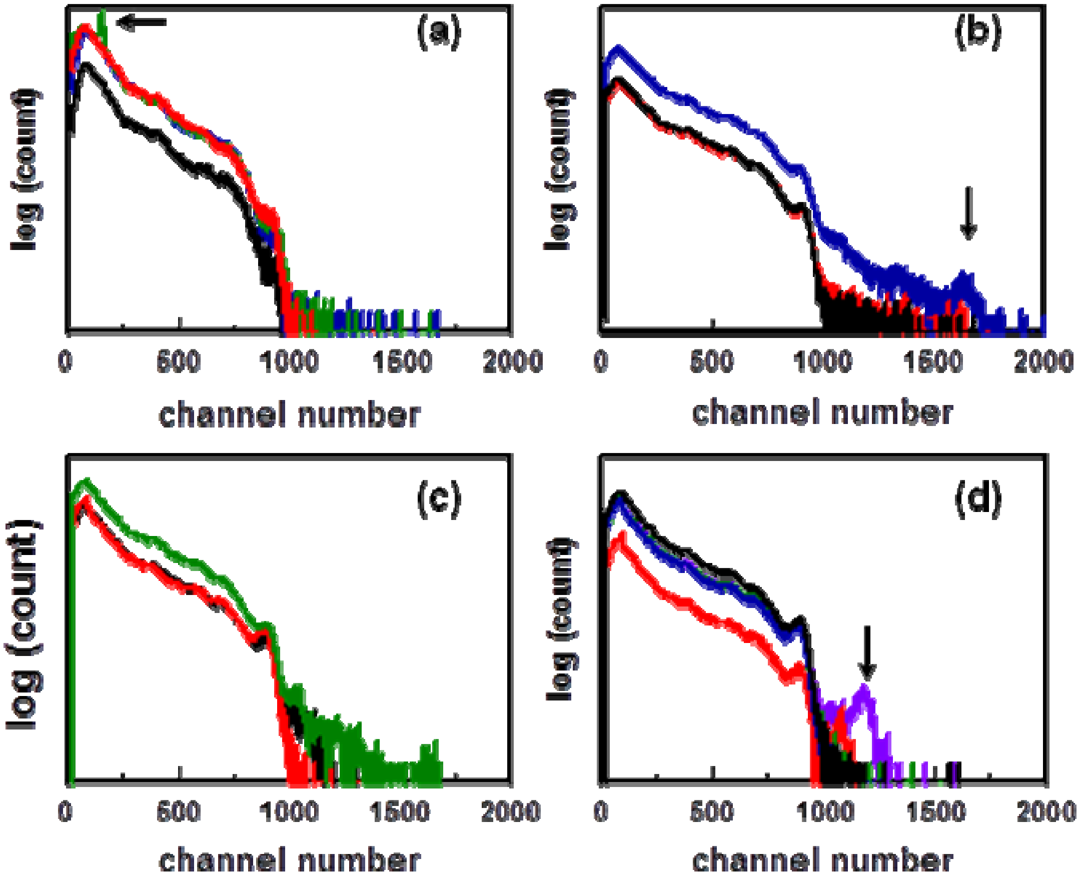

Figure 3.6-11. NaI spectra. The date the spectrum was obtained and acquisition time in seconds are indicated: (a) black = 7-17 @ 1103 (10000 s), blue = 7-18 @ 1120 (36000 s), green = 7-19 @ 1433 (36000 s), and red = 7-20 @ 1124 (36000 s); (b) blue = 8-3 (821732 s), red = 8-5 (174755 s), and black = 8-8 (191273 s); (c) green = 8-11 (239979 s), black = 8-12 (72391 s), and red = 8-13 (77159 s); and (d) purple = 8-14 @ 1452 (84324 s), red = 8-14 @ 2036 (16285 s), green = 8-15 @ 1934 (81840 s), blue = 8-16 @ 1753 (76700 s), and black = 8-18 @ 1629 (142918 s).

3.7 Thermal Measurements

3.7.1 SEM evidence of localized melting of the Pd cathode

The Pd formed as a result of Pd/D co-deposition is black and powdery. A scanning electron microscope (SEM) image of the deposit prepared by the Pd/D co-deposition process is shown in Figure 3.7-1a. The deposit has a highly expanded surface consisting of small spherical nodules. As discussed *vide supra*, because of the expanding electrode surface created as a result of Pd/D co-deposition, non-steady state conditions are assured. In an experiment using Ni screen as the substrate for a Pd/D co-deposition experiment, a thermal runaway occurred. The electrolyte completely boiled away. A silver Pd film was observed on the cell wall adjacent to the Ni screen and on the sides of the cell. SEM analysis of this silver film was done, An SEM image is shown in Figure 3.7-1b. The metallurgist doing the analysis indicated that the observed features of the film were consistent with metal that had melted under water. The melting point of bulk palladium is 1554.9 °C.

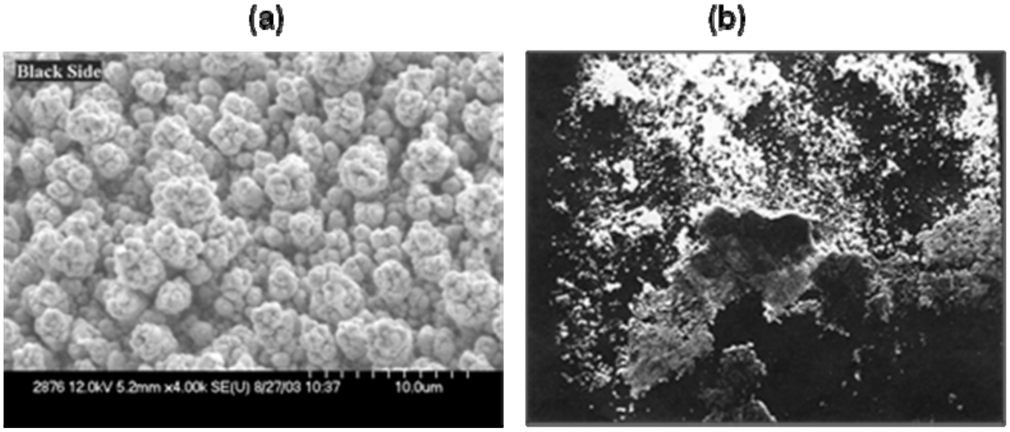

Figure 3.7-1. SEM images obtained for (a) Pd deposit formed as a result of Pd/D co-deposition and (b) Pd deposit that was splattered on the thin acrylic window.

Additional features suggestive of localized melting have been observed in the Pd deposit formed as a result of Pd/D co-deposition, Figure 3.7-2a, b, and c. The morphology of the deposit in Figure 3.7-2b is characteristic of molten lava under water. The Pd/D co-deposition images are very similar to the SEM images obtained for metals that have undergone laser ablation, Figures 3.7-2 d and e. In laser ablation, the focused laser beam causes volatilization of the metal. In both the Pd/D co-deposition images, Figures 3.7-2 a-c, and the laser ablation images, Figures 3.7-2 d and e, craters are observed with rounded, globular edges.

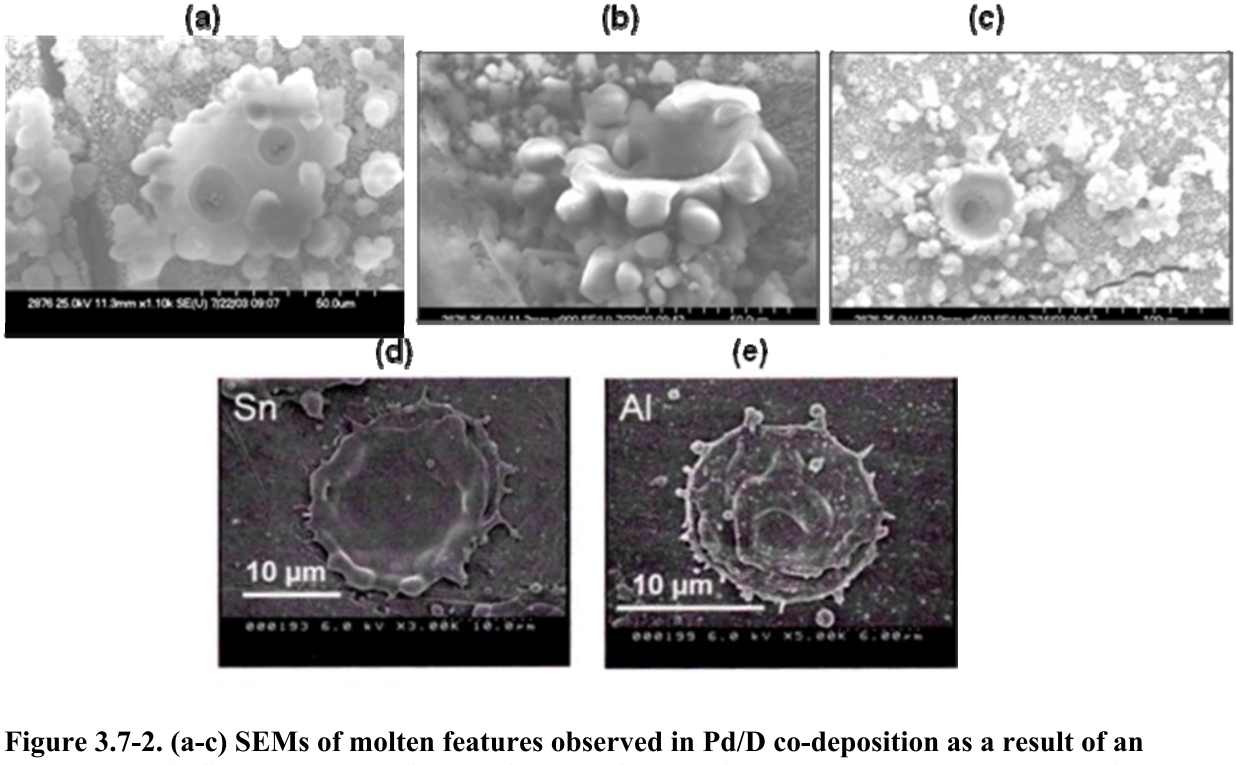

Figure 3.7-2. (a-c) SEMs of molten features observed in Pd/D co-deposition as a result of an external electric field. (d) and (e) SEMs of molten features in metals created by laser ablation.

The morphological features observed in Figures 3.7-2 a-c are similar to damage that has been seen in materials such as californium which undergoes spontaneous nuclear fission. In californium, these eruptions result from large numbers of spontaneous fissions resulting in 'spike damage.'

The energy required to create the craters observed in Figures 3.7-2 a-c can be estimated. Figure 3.7-3a shows a Pd/D co-deposition crater with a diameter of 50 µm. A schematic of this crater is shown in Figure 3.7-3b. The radius (r) and conservatively estimated height (h) of the crater are both ~ 25 µm. The volume (V) of a cone is given by $V = (1/3)\ \pi\ r^2\ h$. Using this relationship, the volume of Pd ejected to create the crater is estimated to be 1.47×10^5 µm^3, or 1.47×10^{-10} cm^3.

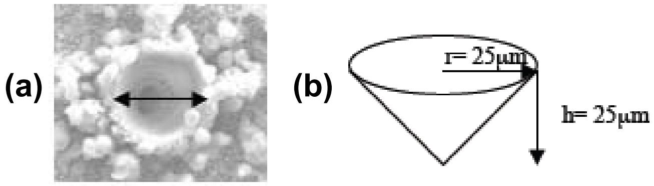

Figure 3.7-3. (a) SEM of crater seen in the Pd/D deposit. The crater has a diameter of 50 µm. (b) Schematic of the crater shown in (a) where r is the radius and h is the height of the cone.

Table 3.7-1 tabulates some constants and conversion factors that were used to calculate the energy required to create the crater shown in Figure 3.7-3. The volume of Pd ejected to create the crater was estimated to be 1.47×10^{-10} cm^3. From the density of Pd, the mass of Pd ejected to create the crater was calculated to be 1.8×10^{-9} g. This is equivalent to 1.6×10^{-7} moles of Pd. Using the heat of vaporization for Pd, the amount of energy required to vaporize the Pd to create the crater is 5.8×10^{-2} Joules.

Table 3 .7-1. Constants used to calculate crater energetics.

Pd solid density	12.02 g cm^{-3}
Pd melting point	1554.9 °C
Pd boiling point	3140 °C
Pd molecular weight	105.6 g mol^{-1}
Pd heat of vaporization	357 kJ mol^{-1} or 3.57×10^5 J mol^{-1}
Unit conversion factors	1 cm^3 = 10^{15} µm^3 1 MeV = 1.6×10^{-13} Joules

The number of nuclear fusion reactions needed to create the crater shown in Figure 3.7-3 can now be estimated. In this calculation, it is assumed that the heat is generated by conventional DD/DT fusion reactions, with a 50% branching ratio. Table 3.7-2 summarizes these hot plasma fusion primary and secondary reactions.

Table 3.7-2 Hot plasma fusion primary and secondary reactions.

(1i) $^{2}D_{1} + {}^{2}D_{1} \rightarrow {}^{3}T_{1}$ (1.01 MeV) + p^{+} (3.02 MeV) 50%
(1ii) $\rightarrow {}^{3}He_{2}$ (0.82 MeV) + n_{0} (2.45 MeV) 50%
(2) $^{2}D_{1} + {}^{3}T_{1} \rightarrow {}^{4}He_{2}$ (3.5 MeV) + n_{0} (14.1 MeV)
(3) $^{2}D_{1} + {}^{3}He_{2} \rightarrow {}^{4}He_{2}$ (3.6 MeV) + p+ (14.7 MeV)

The combined average energy of both primary and secondary DD/DT reactions is about 23 MeV, in both neutron and charged particle products. However, reactions 1i and the secondary, 2, result in 60% of the energy in neutron momentum, that won't heat the immediate vicinity. In contrast, reactions 1ii and the secondary, 3, have only 11% of the energy "lost" to neutron. In these calculations, we will use an average total charged particle energy of 20 MeV available for local heating, or 3.2×10^{-12} J/reaction. The energy required to create the crater in Figure 3.7-3 was estimated to be 5.8×10^{-2} J. Thus it took 1.8×10^{10} nuclear fusion reactions to create a single crater. Yet, this number of fusion reactions, to create a single crater, exceeds the total number of charged particle and neutron recoil tracks observed over the entire surface of a CR-39 detector used in a Pd/D co-deposition experiment.

Consequently, from these calculations, we can conclude the following:

(1) that the observed charged particles and neutrons do not correlate with heat
(2) that another reaction is primarily responsible for the heat generated
(3) that the reaction responsible for the heat is aneutronic.

3.7.2 Evidence that cathode is the heat source

Figure 3.7-4a shows a schematic of a two chamber cell which was used in a Pd/D co-deposition experiment. The Au wire cathode is wrapped around a thermocouple. As shown in Figure 3.7-4a, the Au cathode is in contact with a CR-39 detector. Another thermocouple is in contact with the Pt anode. Figure 3.7-4b shows the temperature measurements of the anode and cathode at an applied current of -100 mA. It can be seen that the thermocouple in contact with the cathode registers a temperature that is ~1.7°C higher than that registered at the anode. At time ~80 min, the cell dropped onto the lab bench, which resulted in knocking the Pd deposit off the Au wire. When this happened, the temperature of the cathode decreased and was approximately that of the anode, Figure 3.7-4b. These results indicate that the cathode is the heat source, which is in agreement with earlier reported infrared imaging results.[11]

In this two-chamber cell experiment, a CR-39 detector was in contact with the cathode, as shown in Figure 3.7-4a. Upon termination of the experiment, the detector was etched an examined under a microscope. Figure 3.7-5a and b show tracks observed at 500x magnification on the front and back surfaces, respectively. Figure 3.7-5c and d shows images obtained at 1000x magnification at different focusing depths. The tracks are similar to those discussed *vide supra*. A triple track, indicative of ≥ 9.6 MeV neutrons, was observed.

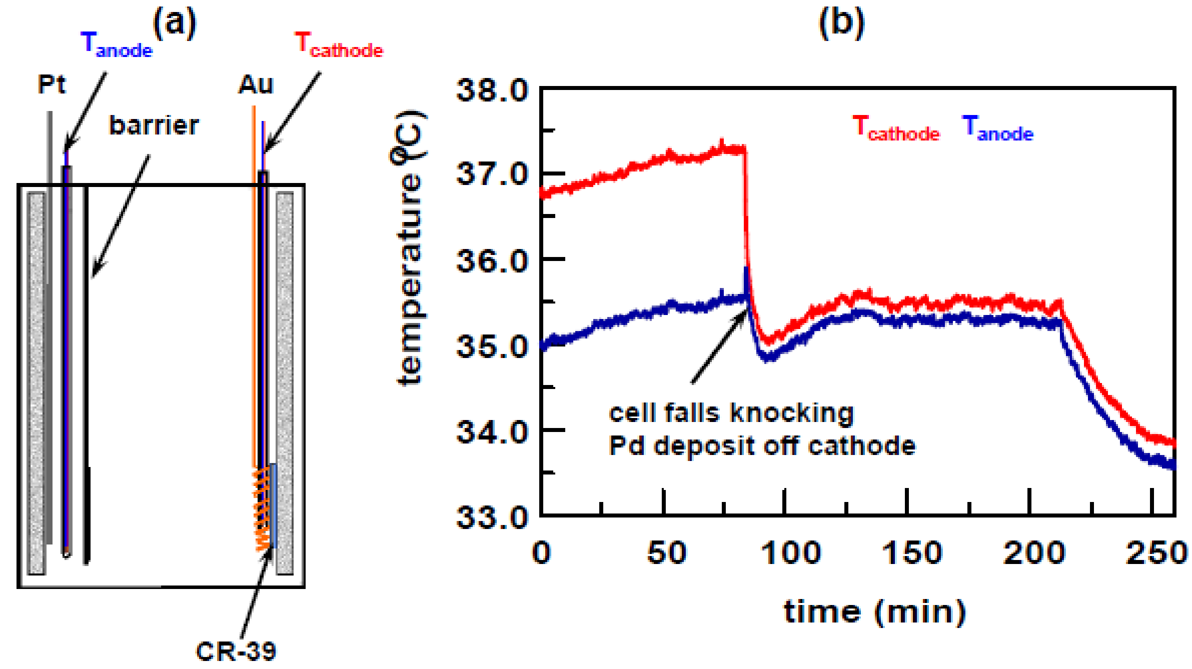

Figure 3.7-4. (a) Schematic of a two chamber cell used for thermal measurements. (b) Plots of the cathode and anode temperatures as a function of time. The time at which the cell fell, knocking off the Pd deposit, is indicated.

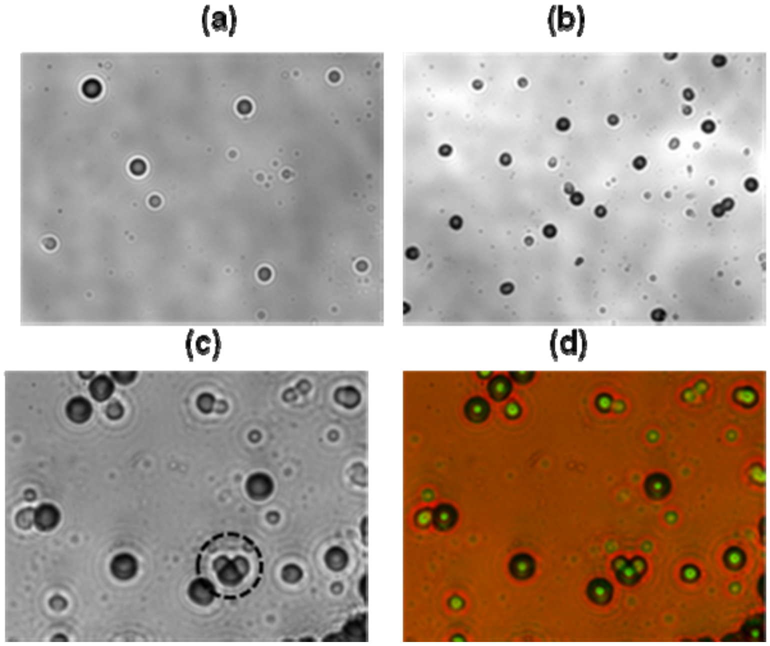

Figure 3.7-5. Microphotographs of tracks observed in the CR-39 detector used in the two-chamber cell shown in Figure 3.7-4a. (a) and (b) were obtained at 500x magnification for the front and back surfaces, respectively. (c) and (d) were obtained on the front surface at 1000x magnification where (c) was obtained with the microscope optics focused on the surface of the detector and (d) is an overlay of two images taken on the surface and the bottom of the tracks. A triple track, indicative of ≥ 9.6 MeV neutrons, is circled in (c).

3.7.3 Uranyl nitrate as an additive in Pd/D co-deposition

In 2003, Cravens and Letts[57] reported on using uranium and other chemicals as additives to trigger heat production in their Pd/D co-deposition experiments. The rational for the use of chemical additives is that there needs to be a gradient in the deuterium's chemical potential for the production of excess power. Their results indicated that the effect requires the deuterium flux to transverse between energy levels before the onset of the excess heat phenomena. They found that additives that have strong magnetic properties or elements with quadrupole moments seem to be beneficial in triggering the excess power events.

In this investigation, uranyl nitrate was used as an additive in a Pd/D co-deposition experiment. Figure 3.7-6a shows a photograph of the glass cell used in the experiment. Co-deposition was done on a Au wire that was wrapped around a thermistor. A concentric geometry, *i.e.*, the cathode is in the center of the anode, was used in this experiment. Figure 3.7-6b is a schematic that shows the placement of two solution thermistors as well as the cathode thermistor. One solution thermistor is between the cathode and the anode and the temperature registered by this thermistor is referred to as T_{inner}. The other solution thermistor is between the anode and the cell wall and the temperature registered by this thermistor is referred to as T_{outer}.

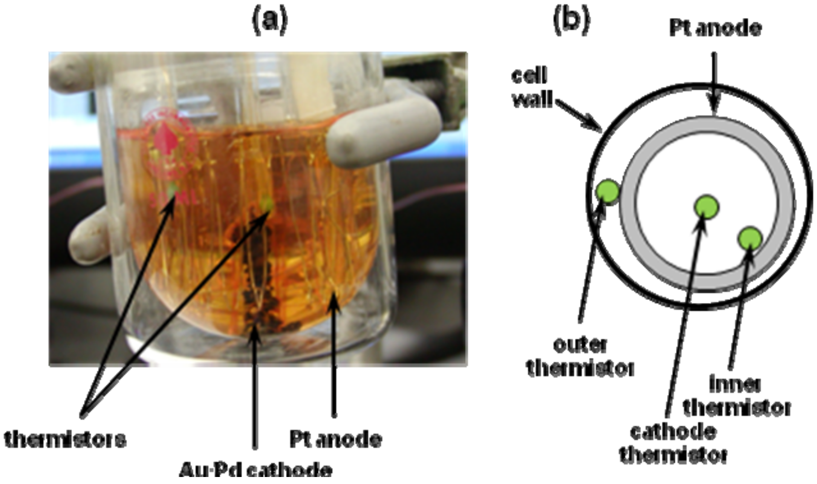

Figure 3.7-6 (a) Photograph of the glass cell used in the Au/Pd/D co-deposition experiment using uranyl nitrate as a chemical additive. (b) Schematic (bottom view) of the cell showing the placement of the thermistors and Pt anode.

In this experiment, two charging profiles were used after the Pd had plated out – constant current (DC) and superwave (SW).[66] Figure 3.7-7a shows a screen dump of the LabView program GUI showing the superwave used in the experiment. The superwave causes high D flux inside the Pd lattice. Results of DC and SW charging are summarized in Figure 3.7-7b. The results summarized in Figure 3.7-7b shows that the cathode is hotter than the solution which indicates that the cathode is the heat source. The results also show that SW charging results in slightly higher temperatures.

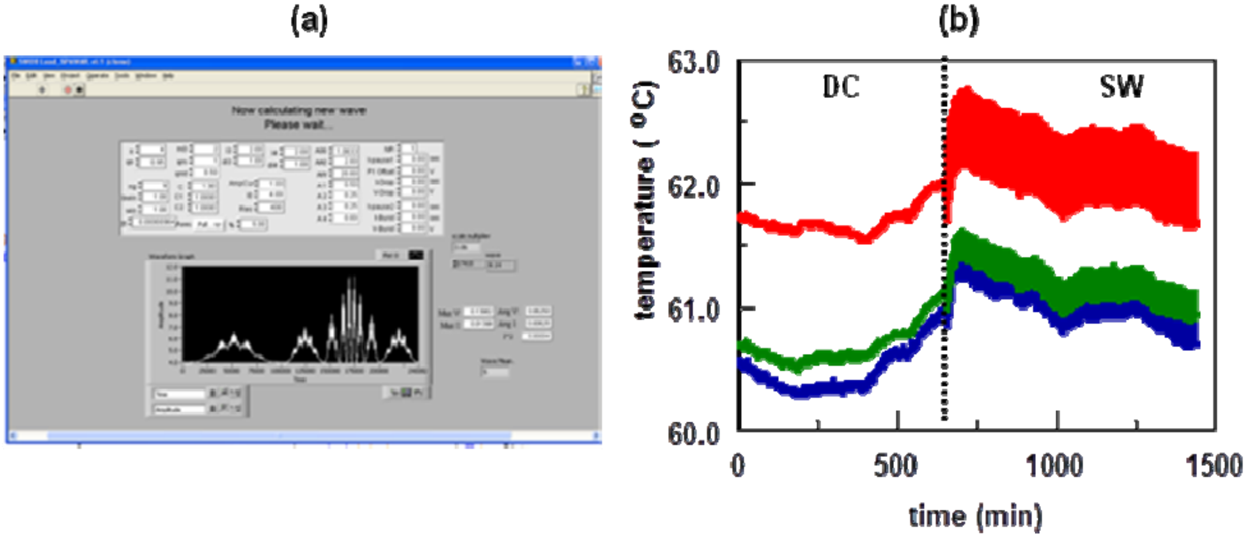

Figure 3.7-7. (a) Screen dump of the LabView GUI showing the superwave used in this experiment. (b) Results of -800 mA DC (average input power is 6.0 W) and -800 mA SW(average input power is 5.7 W) charging. Red = $T_{cathode}$, green = T_{outer}, and blue = T_{inner}

3.7.4 Heat after death (HAD)

In the 'Heat After Death' phenomenon, 'death' refers to the cessation of polarization, *i.e.*, the cell current is reduced to zero. In this effort, three experiments were conducted using the glass cell shown in Figure 3.7-6. In these experiments, the cell voltage was measured as well as the temperature of the cathode and two solution temperatures. One solution thermistor is between the cathode and the anode and the temperature registered by this thermistor is referred to as T_{inner}. The other solution thermistor is between the anode and the cell wall and the temperature registered by this thermistor is referred to as T_{outer}. The top graphs shown in Figure 3.7-8 are plots of ΔT as a function of time and the bottom graphs are plots of cell voltage as a function of time.

Figure 3.7-8a summarizes the results obtained for copper electroplating on a gold wire. This was a light water experiment. At an applied current of -200 mA, it can be seen that the cathode is hotter than the solution. The cell voltage is also very noisy. There was significant gas evolution and the bubbles act as a resistive layer between the cathode and the solution. When the current was turned off, the cell voltage dropped precipitously. A corresponding decrease in ΔT was also observed indicating that desorption of hydrogen from the copper surface is endothermic . When the current was terminated, little outgassing of the copper cathode was observed to occur. Figure 3.7-8b summarizes the results obtained for nickel electroplating on a Ni screen. This was also a light water experiment. At an applied current of -20 mA, the cathode was cooler than the surrounding solution. When the current was turned off, the cell voltage dropped. Like the Cu/H system, little outgassing of the cathode was observed. A decrease in ΔT was also observed indicating that desorption of hydrogen from the Ni surface is endothermic.

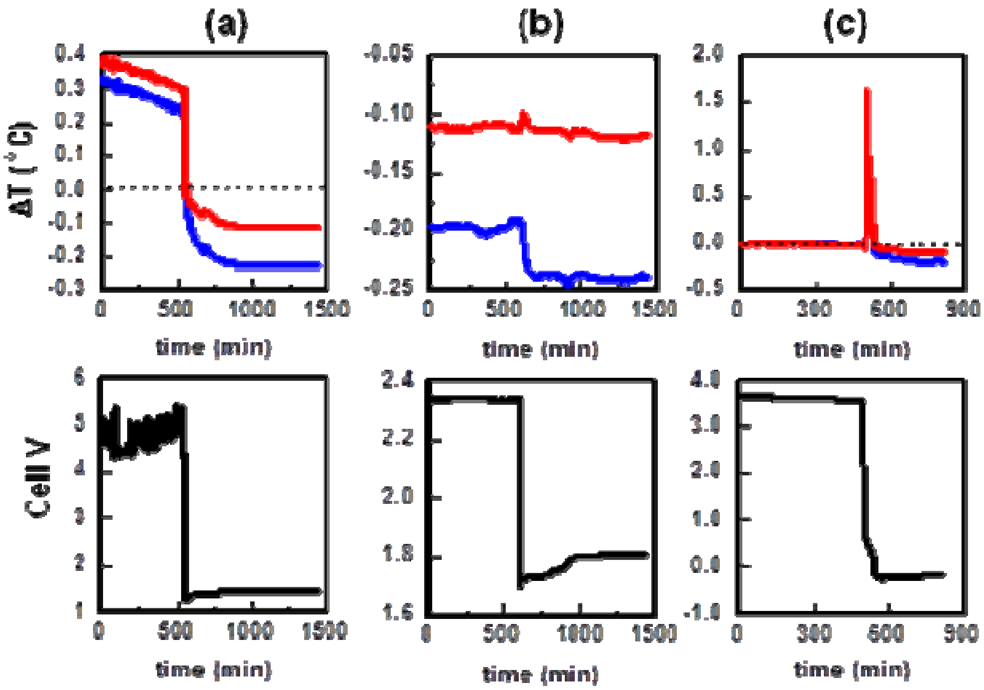

Figure 3.7-8. Experiments looking for evidence of HAD for (a) Cu/H co-deposition on Au wire for I = -200 mA to 0 mA, (b) Ni/H co-deposition on Ni screen for I = -20 mA to 0 mA, and (c) Pd/D co-deposition on Au wire for I = - 75 mA to 0 mA. Top graphs are plots of ΔT as a function of time where blue = $T_{cathode} - T_{outer}$ and red = $T_{cathode} - T_{inner}$. Bottom graphs are cell voltage as a function of time.

Figure 3.7-8c summarizes the results obtained for Pd/D co-deposition on a Au wire. At an applied current of -75 mA, the cathode and solution temperatures were equivalent. When the current was turned off, a HAD event was observed. Unlike the Ni/H and Cu/H systems, significant outgassing of the Pd cathode was observed. This indicates that, unlike the Ni and Cu deposits, the lattice of the Pd deposit loads with deuterium. Figure 3.7-9 shows expanded plots of ΔT vs. time and cell voltage vs. time during the HAD event. Measurements were taken every minute. For the first seven minutes after the cell current had been turned off, a decrease in ΔT was observed. Then ΔT increased. For ~31 minutes, the cathode stayed hotter than the solution.

The SSC-Pacific LENR program had been terminated before any light water experiments with palladium could be conducted. However, it is unlikely that the HAD event shown in Figure 3.7-9 is due to D_2/O_2 recombination. Past experience has show that no recombination occurs on Pd that is completely immersed in water.[14,67]

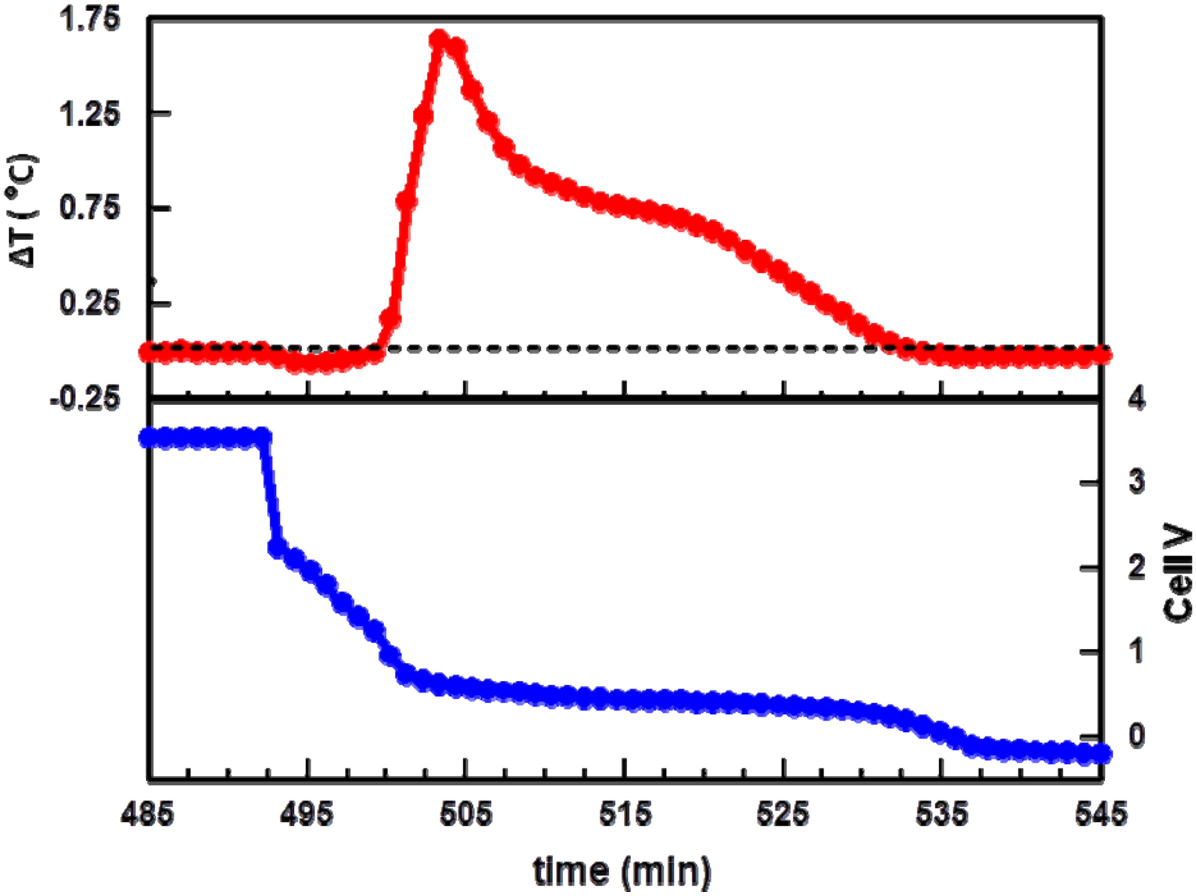

Figure 3.7-9. Expanded plots of (top) ΔT vs. time where ΔT = $T_{cathode} - T_{inner}$ and (bottom) cell voltage vs. time during the HAD event observed for the Au/Pd/D experiment. In the top plot, the dashed line represents a ΔT = 0 °C.

3.8 Preparation and Characterization of Stabilized Pd Foils and Nano-Deposits

3.8.1 Nanodeposit

Permanent ink was used to mask off the back side of a Ag foil and part of the front side. Only a 4 mm^2 square area was left open to plate Pd on. The Ag foil was placed in a quartz cuvette as well as a Pt anode and teflon-coated, magnetic micro stir bar. A solution of $PdCl_2$ and LiCl in D_2O was added and Pd was plated, under constant stirring, onto the bare 4 mm^2 square area on the Ag foil. The applied current was -0.1 mA. The resultant deposit was very dense. After the Pd had completely plated out, the Ag/Pd cathode was rinsed in water and soaked in isopropanol to remove the permanent ink. The cathode was again rinsed in water and allowed to dry. Once dried it was placed in the quartz cuvette (total volume 7.0 mL) along with the Pt anode and a solution of Li_2SO_4 in D_2O. Electrolysis was done to load the Pd with D. The applied current was -1 mA (for ~ 20 h), -2 mA (for ~ 23h), -5 mA (for ~24 h), -10 mA (for ~24h), -25 mA (for ~26h), -50 mA (for ~21h), and -75 mA (for ~72h). After 72 h and with an applied current of -75 mA, 200 μL of saturated Hg_2SO_4 in D_2O was added incrementally during a 24 h period. During electrolysis, Hg_2SO_4 reduces to metallic Hg, which is supposed to seal the deuterium inside the

Pd lattice. This is how Tripoldi *et al.*[20] stabilize their highly loaded Pd/H(D) samples prior to superconductivity measurements. Afterwards the cell was turned off and subjected to analysis using an SEM-EDX. The results are summarized in Figures 3.8-1 through 3.8-3.

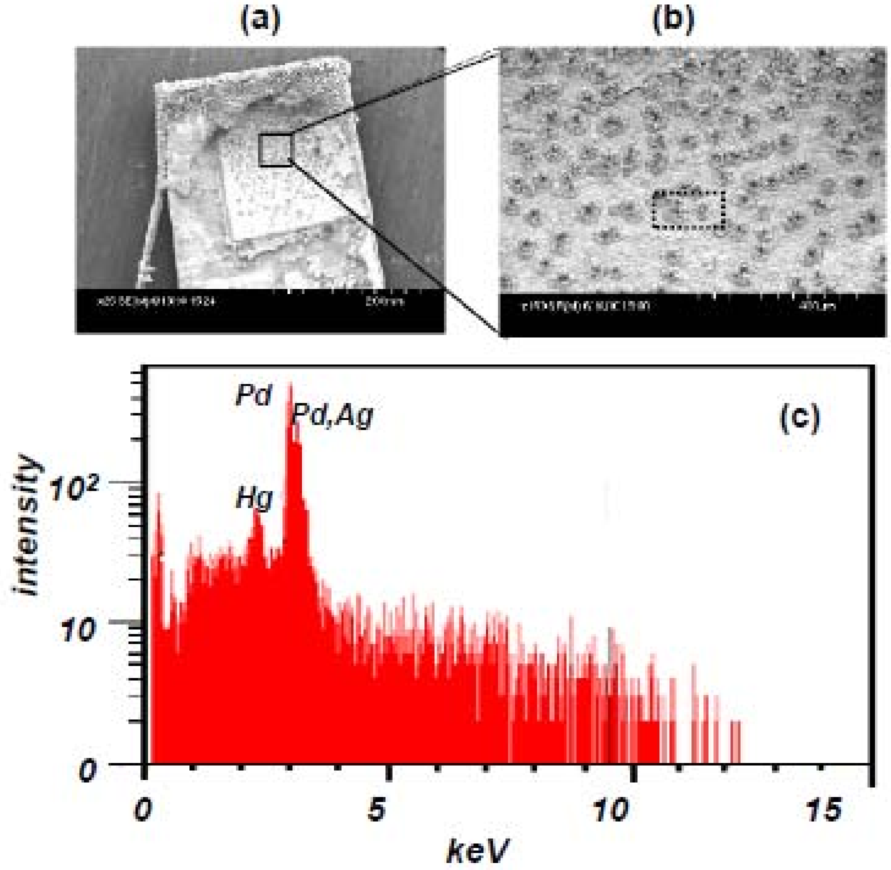

Figure 3.8-1. SEM-EDX analysis of the 'stabilized' Pd nanodeposit on Ag foil. (a) 4 mm^2 square of Pd on Ag foil. (b) SEM and (c) EDX analyses of the area indicated in (a).

Figure 3.8-1a shows an SEM of the Ag foil. It can be seen that most of the Pd did indeed plate out in the unmasked area of the Ag foil. The area inside the Pd deposit was viewed at higher magnification. The SEM of this area is shown in Figure 3.8-1b. It can be seen that the Pd deposit is dense with huge 'barnacle' like features on the surface. Figure 3.8-1c is an EDX of the region indicated in Figure 3.8-1a. The peaks due to Pd and Ag are indicated as is the peak due to Hg. The EDX spectrum shows that the mercurous ions did reduce into metallic Hg on the surface of the cathode. No other peaks due to other species are present.

Figure 3.8-2a shows an SEM of the 'barnacle'-like features at higher magnification. The area magnified is indicated in Figure 3.8-1b. These 'barnacle' like features do not resemble the molten-like features shown in Figure 3.7-2. Instead, these features look like volcano craters formed when hot gases explode through the earth surface during volcanic eruptions. Therefore, the 'barnacle' like features shown in Figure 3.8-2a formed when the deuterium outgassed from inside the Pd lattice. These results indicate that the Pd/Hg deposit does not have the structural integrity to contain the deuterium. The results also indicate that, contrary to the assertions of some LENR researchers, the Pd lattice of the nanodeposits formed as a result of Pd/D co-deposition do indeed load with deuterium. This was also shown by the outgassing observed for the Pd deposit as discussed *vide supra*.

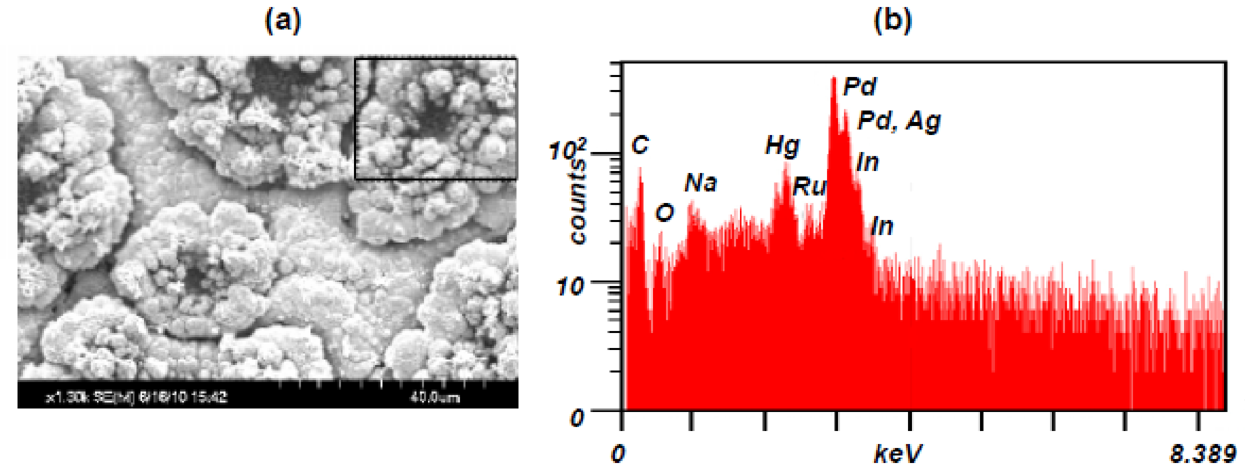

Figure 3.8-2. (a) SEM and (b) EDX analyses of the region indicated in Figure 3.8-1b.

Figure 3.8-2b shows an EDX of the barnacles shown in Figure 3.8-2a. Besides peaks due to Pd, Ag, and Hg, additional peaks due to Na, In, and Ru were observed. These species were not observed in the EDX of the larger area, Figure 3.8-1c. This indicates that the Na, In, and Ru are not homogeneously distributed over the surface of the cathode and that these new species are associated with barnacle itself. EDX detection limits are on the order of 0.1%.[68] Given the insensitivity of the EDX technique, the inhomogeneous distribution of the new elements, the fact that the experiment was done using a quartz cuvette, and the small volume of solution used in the course of this experiment (~10 mL), these new elements cannot be due to contamination.

Figure 3.8-3a shows an SEM of a barnacle at higher magnification. There appears to be dendrites inside the barnacle. These dendrites are shown at even higher magnification in Figure 3.8-3b. In addition to dendrites, small spherical features with spikes on the surface are seen. An EDX of the material inside the barnacle is shown in Figure 3.8-3c. Besides Pd, a peak due to Al is observed. No Al was seen on the surface of the deposit. Under these experimental conditions, Al cannot be electrochemically plated out from an aqueous solution onto a cathode. It is therefore unlikely that this Al is the result of contamination.

As discussed *vide supra*, the barnacles resemble the crater of a volcano. Craters are formed when hot, subsurface gases and magma are released during a volcanic eruption. Likewise, the barnacles resulted when the deuterium inside the Pd lattice was released explosively. The resultant deuterium flux inside the lattice was therefore high. Two criteria for the initiation of LENR are high D/Pd loadings and high D flux inside the lattice. The barnacle features seen in the SEMs, Figures 3.8-1 and 3.8-2, indicate that both criteria were met. The EDX results, Figures 3.8-2b and 3.8-3c, showing the presence of new elements associated with the barnacles indicate that LENR transmutations had occurred.

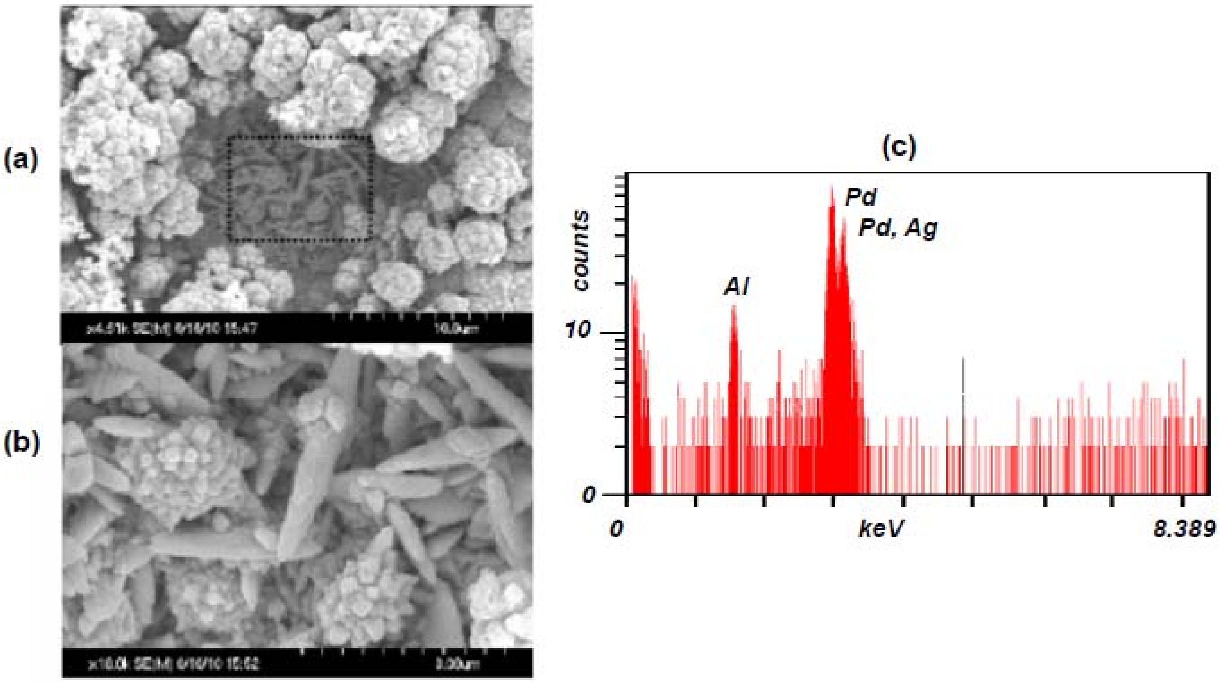

Figure 3.8-3. (a) SEM of the region indicated in Figure 3.8-2a. (b) SEM and (c) EDX analyses of the region indicated in Figure 3.8-3b.

3.8.2 Compression experiment of a stabilized Pd/D foil

A schematic of the cathode used to prepare a stabilized Pd/D foil is shown in Figure 3.8-4a. A 250 µm diameter Ag wire was wrapped around a 25 µm thick, 1 cm^2 Pd foil. To hold the Ag wire in place and provide Ohmic contact to the Pd foil, polyethylene heat shrink was used as shown in Figure 3.8-4a. The cathode was placed inside a quartz cuvette with a Pt anode. A solution containing Li_2SO_4 in D_2O was added to the cell. The Pd foil was then electrolytically loaded with deuterium. The applied current was -10 mA (for ~22 h), -20 mA (for ~8h), -30 mA (for ~18 h), -50 mA(~72 h), -75 mA (~23 h), -100 mA (~24 h), +10 mA (for ~20 min), -100 mA (for ~24 h), +10 mA (for ~20 min), -100 mA (for ~24 h), +10 mA (for ~20 min), -100 mA (for ~24 h), -125 mA (for ~24 h), and -150 mA (~48 h). Afterwards, 500 µL of saturated Hg_2SO_4 in D_2O was added incrementally during a 7 day period to stabilize the D-loaded Pd foil.

The stabilized Pd/D foil was then taken to LANL and was used in a compression experiment. A schematic of the experimental setup is shown in Figure 3.8-4b. In this experiment, the stabilized Pd/D foil was placed on a Cu block. A HE cartridge was placed on top of the stabilized Pd/D foil. This experimental configuration assures maximum compression of the Pd/D foil.

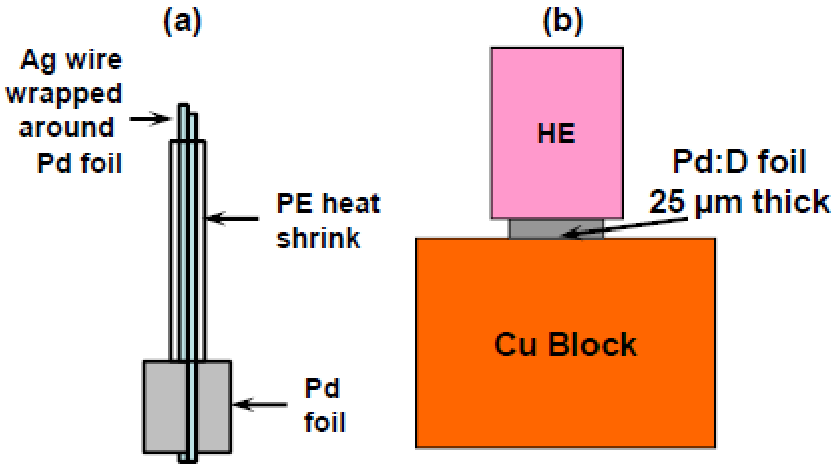

Figure 3.8-4. (a) Schematic of the cathode used to prepare a stabilized Pd/D foil. (b) Schematic of the compression experiment done at LANL.

The results obtained after the HE was detonated are summarized in Figure 3.8-5. Figures 3.8-5a-c show the Cu block after detonation of the HE. A large circular crater is observed. The crater is almost completely symmetric, except for the extra divot observed on the side of the Cu block, indicated by arrows in Figures 3.8-5 a and b. In Figure 3.8-5b, a ridge can be observed around the divot. A latex cast of the crater in the Cu block was made. Photographs of the latex cast are shown in Figure 3.8-6. The divot is circled. It is possible that this divot may have been created by the energy released upon compression of the Pd/D foil. Figure 3.8-5d shows the resultant neutron pulse that was measured using a solid state scintillation detector. This neutron pulse indicates that compression of deuteria inside the Pd lattice occurred.

Other attempts to replicate this experiment failed. One reason may be due to the fact that this particular foil was the only one loaded using Li_2SO_4 as the supporting electrolyte. The other foils were loaded in electrolytes using $SrSO_4$ as the supporting electrolyte. Lithium can enter the Pd lattice. Strontium cannot. This was also the only foil that did not have additional wires spot welded to it to measure the deuterium loading of the stabilized foil. In those other experiments, four Pt wires (250 µm in diameter) were spot-welded to the 25 µm thick foils so that the deuterium loading could be measured. When the foils were taken to LANL, attempts to measure the deuterium loading resulted in one or more of the wires breaking off the foil with subsequent deloading of the deuterium. Also the presence of the remaining wires on the foil could have negatively impacted the geometry of the compression wave.

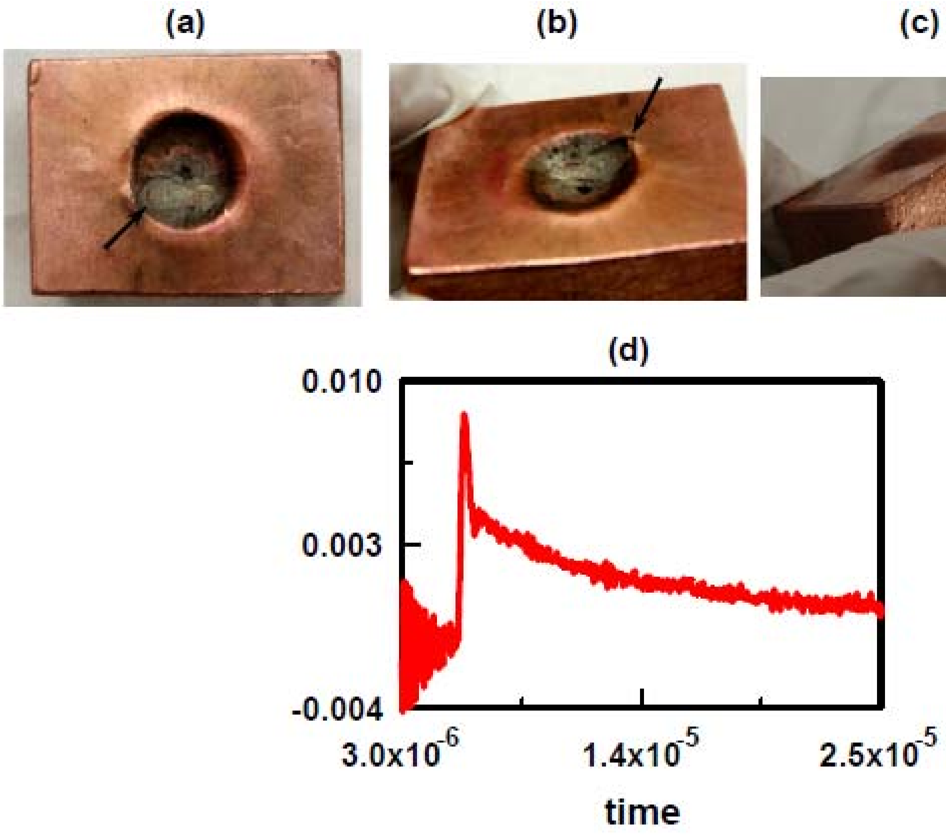

Figure 3.8-5(a)-(c) Photographs of the Cu block used in the compression experiment. The arrows in (a) and (b) indicates an additional divot inside the block. (d) The measured neutron pulse produced as a result of the neutron pulse.

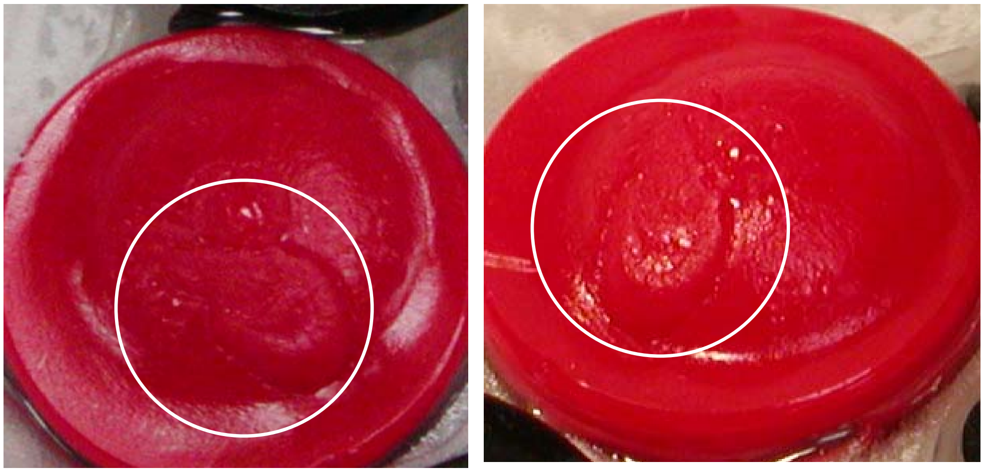

Figure 3.8-6. Photographs of the latex cast of the crater in the Cu block shown in Figure 3.8-5 a-c. The divot is circled.

4.0 COMMERCIAL AND MILITARY VALUE OF THE TECHNOLOGY UPON MATURATION

Once understood, LENR has the potential to be a paradigm-shifting, 'game-changing' technology. Nuclear energy systems have power densities six orders of magnitude greater than chemically-based energy generation or storage systems. The ability to harness a new nuclear energy source for either thermal or electrical conversion, without the generation of penetrating energetic particles, would have a profound commercial and military impact ranging from small footprint power systems to mobile systems to larger stationary power systems. Depending on how the technology scales, it could be used as a power source for expeditionary warfare and military bases as well as surface ships/submarines; nuclear battery for autonomous C4I operations (communications, computers, satellites); and long duration UAV and USV ops (propulsion). Such a technology would have a profound effect upon one of the U.S. and DoD's largest financial and environmental costs: burning hydrocarbons from imported oil and gas with their attendant CO_2 footprint. Indeed, many U.S. military actions this century, and the most costly in the 1990's, have been driven by, or consequences of, the geopolitics of oil. Decreasing the use of foreign oil would result in both an energy savings and a reduction in US military presence, and fleet costs, in maintaining access to foreign oil and natural reserves.

The natural uranium witness material experiments suggest that LENR can be used to create a hybrid fusion-fast fission reactor. Fusion is neutron rich but energy poor while fission is neutron poor but energy rich. Figure 3-1 illustrates the concept of behind a hybrid reactor that combines rich fusion neutrons with rich fission energy. A hybrid fusion-fast fission system capable of fissioning fissile, or fertile, actinides has an impact on nuclear power systems and the remediation of nuclear waste. By using natural uranium, uranium enrichment is unnecessary, removing its economic, environmental, and energy costs. By using fast neutrons, plutonium is not bred, but is consumed. Consequently, there is the potential to burn spent nuclear fuel *in situ* with little or no reprocessing, removing both environmental and public health concerns, and limiting nuclear weapons proliferation. By burning existing nuclear waste, a major impediment to increased nuclear energy is removed. Other potential uses of LENR generated fast neutrons are the creation of radioactive isotopes that are used in medical diagnostics and treatments as well as geological and chemical tracers.

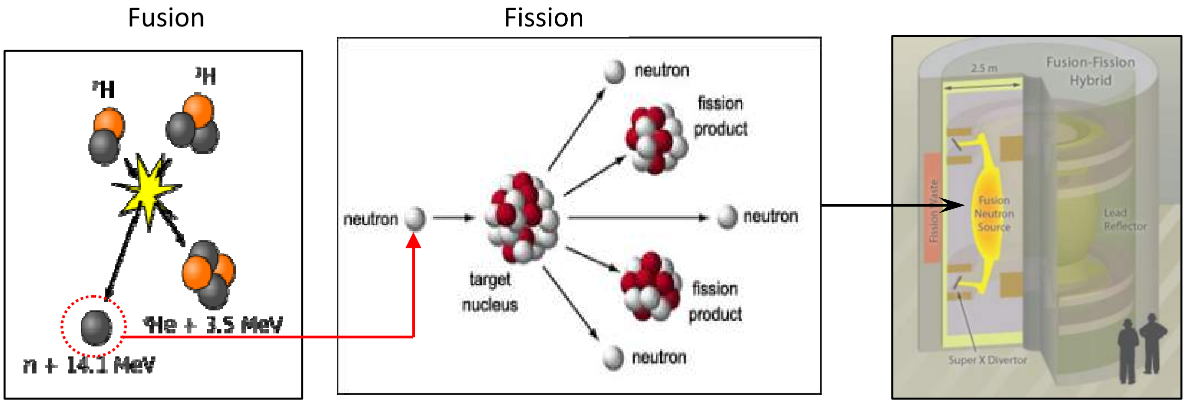

Figure 4-1. Hybrid fusion-fission reactor concept: Pd/D generated 14.1 MeV neutrons are used to fission ^{238}U and actinides present in spent fuel rods thereby eliminating nuclear waste while creating much needed energy without the production of greenhouse gases

A near-room temperature superconductor has applications on both small scales, in computing and antenna component design, and on larger scales in medical magnetic resonance imaging and in loss-less power transmission. These applications are based upon combinations of high strength magnetic fields, low thermal noise, and zero resistance conductance of electricity. Currently, these superconductor uses are compromised by the necessity to cool the superconductor components to either liquid nitrogen (77 K) or liquid helium (4 K) temperatures. Indeed, except under extraordinary circumstances, the cooling infrastructure outweighs the benefits of a superconducting system. However, a near-room temperature superconductor would give rise to entire new industries based on the ability to build highly efficient electrical motors and superior magnets, low noise circuits, and the ability to transmit power long distances without losses.

5.0 CONCLUSIONS

The 23 years of LENR research at SSC Pacific has resulted in 33 publications, 42 presentations/posters/conference proceedings, three technical reports, and one patent. A complete bibliography can be found in Appendix I. Publications and presentations that are relevent, or resulted from, the DTRA funded effort are included in Appendices II and III, respectively. Between 2005 and 2009, videos of SSC-Pacific LENR representations and experiments have been made and posted in the internet. These videos, along with their URL links, are summarized in Table 5-1.

Table 5-1. Summary of SSC-Pacific LENR videos on the internet.

DESCRIPTION	URL Link
2005 - U.S. Navy SPAWAR San Diego LENR (Cold Fusion) Research Lab: Infrared Measurements	http://www.youtube.com/watch?v=Pb9V_qFKf2M
2005 - U.S. Navy SPAWAR San Diego LENR (Cold Fusion) Research Lab: 2005 Site Visit	http://www.youtube.com/watch?v=U93AtjakNDc&feature=related
2005 - U.S. Navy SPAWAR San Diego LENR Research Lab	http://www.youtube.com/watch?v=tC45cDm66WU&feature=related
2007 - P. Mosier-Boss (SPAWAR) LENR Presentation at APS	http://www.youtube.com/watch?v=K1TXv0Ob8Bs&feature=related
2007 - Mr. Lawrence Forsley (JWK Technologies Inc.) LENR Presentation at APS	http://www.youtube.com/watch?v=VH9_42U0FLU
2008 - ICCF-14 #20.1 Frank Gordon -- LENR Research using Co-Deposition	http://www.youtube.com/watch?v=ZGKm0MVZ9Zw
2008 - ICCF-14 #20.3 Pamela Mosier-Boss -- LENR Research using Co-Deposition	http://www.youtube.com/watch?v=7KCc3FKLJco
2008 - ICCF-14 #20.4 Lawrence Forsley -- LENR Research using Co-Deposition	http://www.youtube.com/watch?v=USaM7bMOPnc
2008 - ICCF-14 #20.5-SPAWAR-JWK-Q&A	http://www.youtube.com/watch?v=M_32vY0uUx4
2009 - American Chemical Society Press Briefing	http://www.youtube.com/watch?v=EHc3jOTJYZA&feature=channel
2009 - KSL TV: Cold fusion makes a comeback	http://www.ksl.com/?nid=148&sid=5942381
2009: The Science Channel Videos: Brink: Evidence of Nuclear Fusion?	http://science.discovery.com/videos/brink-news-evidence-of-nuclear-fusion.html
Twenty-Year History of Lattice-Enabled Nuclear Reactions (LENR) - Hiding in Plain Sight	http://www.youtube.com/watch?v=VymhJCcNBBc
2009 - U.S. Navy SPAWAR San Diego LENR ("Cold Fusion") CR-39 Sequential Optical Analysis	http://www.youtube.com/watch?v=8uToLOOg1hI&feature=related
2009 - University of Missouri LENR Seminar - Dr. Frank Gordon	http://www.youtube.com/watch?v=ZyciIs53GfA&feature=related
2009 - University of Missouri LENR Seminar - Dr. Pamela Mosier Boss	http://www.youtube.com/watch?v=HbA6ZH8AiN4&feature=related
2009 - University of Missouri LENR Seminar - Mr. Larry Forsley	http://www.youtube.com/watch?v=m-oPfqXtHIM&feature=related

Taken all together, this is probably the largest, most comprehensive body of work in the LENR field. The work has received international attention. Three stories appeared in the UK international science magazine, New Scientist. All three stories were positive towards LENR. The first story, ‘Reasonable Doubt’ by Bennett Daviss, appeared on March 29, 2003. It covered the LENR work done by Szpak *et al.* at SSC-Pacific and Miles at Naval Air Weapons Station China Lake. Figure 5-1a shows a photograph of the issue’s cover page. The second story, ‘Cold Fusion Rides Again’ by Bennett Daviss, appeared on May 5, 2007 and covered the initial CR-39 results reported by SSC Pacific scientists at the 2007 spring ACS meeting in Chicago, IL. The cover page of this issue is shown in Figure 5-1b. The third story, ‘Neutron Tracks Revive Hopes for Cold Fusion’ by Collin Barras, appeared on March 28, 2009. This story summarized the triple track CR-39 data reported by SSC Pacific at the 2009 spring ACS meeting in Salt Lake City, UT. Figure 5-1c shows a triple track recorded on a CR-39 detector used in a Pd/D co-deposition experiment.

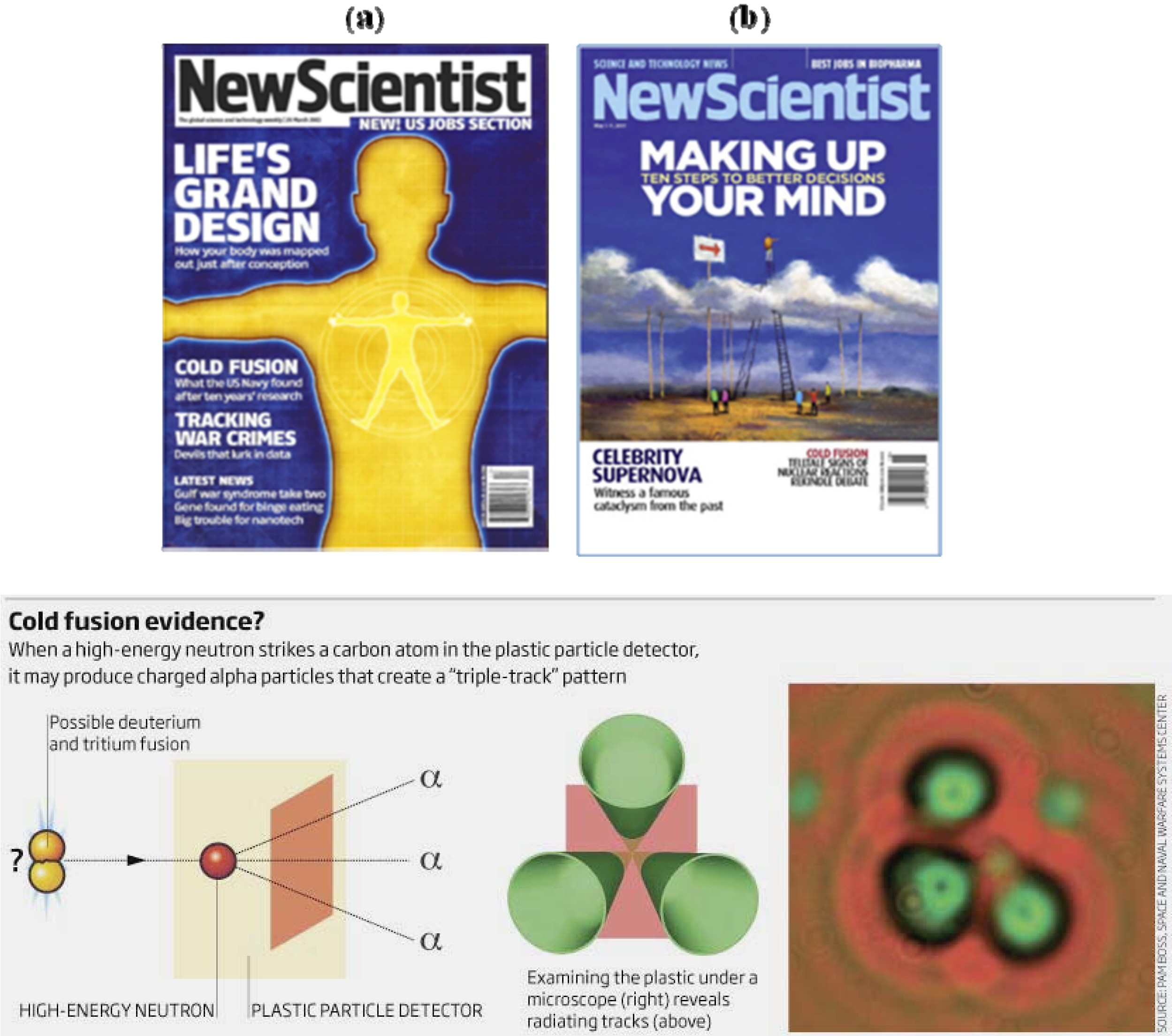

Figure 5-1. Cover pages of the New Scientist issues on (a) March 29, 2003 and (b) May 5, 2007. (c) Triple track shown in the March 28, 2009 New Scientist issue.

On Sept. 30, 2005, NPR's Living on Earth aired three reports on nuclear power. The first report, 'Some Like It Hot…,' focused on conventional hot fusion. The second report, 'Cold Fusion: A Heated History,' looked at the latest research in the field of cold fusion that included the work done at SSC Pacific. The third report, 'Pebble Bed Technology – Nuclear Promise or Peril?,' looked at the nuclear power plant being developed in South Africa. These reports on nuclear power won the 2006 AAAS Science Journalism Award. The Sept. 30, 2005 show and transcript can be accessed at http://www.loe.org/shows/shows.html?programID=05-P13-00039.

On the 20th anniversary of the Fleischmann-Pons press conference announcing that their electrochemical cells were producing more energy than could be accounted for by chemical means, Mosier-Boss reported on evidence of high energy neutrons at the American Chemical Society (ACS) Spring meeting. By happenstance, that meeting was held in Salt Lake City, UT. The ACS hosted a press conference. Mosier-Boss participated in this press conference, Figure 5-2a, and her statement can be found in Appendix I. The ACS press release was picked up by news agencies world-wide. These news agencies (including the San Diego Union Tribune), in turn, reported on the neutron results. Colin Barras of New Scientist contacted Dr. Johan Frenje at the Massachusetts Institute of Technology, DoE's expert at interpreting CR-39 tracks.[44] When shown microphotographs of the SSC-Pacific triple tracks, Frenje said, 'I must say that the data and their analysis seem to suggest that energetic neutrons have been produced.' On March 27, 2009, the Discovery Science Channel show Brink reported on the SSC-Pacific results in the story 'Evidence of Nuclear Fusion?,' Figure 5-2b.

Figure 5-2. Photographs of (a) the panel of participants of the 2009 ACS press conference and (b) the Brink story, 'Evidence of Nuclear Fusion?'

The Pd/D co-deposition generated tracks in CR-39 have also been shown in the cover of Current Science, Figure 5-3a. Current Science is published by the Current Science Association in collaboration with the Indian Academy of Sciences. According to the Current Science home page, ‘The journal is intended as a medium for communication and discussion of important issues that concern science and scientific activities. SSC-Pacific triple track images in CR-39 were shown on the cover of the ACS symposium book, Figure 5-3b. The ACS is the world’s largest scientific society.

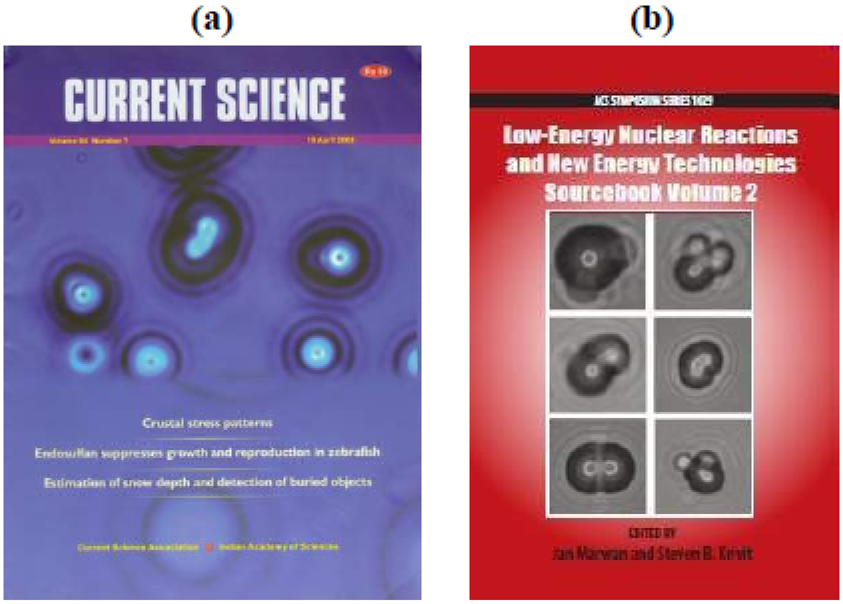
(a)

CURRENT SCIENCE

Crustal stress patterns

Endosulfan suppresses growth and reproduction in zebrafish

Estimation of snow depth and detection of buried objects

(b)

Low-Energy Nuclear Reactions
and New Energy Technologies
Sourcebook Volume 2

EDITED BY
Jan Marwan and Steven B. Krivit

Figure 5-3. Cover pages on (a) Apr. 7, 2008 Current Science and (b) 2010 ACS symposium book.

There are indications that the field of LENR is slowly gaining acceptance. The Environmental Division of ACS has hosted five New Energy Technologies symposia between 2007 and 2011 and published two symposium books. Katherine Sanderson of Nature reported on the March 2007 ACS symposium that was held in Chicago, IL. She reported that the program chair for the session (not a cold fusion scientist) was impressed by the results that were presented and was ‘keeping an open mind on the matter.’ As for herself, she said she was initially skeptical. After seeing the presentations, she indicated, ‘Cold fusion? I don’t know, but the evidence that something weird is happening is there. Maybe it’s time to think about this again...’

On March 26, 2012, Mosier-Boss and Forsley were invited by Dr. Michael Adams of Xavier University to speak at the ACS Undergraduates Technical Symposium on “Nuclear Power Generation – Lessons from Fukushima Daiichi and Future Directions.” These presentations are included in Appendix III.

On April 19, 2009, "60 MINUTES" aired a story on LENR, profiling the research done by the Israeli firm, Energetics Technologies LLC, as well as their collaborative work with SRI International and the Italian Energy Research Agency, ENEA. CBS had asked Dr. Robert Duncan, vice chancellor for research at the University of Missouri and an expert in low-temperature physics, to look into LENR. Duncan read some of the published papers and then met with researchers at the Energetics laboratory in Israel. Forsley brought to his attention the SPAWAR work and papers, that were briefly cited in the CBS transcript. Duncan was convinced that the excess heat effects were real. Forsley suggested a meeting of SPAWAR personnel and University Columbia faculty that became a University of Missouri hosted, and webcast, LENR symposium on May 30, 2009

In August 2009, SSC-Pacific hosted a LENR workshop. This resulted in DIA publishing a technology forecast paper on LENR that came out on November 13, 2009. A copy of this paper can be found in Appendix II. At the first ARPA-E Energy Innovation Summit in Washington DC in March, 2010, Dr. Vinod Khosla, an invited speaker, founder of Sun Microsystems and Khosla Ventures, mentioned LENR as a potential energy source in his keynote speech 'Innovation vs. Punditry: Escaping Conventional Thinking.'

Besides presenting results at conferences in APS, ACS, and ICCF, Pd/D co-deposition has been presented to a number of admirals and heads of government agencies. Table 5-2 summarizes these presentations.

The Pd/D co-deposition technique, pioneered by SSC-Pacific, is a robust, reliable and reproducible means of generating LENR in the Pd lattice. Heat effects using Pd/D co-deposition have been reproduced by Miles[10] as well as Cravens and Letts.[10,56] Bockris *et al.* reproduced the tritium results.[69] Besides SRI, the CR-39 results have been replicated by Dr. Winthrop Williams of the University of Berkeley, Dr. Ludwik Kowalski of Montclair University; Mr. Pierre Carbonnelle, l'Université catholique de Louvain and three groups of undergraduates from UCSD as part of their senior projects.

On November 2011, the LENR research at SSC-Pacific was terminated. The official reason given by SSC-Pacific's PAO, Jim Fallin, to Steve Krivit of New Energy Times for the termination the LENR work at SSC-Pacific is:

> "In response to your recent query," Fallin wrote, "while I won't discuss details of our internal decision-making processes, I will confirm SPAWAR plans no further low-energy nuclear reaction (LENR) research. There are other organizations within the federal government that are better aligned to continue research regarding nuclear power. We have taken initial steps to determine how a transition of low-energy nuclear reaction (LENR) research might occur."

The implications of this statement are that both SPAWAR HQ and SSC-Pacific say that the phenomenon is real and that it is nuclear in nature.

Table 5-2. List of presentations to admirals and heads of government agencies.

DATE	MEETING PLACE/ PERSON(S) BRIEFED
Aug. 2, 2006	NDIA Naval S&T Partnership Conference in Washington DC: RADM William E. Landay III (head of ONR), Dr. Mike McGrath (head of S&T at ASN, RDA), Lt. Gen. Lawrence P. Farrell Jr. (USAF, retired)
Sept. 28, 2006	Capt. S. Black (Navy Liaison to the Vice President) in the Vice Presidents' ceremonial office in the old executive office building in Washington DC.
May 2007	NDIA Joint Services Environmental Management Conference in Columbus, OH: Len Gollobin (Head of NDIA Energy Security Panel), Jim Woolsey (former head of CIA)
Nov. 7, 2007	SSC-Pacific: RADM Charles (Grunt) Smith (Vice CDR of SPAWAR)
May 2008	SSC-Pacific: James Colvard (retired SES, on special assignment to the Secretary of the Navy)
Apr. 2009	SSC-Pacific: ADM James Hogg (four star admiral, retired)
Apr. 14, 2009	SSC-Pacific: Brief given to congressional staffers
Apr. 27, 2009	SSC-Pacific: RADM Nevin P. Carr Jr. (Head of ONR)
May 14, 2009	AFCEA C4ISR at the San Diego Convention Center
June 26, 2009	SSC-Pacific: Dr. Richard L. Garwin (JASON Defense Advisory Group)
Aug. 2009	SSC-Pacific: B.J. Penn (ASN)
Sept. 24, 2009	SSC-Pacific: RADM Joe Rixey (Vice CDR of SPAWAR)
Oct. 27, 2009	SSC-Pacific: Mr. Zachary Lemnios (DDR&E)
Dec. 9, 2009	Chief of Naval Operations/Strategic Studies Group
May 13, 2010	MITRE Corp., VA, EMIS
June 29, 2010	Army Research Labs, Adelphi MD: RDECOM Power and Energy TFT LENR Workshop
Oct. 14, 2010	SSC-Pacific: Congressman Darrell Issa
Aug. 30, 2011	SSC-Pacific: Dr. Richard Carlin (ONR)
Others	RADM Kenneth Slaght (SPAWAR HQ); RADM Tim Flynn (when Captain of SSC-San Diego); Dr. John Fisher (DDR&E); Dr. Fred Saalfeld (senior civilian at ONR); VADM G. Peter Nanos (retired, Associate Director R&D at DTRA); Congresswoman Susan Davis; Senator Diane Feinstein

REFERENCES

1. S. Szpak and P.A. Mosier-Boss, ‘On the Behavior of the Cathodically Polarized Pd/D System: a Response to Vigier’s Comments,’ Phys. Letts. A, Vol. 221, pp. 141-143 (1996).

2. S. Szpak, P.A. Mosier-Boss, S.R. Scharber, and J.J. Smith, ‘Charging of the Pd/^{n}H System: Role of the Interphase,’ J. Electroanal. Chem., Vol. 337, pp. 147-163 (1992).

3. S. Szpak, P.A. Mosier-Boss, S.R. Scharber, and J.J. Smith, ‘Cyclic Voltammetry of Pd+D Codeposition,’ J. Electroanal. Chem., Vol. 380, pp. 1-6 (1995).

4. S. Szpak, P.A. Mosier-Boss, and J.J. Smith, ‘Deuterium Uptake During Pd-D Codeposition,’ J. Electroanal. Chem., Vol. 379, pp. 121-127 (1994).

5. S. Szpak, P.A. Mosier-Boss, and J.J. Smith, ‘On the Behavior of Pd Deposited in the Presence of Evolving Deuterium,’ J. Electroanal. Chem., Vol. 302, pp. 255-260 (1991).

6. M. Swartz, "Codeposition of Palladium and Deuterium", Fusion Technology, Vol. 32, pp. 126-130 (1997).

7. M. Swartz, "Quasi-One-Dimensional Model of Electrochemical Loading of Isotopic Fuel into a Metal", Fusion Technology, Vol. 22, pp. 296-300 (1992).

8. M. Swartz, "Isotopic Fuel Loading Coupled to Reactions At an Electrode", Fusion Technology, Vol. 26, pp. 74-77 (1994).

9. S. Szpak, P.A. Mosier-Boss, M.H. Miles, and M. Fleischmann, ‘Thermal Behavior of Polarized Pd/D Electrodes Prepared by Co-Deposition,’ Thermochim. Acta, Vol. 410, pp. 101-107 (2004).

10. D. Letts, ‘Codeposition Methods: A Search for Enabling Factors,’ J. Condensed Matter Nucl. Sci., Vol. 4, pp. 81-92 (2011).

11. P.A. Mosier-Boss and S. Szpak, ‘The Pd/^{n}H System: Transport Processes and Development of Thermal Instabilities,’ Il Nuovo Cimento, Vol. 112A, pp. 577-585 (1999).

12. S. Szpak, P.A. Mosier-Boss, and J.J. Smith, ‘On the Behavior of the Cathodically Polarized Pd/D System: Search for Emanating Radiation,’ Phys. Letts. A, Vol. 210, pp. 382-390 (1996).

13. M.R. Swartz, G. Verner, A. Weinberg, ‘Possible Non-Thermal Near-IR Emission Linked with Excess Power Gain in High Impedance and Codeposition Phusor-LANR Devices,’ in Fourteenth International Conference on Cold Fusion. 2008, Washington, DC.

14. S. Szpak, P.A. Mosier-Boss, R.D. Boss, and J.J. Smith, ‘On the Behavior of the Pd/D System: Evidence for Tritium Production,’ Fusion Technology, Vol. 33, pp. 38-51 (1998).

15. S. Szpak, P.A. Mosier-Boss, C. Young, and F.E. Gordon, 'Evidence of Nuclear Reactions in the Pd Lattice,' Naturwissenschaften, Vol. 92, pp. 394-397 (2005).

16. P.A. Mosier-Boss, S. Szpak, F.E. Gordon, and L.P.G. Forsley, 'Triple Tracks in CR-39 as the Result of Pd-D Co-deposition: Evidence of Energetic Neutrons,' Naturwissenschaften, Vol. 96, pp. 135-142 (2009).

17. M. Swartz, 'Consistency of the Biphasic Nature of Excess Enthalpy in Solid State Anomalous Phenomena with the Quasi-1-Dimensional Model of Isotope Loading into a Material,' Fusion Technology, Vol. 31, pp. 63-74 (1997).

18. M. Swartz, 'Phusons in Nuclear Reactions in Solids,' Fusion Technology, Vol. 31, pp. 228-236 (1997).

19. T. Skoskiewicz, A.W. Szanfranski, W. Bujnowski, and B. Baranowski, J. of Physics C, Vol. 7, pp. 2670-2676 (1974).

20. P. Tripodi, D. Di Gioacchino, and J. Darja Vinko, 'Magnetic and Transport Properties of PdH: Intriguing Superconductive Observations,' Brazilian J. Phys., Vol. 34, pp. 1177-1184 (2004).

21. F. Tanzella, SRI, personal communication.

22. P.A. Mosier-Boss, S. Szpak, F.E. Gordon, and L.P.G. Forsley, 'Use of CR-30 in Pd/D Co-deposition Experiments,' Eur. Phys. J. Appl. Phys., Vol. 40, pp. 293-303 (2007).

23. D. Nikezic and K.N. Yu, 'Formation and growth of tracks in nuclear track materials. Material Science and Engineering,' Mat. Sci. Eng. R. Vol. 46, pp. 51-123 (2004).

24. K. Oda, M. Ito, H. Miyake, M. Michijima, 'Track Formationin CR-39 Detector Exposed to D-T Neutrons,' Nucl. Instr. and Meth. in Phy. Res., Vol. B35, pp. 50-56 (1988).

25. G.W. Phillips, J.E. Spann, J.S. Bogard, T. VoDinh, D. Emfietzoglou, R.T. Devine, and M. Moscovitch, 'Neutron Spectrometry using CR-39 Track Etch Detectors,' Radiat. Protect. Dosim., Vol. 120, pp. 457-460 (2006).

26. A.G. Lipson, A.S. Roussetski, G.H. Miley, and E.I. Saunin, 'In-Situ Charged Particles And X-Ray Detection In Pd Thin Film-Cathodes During Electrolysis In Li_2SO_4/H_2O,' in *Condensed Matter Nuclear Science: Proceedings of the 9th International Conference on Cold Fusion* (Tsinghua Univ. Press, Beijing, 2002).

27. A.S. Roussetski, A.G. Lipson, B.F. Lyakhov, and E.I. Saunin, 'Correct Identification of Energetic Alpha and Proton Tracks in Experiments on CR-39 Charged Particle Detection During Hydrogen Desorption from Pd/PdO:Hx Heterostructure,' in *The 12th International Conference on Condensed Matter Nuclear Science* (Yokohama, Japan, 2005).

28. D. O'Sullivan, D. Zhou, W. Heinrich, S. Roesler, J. Donnelly, R. Keegan, E. Flood, and L. Tommasino, 'Cosmic Rays and Dosimetry at Aviation Altitudes,' Radiat. Mea., Vol. 31, pp. 579-584 (1999).

29. D. O'Sullivan, D. Zhou, E. Semones, W. Heinrich, and E. Flood, 'Dose Equivalent, Absorbed Dose and Charge Spectrum Investigations in Low Earth Orbit,' Adv. Space Res., Vol. 34, pp. 1420-1423 (2004).

30. D. Zhou, E. Semones, R. Gaza, S. Johnson, N. Zapp, and M. Weyland, 'Radiation Measured ISS-Expedition 12 with Different Dosimeters,' for Nucl. Instr. Meth., Vol. A580, pp. 1283-1289 (2007).

31. D. Zhou, E. Semones, R. Gaza, S. Johnson, N. Zapp, M. Weyland, R. Rutledge, and T. Lin, 'Radiation Measured with Different Dosimeters During STS-121 Space Mission,' Acta Astron., Vol. 64, pp. 437-447 (2009).

32. D. Zhou, E. Semones, R. Gaza, S. Johnson, N. Zapp, K. Lee, and T. George, 'Radiation Measured During ISS-Expedition 13 with Different Dosimeters,' Adv. Space Res., Vol. 43, pp. 1212-1219 (2009).

33. D. Zhou, E. Semones, D. O'Sullivan, N. Zapp, M. Weyland, G. Reitz, T. Berger, and E.R. Benton, 'Radiation Measured for MATROSHKA-1 Experiment with Passive Dosimeters,' Acta Astron., Vol. 66, pp. 301-308 (2010).

34. P.K. Iyengar and M. Srinivasan, *BARC Studies in Cold Fusion*, Bhabha Atomic Research Centre, Trombay, Bombay, India, 1989).

35. M. Swartz, 'Optimal Operating Point Manifolds in Active, Loaded Palladium Linked to Three Distinct Physical Regions,' in *The 14th International Conference on Condensed Matter Nuclear Science* (Washington D.C., USA, 2008).

36. E. Storms, 'Some Thoughts on the Nature of the Nuclear-Active Regions in Palladium,' in *the Sixth International Conference on Cold Fusion, Progress in New Hydrogen Energy* (Tokyo Institute of Technology, Tokyo, Japan, 1996).

37. K.L. Shanahan, 'Comments on a New Look at Low-Energy Nuclear Reaction Research,' J. Environ, Monit., Vol. 12, pp. 1756-1764 (2010).

38. J. Marwan, M. C. H. McKubre, F. L. Tanzella, P. L. Hagelstein, M. H. Miles, M. R. Swartz, Edmund Storms, Y. Iwamura, P. A. Mosier-Boss and L. P. G. Forsley, 'A New Look at Low-Energy Nuclear Reaction Research,' J. Environ, Monit., Vol. 12, pp. 1765-1770 (2010).

39. L. Kowalski, 'Comments on Codeposition Electrolysis Results,' J. Condensed Matter Nucl. Sci., Vol. 3, pp. 1-3 (2010).

40. U. Mastromatteo and R. Aina, ‘Investigation of Anomalous Densities of High Energy Alpha Particles Tracks in CR-39 Detectors During Electrolysis of Heavy Water on Palladium Cathodes,’ in the *15th International Conference on Condensed Matter Nuclear Science* (Rome, Italy, 2010).

41. P.A. Mosier-Boss, S. Szpak, F.E. Gordon, and L.P.G. Forsley, ‘Comments on Co-deposition Electrolysis Results: A Response to Kowalaski,’ J. Condensed Matter Nucl. Sci., Vol. 3, pp. 4-8 (2010).

42. P.A. Mosier-Boss, S. Szpak, F.E. Gordon, and L.P.G. Forsley, ‘Characterization of Tracks in CR-39 Detectors Obtained as a Result of Pd/D Co-deposition,’ Eur. Phys. J. Appl. Phys., Vol. 46, pp. 30901 p. 1-12 (2009).

43. E. Składnik-Sadowska, J. Baranowski, M. Sadowski, ’Low-Energy Ion Measurements by Means of CR-39 Nuclear Track Detectors,’ Radiat. Meas., Vol. 34, pp. 337-339 (2001).

44. J.A. Frenje, C.K. Li, F.H. Séguin, D.G. Hicks, S. Kurebayashi, R.D. Petrasso, S. Roberts, V.Y. Glebov, D.D. Meyerhofer, T.C. Sangster, J.M. Soures, C. Stoeckl, G.J. Schmid, R.A. Lerche, ‘Absolute measurements of neutron yields from DD and DT implosions at the OMEGA laser facility using CR-39 track detectors,’ Rev. Sci. Instrum., Vol. 73, pp. 2597-2605 (2002).

45. P.A. Mosier-Boss, J.Y. Dea, M.S. Morey, J.R. Tinsley, J.P Hurley, L.P.G. Forsley, and F.E. Gordon, ‘Comparison of Pd/D Co-deposition and DT Neutron Generated Triple Tracks Observed in CR-39 Detectors,’ Eur. Phys. J. Appl. Phys., Vol. 51, 20901 pp. 1-11 (2010).

46. B. Antolkovia and Z. Dolenec, ‘The Neutron-Induced $^{12}C(n, n')3\alpha$ Reaction at 14.4 MeV in a Kinematically Complete Experiment,’ Nucl. Phys. A Vol. 237, pp. 235-252 (1975).

47. A. Aframian, ‘Disintegration of Carbon-12 with 7.1-20.1 MeV Neutrons in Dielectrics,’ J. Phys. G: Nucl. Phys.Vol. 9, pp. 985-994 (1983)

48. M. Balcázar-García and S.A. Durrani, ‘High-Energy Neutron Spectrometry with Plastic SSNTDs,’ Nucl. Instrum. Meth., Vol. 173, pp. 131-135 (1980).

49. T. Nakamura, T. Nunomiya, S. Abe. K. Terunuma, and H. Suzuki, ‘Sequential Measurements of Cosmic-Ray Neutron Spectrum and Dose Rate at Sea Levels in Sendai, Japan,’ J. Nucl. Sci. Technol. Vol. 42, pp. 843-853 (2005).

50. P.J. Dimbylow, ‘Neutron Cross-Sections and Kerma Values for Carbon, Nitrogen and Oxygen from 20 to 50 MeV,’ Phys. Med. Biol., Vol. 25, p, 637-650 (1980).

51. A.G. Lipson, B.F. Lyakhov, A.S. Roussetski, T. Akimoto, T. Mizuno, N. Asami, R. Shimada, S. Mitashita, and A. Takahashi, ‘Evidence for Low-Intensity D-D Reaction as a Result of Exothermic Deuterium Desorption from Au/Pd/PdO:D Heterostructure,’ Fus. Technol., Vol. 38, pp. 238-252 (2000).

52. R. Taniguchi, T. Yamamoto, S. Irie, ‘Detection of Charged Particles Emitted by Electrolytically Induced Cold Nuclear Fusion,’ Jpn J. Appl. Phys., Vol. 28, pp. L2021-L2023 (1989).

53. A.S. Roussetski, ‘Application of CR-39 Plastic Track Detector for Detection of DD and DT-Reaction Products in Cold Fusion Experiments’ in *8th International Conference on Cold Fusion* (Italian Physical Society, Bologna, Italy, 2000).

54. A. Takahashi, ‘Some Considerations of Multibody Fusion in Metal Deuterides,’ Fus. Technol. **26**, 451 (1994).

55. J.D. Lawsen, ‘Some Criteria for a Power Producing Thermonuclear Reactor,’Proc. Phys. Soc. Lond. B, Vol. 70, pp. 6-10 (1957).

56. D.J. Cravens and D.G. Letts, ‘Practical Techniques in CF Research – Triggering Methods,’ in *10th International Conference in Cold Fusion* (Cambridge, MA, USA 2003).

57. T.W. Raudorf and R.H. Pehl, ‘Effect of Charge Carrier Trapping on Germanium Coaxial Detector Line Shapes,’ Nucl. Instru. and Meth., Vol. A255, pp. 538-551 (1987).

58. P. Leleux, F. Albernhe, V. Borrel, B. Cordier, R. Coszach, S. Crespin, J.M. Denis, P. Duhanel, P. Frabel, W. Galster, J.-S. Graulich, P. Jean, B. Kandel, J.P. Meulders, G. Tauzin, J. Vanhorenbeeck, G. Vedrenne, and P. von Ballmoos, ‘Neutron-Induced Nuclear Reactions and Degradation in Germanium Detectors,’ A&A, Vol. 411, pp. L85-L90 (2003).

59. V. Borrel, B, Kandel, F. Albernhe, P. Frabel, B. Cordier, G. Tauzin, S. Crespin, R. Coszach, J.M. Denis, and P. Leleux, ‘Fast Neutron-Induced Damage in INTEGRAL n-Type HPGe Detectors,’ Nucl. Instru. and Meth., Vol. A430, pp. 348-362 (1999).

60. N. Jovančević and M. Krmar, ‘Neutrons in the Low-Background Ge-Detector Vicinity Estimated from Different Activation Reactions,’ Appl. Rad. And Isotopes, Vol. 69, pp. 629-635 (2011).

61. G. Fehrehbacher, R. Meckbach, and H.G. Paretzke, ‘Fast Neutron Detection with Germanium Detectors: Computation of Response Functions for the 692 keV Inelastic Scattering Peak,’ Nucl. Instru. and Meth., Vol. A372, pp. 239-245 (1996).

62. J.K. Pálfalvi, Y. Akatov, J. Szabó, L. Sajó-Bohus, and I. Eördögh, ‘Evaluation of Solid State Nuclear Track Detector Stacks Exposed on the International Space Station,’ Rad. Prot. Dos., Vol. 110, pp. 393-397 (2004).

63. S.M. Bennington, R.S. Sokhi, P.R. Stonadge, D.K. Ross, M.J. Benham, T.D. Beynon, P. Whithey, I.R. Harris, J.P.G. Farr, 'A Search for the Emission of X-rays from Electrochemically Charged Palladium-Deuterium,' Electrochimica Acta, Vol. 34, pp. 1323-1326 (1989).

64. M.R. Deakin, J.D. Fox, K.W. Kemper, E.G. Myers, W.N. Shelton, J.G. Skofronick, 'Search for Cold Fusion using X-ray Detection,' Phys. Rev. C, Vol. 40, pp. R1851-R1853 (1989).

65. http://www.bubbletech.ca/radiation_detectors_files/Bubble%20Detectors.html

66. I. Dardik, T. Zilov, H. Branover, A. El-Boher, E. Greenspan, B. Khachaturov, V. Krakov, S Lesin, and M. Tsirlin, 'Excess Heat in Electrolysis Experiments at Energetics Technologies,' in *11th International Conference in Cold Fusion* (Marseilles, France 2004).

67. S. Szpak, P.A. Mosier-Boss, and M.H. Miles, 'Calorimetry of the Pd+D Codeposition,' Fusion Technology, Vol. 36, pp. 234-241 (1999).

68. http://www.web.pdx.edu/~jiaoj/phy451/Lect7.pdf

69. J. O'M. Bockris, 'Early Contributions from Workers at Texas A&M University to (So-Called) Low Energy Nuclear Reactions,' J. of New Energy, Vol. 4, p. 40 (1999).

Appendix I: Miscellaneous

1. Statement given at the press conference at the American Chemical Society on March 2009

2. Complete bibliography of SSC-Pacific/JWK LENR publications

ACS Press Conference Statement

Pamela A. Mosier-Boss

March 23, 2009

Initial criticism of the purported Pd/D low energy nuclear reactions centered upon the phenomena's irreproducibility. Many years later this was understood to be due to the long incubation times required to fully load the Pd with deuterium. However, early on, Dr. Stanislaw Szpak, an electrochemist at the Naval laboratory in San Diego, developed an alternative method of initiating low energy nuclear reactions using Pd/D co-deposition. In this process palladium metal is plated out in the presence of deuterium gas. The advantages of this approach are that the palladium metal loads instantly with deuterium, the experiments can be done faster, there is a great deal of experimental flexibility, and the experiments are reproducible. Other groups from SRI, UCSD, Texas A & M, the Navy Laboratory in China Lake, and Berkeley have obtained positive results using the co-deposition process.

Early experiments using thermocouples showed that the co-deposition electrode was always hotter than the solution. This indicated that the electrode was the heat source and not Joule heating. Calorimetric measurements, done by Dr. Melvin Miles of China Lake, showed that the rates of excess enthalpy generation using electrodes prepared by the co-deposition technique were comparable to that obtained when Pd bulk electrodes were used. Infrared imaging of electrodes prepared by co-deposition, in collaboration with Prof. Simnad of UCSD and Dr. Todd Evans of General Atomics, showed the presence of hot spots were indicative of mini-explosions. This was confirmed in an experiment suggested by Dr. Lowell Wood, of LLNL, by co-depositing Pd and D on a transducer that recorded the mini-explosion pressure and heat transients as they occurred.

Ultimately, we concluded that heat alone was not going to convince others that nuclear reactions were occurring inside the Pd lattice. Our focus changed to look for evidence of nuclear ash. Using conventional nuclear diagnostics, we showed that the emission of X-rays, γ-rays, and tritium occurred as a result of co-deposition. These emissions occurred sporadically and in bursts. To enhance these effects, experiments were conducted in the presence of either an external electric or magnetic field. Examination of the Pd deposits at the end of the experiments showed significant morphological changes that were consistent with localized melting of the metal. Further analysis of these molten-like features showed the presence of new elements, such as Al, Mg, Ca, Si, and Zn. More recent experiments using a solid state nuclear track etch detector during co-deposition has shown the emission of both charged particles and neutrons. The observed size distribution of the particles and neutrons obtained as a result of co-deposition is consistent with those observed for DD and DT fusion. Taking all the data together, we have compelling evidence that nuclear reactions are stimulated by electro-chemical processes. To date, these observations have been published in 20 peer-reviewed journal papers and one peer-reviewed symposium book. Two additional papers have been accepted for publication later this year.

As to the future, there are a number of potential uses for the heat and nuclear emissions generated as a result of the low energy nuclear reactions occurring inside a metal lattice. Heat can be directly converted into power without the emission of greenhouse gases. The energetic particles can be directly converted into electricity as is done in radioisotope thermoelectric generators. Uses of neutrons include the remediation of radioactive waste and the production of radioisotopes used in medical, industrial, and environmental applications. However, in order to achieve its full potential, additional research is needed to determine the mechanism by which low energy nuclear reactions occur within a metal lattice. Only then will it be possible to optimize and control these reactions for a given application.

Bibliography

I. Publications

1. S. Szpak, P.A. Mosier-Boss, and J.J. Smith, “On the Behavior of Pd Deposited in the Presence of Evolving Deuterium,” *J. Electroanal. Chem*., **302** (1991) 255.

2. S. Szpak, C.J. Gabriel, and R. J. Nowak, “Electrochemical Charging of Pd Rods,” *J. Electroanal.Chem*., **309** (1991) 273-292

3. S. Szpak, P.A. Mosier-Boss, S.R. Scharber, and J.J. Smith, “Charging of the Pd/^{n}H System: Role of the Interphase,” *J. Electroanal. Chem*., **337** (1992) 147 (1992).

4. S. Szpak, P.A. Mosier-Boss, C.J. Gabriel, and J.J. Smith “Absorption of Deuterium in Palladium Rods: Model vs. Experiment,” *J. Electroanal. Chem*., **365** (1994) 275.

5. S. Szpak, P.A. Mosier-Boss, R.D. Boss and J.J. Smith “Comments on the Analysis of Tritium Content in Electrochemical Cells,” *J. Electroanal. Chem*., **373** (1994) 1.

6. S. Szpak, P.A. Mosier-Boss, and J.J. Smith, “Deuterium Uptake During Pd-D Codeposition,” *J. Electroanal. Chem.*, **379** (1994) 121.

7. S. Szpak, P.A. Mosier-Boss, S.R. Scharber, and J.J. Smith, “Cyclic Voltammetry of Pd/D Co-deposition,” *J. Electroanal. Chem*., **380** (1995) 1.

8. S. Szpak, P.A. Mosier-Boss, and J.J. Smith, “On the Behavior of the Cathodically Polarized Pd/D System: Search for Emanating Radiation,” *Physics Letters A*, **210** (1995) 382.

9. S. Szpak and P.A. Mosier-Boss, “Nuclear and Thermal Events Associated with Pd+D Codeposition,” *J. New Energy* **1** (1996) 54.

10. S. Szpak and P.A. Mosier-Boss, “On the Behavior of the Cathodocally Polarized Pd/D System: A Response to Vigier's Comments,” *Physics Letters A,* **211** (1996) 141.

11. S. Szpak, P.A. Mosier-Boss, R.D. Boss, and J.J. Smith, “On the Behavior of the Pd/D System: Evidence for Tritium Production,” *Fusion Technology*, **33** (1998) 38.

12. S. Szpak and P.A. Mosier-Boss, “On the Release of ^{n}H from Cathodically Polarized Palladium Electrodes,” *Fusion Technology*, **34** (1998) 273.

13. S. Szpak and P.A. Mosier-Boss, “The Pd/^{n}H System: Transport Processes and Development of Thermal Instabilities,” *Il Nuovo Cimento*, **112** (1999) 577.

14. S. Szpak, P.A. Mosier-Boss, and M. H. Miles, “Calorimetry of the Pd + D Codeposition,” *Fusion Technology*, **36** (1999) 234.

15. S. Szpak, P.A. Mosier-Boss, M. H. Miles, and M. Fleischmann, "Thermal Behavior of Polarized Pd/D Electrodes Prepared by Co-Deposition," *Thermochimica Acta*, **410** (2004) 101.

16. S. Szpak, P.A. Mosier-Boss, C. Young, and F.E. Gordon, "The Effect of an External Electric Field on Surface Morphology of Co-Deposited Pd/D Films," *J. Electroanal. Chem.*, **580** (2005) 284.

17. S. Szpak, P.A. Mosier-Boss, C. Young, and F.E. Gordon, "Evidence of Nuclear Reactions in the Pd Lattice," *Naturwissenschaften*, **92** (2005) 394.

18. S. Szpak, P.A. Mosier-Boss, and F.E. Gordon, "Further Evidence of Nuclear Reactions in the Pd/D Lattice: Emission of Charged Particles," *Naturwissenschaften*, **94** (2007) 511.

19. S. Szpak, P.A. Mosier-Boss, F.E. Gordon, and L.P.G. Forsley, "Use of CR-39 in Pd/D Co-Deposition Experiments," *European Physics Journal-Applied Physics*, **40** (2007) 293.

20. S. Szpak, P.A. Mosier-Boss, F.E. Gordon, and L.P.G. Forsley, "Reply to Comment on 'the Use of CR-39 in Pd/D Co-deposition Experiments': a Response to Kowalski," *European Physics Journal-Applied Physics*, **44** (2008) 291.

21. S. Szpak, P.A. Mosier-Boss, F.E. Gordon, and L.P.G. Forsley, "Detection of Energetic Particles and Neutrons Emitted During Pd.D Co-Deposition," in *Low-Energy Nuclear Reactions Sourcebook*, J. Marwan and S. Krivit (Ed), Oxford Univ. Press (2008).

22. S. Szpak, P.A. Mosier-Boss, F.E. Gordon, and L.P.G. Forsley, "Triple Tracks in CR-39 as the Result of Pd/D Co-deposition: Evidence of Energetic Neutrons," *Naturwissenschaften*, **96** (2009) 135.

23. S. Szpak, P.A. Mosier-Boss, F.E. Gordon, and L.P.G. Forsley, "Characterization of Tracks in CR-39 Detectors Obtained as a Result of Pd/D Co-Deposition," *European Physics Journal-Applied Physics*, **46** (2009) 30901.

24. S. Szpak, P.A. Mosier-Boss, F.E. Gordon, and L.P.G. Forsley, "Characterization of Neutrons Emitted During Pd/D Co-Deposition," *J. of Scientific Exploration*, **23** (2009) 473.

25. P.A. Mosier-Boss, L.P.G. Forsley, and F.E. Gordon, "Comments on Co-deposition Electrolysis Results: A Response to Kowalski," *J. Condensed Matter Nucl. Sci.*, **3**, (2010) 4.

26. P.A. Mosier-Boss, J.Y. Dea, L.P.G. Forsley, M.S. Morey, J.R. Tinsley, J.P. Hurley, and F.E. Gordon, "Comparison of Pd/D Co-Deposition and DT Neutron Generated Triple Tracks Observed in CR-39 Detectors," *European Physics Journal-Applied Physics*, **51**, (2010) 20901.

27. P.A. Mosier-Boss, F.E. Gordon, and L.P.G. Forsley, "Characterization of Energetic Particles Emitted During Pd/D Co-Deposition for Use in a Radioisotope Thermoelectric Generator (RTG)," in *Low-Energy Nuclear Reactions Sourcebook Volume 2*, J. Marwan and S. Krivit (Ed), Oxford Univ. Press (2010).

28. J. Marwan, M.C.H. McKubre, F.L. Tanzella, P.L. Hagelstein, M.H. Miles, M.R. Swartz, Edmund Storms, Y. Iwamura, P.A. Mosier-Boss, and L.P.G. Forsley "A New Look at Low-Energy Nuclear Reaction (LENR) Research: a Response to Shanahan," *J. Environ. Monitor.*, **12** (2010) 1765.

29. P.A. Mosier-Boss, J.Y. Dea, F.E. Gordon, L.P.G. Forsley, and M.H. Miles, "Review of Twenty Years of LENR Research Using Pd/D Co-deposition," *J. Condensed Matter Nucl. Sci.*, **4** (2011) 173.

30. P.A. Mosier-Boss, F. Tanzella and M. Miles, "ACS New Energy Technology Symposium," *Infinite Energy*, **97** (2011) 10.

31. P.A. Mosier-Boss, L.P.G. Forsley, P. Carbonnelle, M.S. Morey, J.R. Tinsley, J.P. Hurley, and F.E. Gordon, "Comparison of SEM and Optical Analyses of DT Neutron Tracks in CR-39 Detectors," *Radiation Measurements*, **47** (2012) 57.

32. P.A. Mosier-Boss, F.E. Gordon, and L.P.G. Forsley, "Characterization of Neutrons Emitted during Pd/D Co-deposition," *J. Condensed Matter Nucl. Sci.,* **6** (2012) 13.

33. P.A. Mosier-Boss, "A Review on Nuclear Products Generated During Low-Energy Nuclear Reactions (LENR)," *J. Condensed Matter Nucl. Sci.*, **6** (2012) 135.

II. Presentations/Posters/Conference Proceedings

1. S. Szpak, P.A. Mosier-Boss, and J.J. Smith, "Reliable Procedure for the Initiation of the Fleischmann-Pons Effect" in *The Science Of Cold Fusion*, T. Bressani, E. Del Giudice, and G. Preparata, eds., Proceedings of the II Annual Conference on Cold Fusion, Como, Italy, June 1991.

2. S. Szpak, P.A. Mosier-Boss, and J.J. Smith, "Comments on Methodology of Excess Tritium Determination," in Proceedings ICCF-3, H. Ikegami, ed., Third International Conference on Cold Fusion, Nagoya, Japan, Oct. 1992.

3. S. Szpak and P.A. Mosier-Boss, "Thermal and Nuclear Events in a Polarized Pd + D System: an Overview,"Amer. Chem. Soc. Western Regional Meeting, Ontario, CA, Oct. 1999.

4. P.A. Mosier-Boss, J. Dea and S. Szpak, "Thermal and Pressure Gradients in Polarized Pd/D System", Amer. Phys. Soc., Indianapolis, IN, March 2002.

5. M.H. Miles, S. Szpak, P.A. Mosier-Boss, and M. Fleischmann, "Thermal Behavior of Polarized Pd/D Electrodes Prepared by Co-deposition," ICCF-9, Beijing, China, May 2002.

6. S. Szpak and P.A. Mosier-Boss, "The Dynamics of the $Pd/D-D_2O-Li^+$ System as a Precursor to the Fleischmann-Pons Effect," 2003 ANS Annual Meeting, San Diego, CA, June 2003.

7. S. Szpak, P.A. Mosier-Boss, J. Dea, and F. Gordon, “Polarized D^+/Pd-D_2O System: Hot-Spots and Mini-Explosions,” ICCF-10, Cambridge, MA, Aug. 2003.

8. S. Szpak, P.A. Mosier-Boss, and F. Gordon, “Precursors and the Fusion Reactions in Polarized Pd/D-D_2O System: Effect of an External Electric Field,” ICCF-11, Marseille, France, Nov. 2004.

9. S. Szpak, P.A. Mosier-Boss, and F. Gordon, “Experimental Evidence for LENR in a Polarized Pd/D Lattice,” Amer. Phys. Soc., Los Angeles, CA, March 2005.

10. S. Szpak, P.A. Mosier-Boss, and F. Gordon, “Experimental Evidence for LENR in a Polarized Pd/D Lattice,” NDIA Naval S&T Partnership Conference, Washington DC, Aug. 2006.

11. P.A. Mosier-Boss, S. Szpak, and F. Gordon, “Production of High Energy Particles Using the Pd/D Co-Deposition Process,” Amer. Phys. Soc., Denver, CO, March 2007.

12. L.P.G. Forsley, G.W. Phillips, S. Szpak, P.A. Mosier-Boss, J.W. Khim, and F.E. Gordon, “Time Resolved, High Resolution, γ-Ray and Integrated Charge and Knock-on Particle Measurements of Pd:D Co-deposition Cells,” Amer. Phys. Soc., Denver, CO, March 2007.

13. L.P.G. Forsley, “Observations of Oppenheimer-Born Approximation Negation and Oppenheimer-Phillips Reactions in Condensed Matter Nuclear Science”, Amer. Phys. Soc., Denver, CO, March, (2007)

14. S. Szpak, P.A. Mosier-Boss, F.E. Gordon, L.P.G. Forsley, and G.W. Phillips, “Pd/D Co-Deposition: Excess Power Generation and Its Origin,” Amer. Chem. Soc., Chicago, IL, March 2007.

15. S. Szpak, F.E. Gordon, P.A. Mosier-Boss, L.P.G. Forsley, and G.W. Phillips, “Low Energy Nuclear Reactions: Historically Known as Cold Fusion,” NDIA JSEM, Columbus, OH, May 2007.

16. W. Williams, L.P.G. Forsley, *et al,* “Analysis of Nuclear Particles from Independent Replications Using the SPAWAR Co-Dep TGP Protocol and CR-39 Track Detectors”, Proc. of the 8th Int. Workshop on Anomalies in Hydrogen and Deuterium-Loaded Metals, Catania, Sicily, October 2007.

17. L.P.G. Forsley and P.A. Mosier-Boss, “Comparison of SPAWAR Co-deposition Experimental Data and Competing Condensed Matter Nuclear Science Theories,” Amer. Phys. Soc., New Orleans, LA, March 2008.

18. L.P.G. Forsley and P.A. Mosier-Boss, “Multiple Etching of CR-39 Nuclear Track Detectors used in SPAWAR Co-Dep Experiment,”Amer. Phys. Soc., New Orleans, LA, March 2008.

19. S. Szpak, P.A. Mosier-Boss, F. Gordon, J. Dea, M. Miles, J.W. Khim, and L. Forsley, “LENR Research Using Co-Deposition,” ICCF-14, Washington DC, August 2008.

20. L.P.G.Forsley and P.A. Mosier-Boss, “Quantitative Spatial Analysis of Pd/D Co-Deposited Induced Nuclear Particle Tracks”, ISCMNS-14*,* Washington, DC, August 2008.

21. S. Szpak, P.A. Mosier-Boss, F. Gordon, J. Dea, M. Miles, J.W. Khim, and L. Forsley, “SPAWAR Systems Center-Pacific Pd:D Co-Deposition Research: Overview of Refereed LENR Publications”, ISCMNS-14 Vol **2**, Washington, DC, pp 772-777 (2008).

22. S. Szpak, P.A. Mosier-Boss, F. Gordon, J. Dea, M. Miles, J.W. Khim, and L. Forsley, “LENR Research Using Co-Deposition”, ISCMNS-14 Vol **2**, Washington, DC, pp 766-771 (2008).

23. M. Swartz and L.P.G. Forsley, “Analysis and Confirmation of the “Superwave-as-Transitory-OOP-Peak” Hypothesis”, ISCMNS-14 Vol **2**, Washington, DC, pp 653 - 662 (2008)

24. P.A. Mosier-Boss, S. Szpak, F.E. Gordon, and L.P.G. Forsley, “CR-39 Studies of Pd/D Co-Deposition,” Amer. Chem. Soc., Philadelphia, PA, August 2008.

25. S. Szpak, P.A. Mosier-Boss, F.E. Gordon, and L.P.G. Forsley,“Twenty Year History of LENR Research Using Pd/D Co-Deposition,” Amer. Chem. Soc., Salt Lake City, UT, March 2009.

26. P.A. Mosier-Boss, S. Szpak, F.E. Gordon, and L.P.G. Forsley, “Characterization of Neutrons Emitted During Pd/D Co-Deposition,” Amer. Chem. Soc., Salt Lake City, UT, March 2009.

27. L.P.G. Forsley, P.A. Mosier-Boss, and F.E. Gordon, “Nano-nuclear Reactions in Condensed Matter,” Amer. Chem. Soc., Salt Lake City, UT, March 2009.

28. L.P.G. Forsley, “Cold Fusion Seminar”, *Belgian Nuclear Research Center, SCK.CEN, Fusion Support Unit*, invited talk, Boeretang, Belgium, May 2009.

29. L.P.G. Forsley, “Lattice-assisted Nuclear Reaction: overview”, *The First Colloquium on Nano-Nuclear Science,* Université catholique de Louvain, invited talk, Louvain-la-Neuve, Belgium, May 2009.

30. L.P.G. Forsley, “An Experimental Protocol for Exploring nano-nuclear science”, *The First Colloquium on Nano-Nuclear Science,* Université catholique de Louvain, Louvain-la-Neuve, Belgium, May 2009.

31. L.P.G. Forsley, “Two Channels: Evidence of aneutronic and conventional fusion”, *The First Colloquium on Nano-Nuclear Science,* Université catholique de Louvain, Louvain-la-Neuve, Belgium, May 2009.

32. L.P.G. Forsley, “The Wider Phenomena: electron screening, nuclear cross-sections and superconductivity”, *The First Colloquium on Nano-Nuclear Science,* Université catholique de Louvain, Louvain-la-Neuve, Belgium, May 2009.

33. F.E. Gordon, P.A. Mosier-Boss, and L.P.G. Forsley, “SPAWAR Group Abstract: Twenty-Year History of Lattice-Enabled Nuclear Reactions Using Pd/D Co-deposition”, *University of Missouri LENR Symposium*, Columbia, MO, May 2009.

34. L.P.G. Forsley, “SPAWAR’s Low Energy Nuclear Reaction CRADA”, *Changing Landscapes in Energy and High Technology, FLC Far West and Mid-Continent Joint Regional Meeting*, invited talk, San Francisco, CA, August (2009)

35. P.A. Mosier-Boss, F.E. Gordon, and L.P.G. Forsley, “Characterization of Nuclear Emissions Resulting from Pd/D Co-deposition,” Amer. Chem. Soc., San Francisco, CA, March 2010.

36. P.A. Mosier-Boss and L.P.G. Forsley, “LENR Evidence”, *2010 Energetic Materials Intelligence Seminar*, MITRE Corp., VA, May 2010.

37. P.A. Mosier-Boss, L.P.G. Forsley, M.S. Morey, J. R. Tinsley, J.P. Hurley, P. Carbonnelle, and F.E. Gordon, “Comparison of DT- Generated and Pd/D Co-deposition Triple Tracks in CR-39 Detectors,” Amer. Chem. Soc., Anaheim, CA, March 2011.

38. L.P.G. Forsley, P.A. Mosier-Boss, F. Tanzella, A. Lipson, D. Zhou, A. Roussetski, and M. McKubre, “Comparison of Three Methods of Analyzing Nuclear Tracks Observed in CR-39 Detectors used in Pd/D Co-deposition Experiments,” Amer. Chem. Soc., Anaheim, CA, March 2011.

39. P.A. Mosier-Boss, L.P.G. Forsley, M.S. Morey, J. R. Tinsley, J.P. Hurley, P. Carbonnelle, and F.E. Gordon, “Comparison of SEM and Optical Analysis of DT Neutron Tracks in CR-39 Detectors,” SPIE “Hard X-Ray, Gamma-Ray, and Neutron Detector Physics XIII," San Diego, CA, August 2011.

40. P.A. Mosier-Boss, “The Greening of America: a New Nuclear Future,” 243rd American Chemical Society National Meeting, San Diego, CA, Mar. 2012.

41. L.P.G. Forsley, S. Newsome, P.A. Mosier-Boss, R. Bost, and A. Kirk, “Fukushima Revisited and the Nano-Nuclear Alternative,” 243rd American Chemical Society National Meeting, San Diego, CA, Mar. 2012.

III. Technical Reports

1. P.A. Mosier-Boss and S. Szpak, “Anomalous Behavior of the Pd/D System,” Technical Report 1696, September 1995, Naval Command Control and Ocean Surveillance Center RDT & E Division, San Diego, CA 92152-5000.

2. P.A. Mosier-Boss and S. Szpak, “Thermal and Nuclear Aspects of the Pd/D_2O Systems. Vol. 1: A Decade of Research of Navy Laboratories,” Technical Report 1862 vol. 1, Feb. 2002, Space and Naval Warfare Systems Center San Diego, CA 92152-5001.

3. P.A. Mosier-Boss and S. Szpak, “Thermal and Nuclear Aspects of the Pd/D_2O Systems. Vol. 2: Simulation of the Electrochemical Cell (ICARUS) Calorimetry,” Technical Report 1862 vol. 2, Feb. 2002, Space and Naval Warfare Systems Center San Diego, CA 92152-5001.

IV. Patents

1. P.A. Boss and S. Szpak, “Electrochemical Cell Having a Beryllium Compound Coated Electrode", Navy Case 76707. U.S. Patent No. 5,928,483 issued 7/27/99.